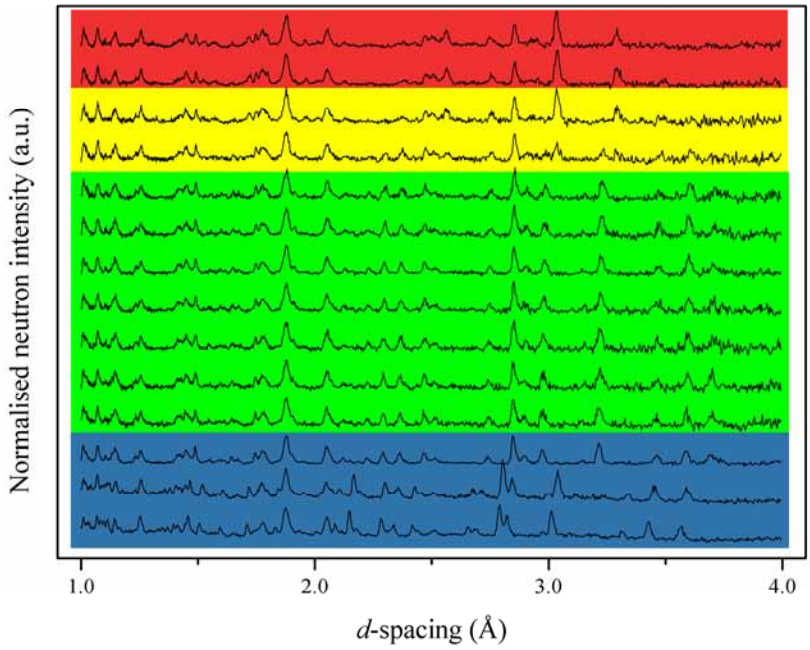

Figure 3.25 Neutron powder diffraction patterns obtained during the decompression of ε-RDX to ambient pressure at 150 K, and the subsequent warming of the sample at ambient pressure. The patterns highlighted in blue were obtained during the decompression of ε-RDX at 150 K (at 3.34, 2.47 and 0.00 GPa, respectively); the patterns shown in green represented the warming of ε-RDX at ambient pressure – data were obtained in 10 K intervals to a maximum of 220 K. Warming to 230 K, however, resulted in the formation of a mixed ε/α-phase and then a pure sample of the α-form. These patterns are shown in yellow. Finally, the sample was warmed to 240 K to ensure complete conversion to α-RDX before a pattern was collected at 220 K to facilitate comparison with the ε-form – these are shown in red. It should be noted that the patterns have been vertically scaled for clarity.

	ε-RDX	α-RDX
Space Group	$Pca2_1$	*Pbca*
a (Å)	7.519(4)	13.166(4)
b (Å)	11.643(5)	11.539(4)
c (Å)	9.177(4)	10.667(3)
V (Å^3)	803.4(4)	1620.6(5)
Z	4	8
D_c (Mg m^{-3})	1.836	1.821

Table 3.6 Comparison of the crystallographic data obtained for ε- and α-RDX at ambient pressure and 220 K.

The observation that ε-RDX can be recovered to ambient pressure and that it has been shown to be denser than the α-form under the exact same conditions has significant implications. This 'proof-of-concept' experiment has shown that the recovery of high-pressure

polymorphs is a viable route to novel materials, potentially with improved performance, and these studies are currently being extended to other energetic materials with a view to improving their performance.

3.5.3 δ-RDX: the very-high-pressure form of RDX

After the successful determination of the structures of the γ-, β-, and ε-forms of RDX [37, 87, 88], it was thought prudent to investigate the polymorphism of RDX under very high pressures (up to ~ 20 GPa). High-pressure X-ray powder diffraction experiments were carried out at the Extreme Conditions (I15) and High Resolution Powder Diffraction (I11) Beamlines at Diamond Light Source. In each case polycrystalline RDX was loaded into a Merrill-Bassett diamond-anvil cell (DAC) and pre-compressed to the maximum pressure studied. The studies undertaken at I15 used methanol:ethanol (4:1) as the pressure-transmitting medium, despite pressure-induced freezing of the pressure medium being reported to occur ~9.8 GPa at ambient temperature.[89] No medium was used in the I11 study in order to investigate any possible structural changes induced by compression to ~ 20 GPa under non-hydrostatic conditions.

Multiplots of the patterns collected at the two beamlines can be found in Figure 3.26. On initial inspection it does not appear that there are any significant changes (other than the α → γ phase transition) in the diffraction patterns over this pressure range, although peak broadening under these non-hydrostatic conditions results in much lower resolution. It is interesting to note that both the α- and γ-polymorphs are present in the diffraction pattern collected at 5.8 GPa in the I15 experiment. This implies that there is a signicant pressure gradient within the sample in this experiment (of ~ 2.0 GPa) as α-RDX has never been observed to exist beyond 3.9 GPa.[29-31, 37]

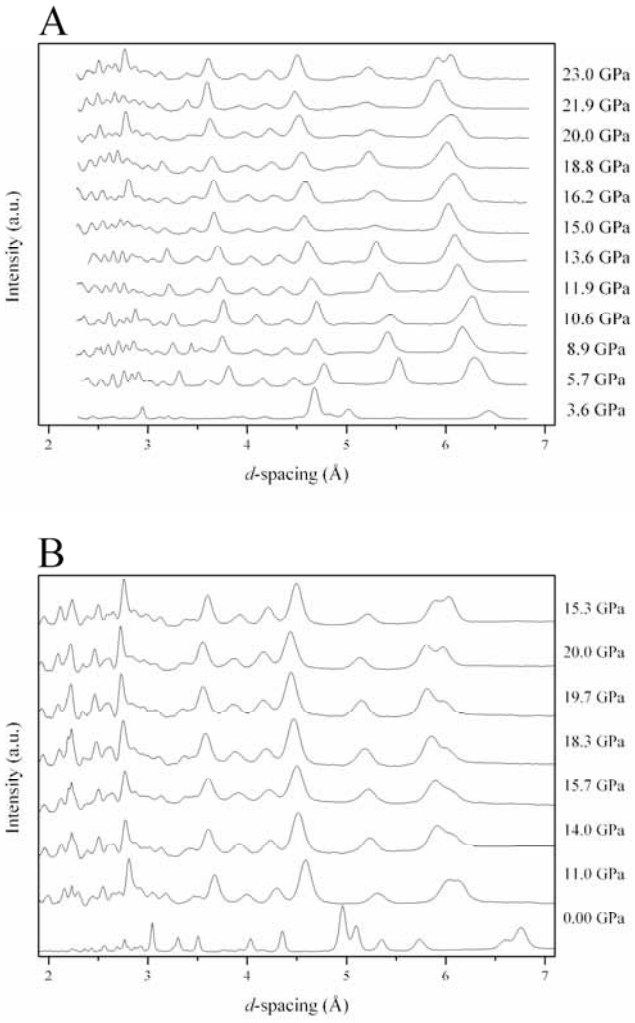

Figure 3.26 Series of diffraction patterns (scaled vertically) collected during the decompression of RDX: (a) from 23.0 GPa using MeOH:EtOH (4:1) on the Extreme Conditions Beamline (I15); (b) from 20.0 GPa on the High Resolution Powder Diffraction Beamline (I11), where no pressure medium was employed. In both experiments the diffraction pattern collected at the lowest pressure was successfully refined using the α-RDX structural model; all other patterns were indexed to the γ-form.

It was possible to perform Le Bail refinements on all of the patterns collected using the unit cell indexing of either the α-form (for patterns collected below 3.9 GPa) or the γ-form (all other patterns) confirming that no phase transitions to the reported δ-form occurred within the pressure range of this work. Unfortunately the low resolution of the powder patterns meant that Rietveld refinements were not sufficiently stable; it was therefore not possible to refine atomic positions, but inspection of the data showed that all peaks were modelled satisfactorily and that there were no extraneous peaks that may be indicative of a significant change in molecular geometry and/or molecular packing. The unit cell parameters are presented as a function of pressure in Table 3.7. The significant variation in the compression

behaviour of the different samples is particularly evident when all of the unit cell data are presented on one plot, as in Figure 3.27(a)-(d), which includes the unit cell compression of a sample of RDX-d_6 as determined by neutron powder diffraction.[37]

P (GPa)	a (Å)	b (Å)	c (Å)	V (Å^3)	wR_p	R_p	χ^2
2.9	*12.852(4)*	*11.115(3)*	*10.188(3)*	*1455.4(8)*	0.0838	0.0584	1.133
5.8	*12.705(11)* 12.732(5)	*11.002(9)* 9.513(3)	*9.953(7)* 11.133(4)	*1391.2(14)* 1348.4(7)	0.2300	0.1407	29.65
6.7	12.680(4)	9.639(3)	10.979(3)	1341.8(6)	0.1143	0.0704	6.640
8.8	12.566(4)	9.486(3)	10.858(3)	1294.2(7)	0.1255	0.0791	7.033
10.0	12.495(4)	9.408(4)	10.782(4)	1267.5(8)	0.1856	0.1064	13.91
10.8	12.443(4)	9.349(4)	10.723(4)	1247.4(7)	0.1517	0.1001	8.869
13.1	12.283(6)	9.223(5)	10.569(5)	1197.3(10)	0.2197	0.1131	10.57
3.6	*12.844(3)*	*11.010(3)*	*10.046(10)*	*1420.6(5)*	0.1323	0.0957	0.540
5.7	12.622(10)	9.542(11)	11.023(12)	1331.8(15)	0.1757	0.1146	7.125
8.9	12.474(7)	9.372(8)	10.824(8)	1265.4(16)	0.1702	0.1055	6.955
10.6	12.550(6)	9.433(7)	10.840(6)	1283.3(14)	0.1292	0.0945	3.304
11.9	12.309(8)	9.255(10)	10.732(12)	1222.7(14)	0.2164	0.1392	10.06
13.6	12.385(7)	9.284(9)	10.588(90	1217.5(13)	0.2610	0.1570	14.63
15.0	12.182(9)	9.174(9)	10.574(8)	1181.6(19)	0.1543	0.1052	5.162
16.2	12.229(10)	9.093(10)	10.576(10)	1176.1(20)	0.1657	0.1129	6.353
18.8	12.126(10)	9.108(10)	10.479(10)	1157.4(20)	0.1093	0.0864	3.370
20.0	12.130(6)	8.989(6)	10.452(5)	1139.7(11)	0.0903	0.0622	2.205
21.9	11.987(90	8.988(9)	10.365(9)	1116.7(19)	0.1210	0.0897	3.606
23.0	12.083(5)	8.976(5)	10.395(5)	1127.4(10)	0.1436	0.0933	5.045

Table 3.7 Unit cell parameters (a, b, c and V) as determined by Le Bail refinement of the X-ray powder diffraction patterns collected during compression of RDX in MeOH:EtOH. The two compression studies have been separated for clarity. The patterns that have been refined using the α-structure have been italicised, with the pattern at 5.8 GPa being refined as a mixed phase of α- and γ-RDX.

P (GPa)	a (Å)	b (Å)	c (Å)	V (Å^3)	wR_p	R_p	χ^2
15.3	12.052(8)	8.947(7)	10.362(7)	1117.4(14)	0.1247	0.0826	1.267
20.0	11.924(9)	8.861(9)	10.160(9)	1073.5(16)	0.1703	0.1024	2.311
19.7	11.976(8)	8.827(9)	10.188(9)	1077.0(10)	0.1177	0.0769	1.001
18.3	12.038(10)	8.901(10)	10.282(11)	1101.7(19)	0.2104	0.0987	3.024
15.7	12.126(10)	8.958(9)	10.354(13)	1124.6(20)	0.0848	0.0572	0.748
14.0	12.116(9)	9.012(10)	10.355(10)	1130.6(18)	0.3019	0.1691	7.884
11.0	12.271(6)	9.184(7)	10.569(7)	1191.0(8)	0.1237	0.0847	1.185
0.0	*13.195(4)*	*11.593(3)*	*10.706(3)*	*1637.6(7)*	0.1384	0.0974	0.404

Table 3.8 Unit cell parameters (a, b, c and V) as determined by Le Bail refinement of the X-ray powder diffraction patterns collected during compression of RDX in the absence of pressure-transmitting medium. In this experiment, the sample was pre-compressed to 15.3 GPa before the pressure was increased to 20.0 GPa. Subsequent data collections were performed upon decompression.

In order to compare to the equation of state determined for RDX-d_6, the variation in unit cell volume with pressure in each case was fitted to a 3rd-order Birch-Murnaghan EoS, in which V_0 was fixed to the value determined by Oswald *et al*.[39] These are presented as insets in the respective *PV* plots, Figure 3.28. Following the procedure described by Oswald *et al*., equations of state were also refined by fixing B' to be the value determined for the γ-form at lower pressure (*i.e.* 11.26). However, this resulted in unsatisfactorily large uncertainties in the parameters V_0 and B_0 and visual inspection of the data showed that this did not accurately describe the compression behaviour. A direct comparison of the EoS for RDX-h_6 (this study) and RDX-d_6 can also be found in Figure 3.28(c).

Close inspection of the compression behaviour shown in Figure 3.27 and Figure 3.28 shows that there is a marked difference between the study in which no pressure-transmitting medium was employed and the compressions conducted in MeOH:EtOH (I15). The unit cell volumes determined in the non-hydrostatic compression (I11) are consistently lower than those measured at I15, especially at pressures greater than 10 GPa. This is particularly striking evidence of the effect of non-hydrostatic conditions on the crystal structure of the material under investigation. The development of deviatoric strains under these conditions will result in a pressure gradient across the cell. Therefore, the pressures experienced by the sample at the centre of the gasket (*i.e*. the volume being sampled during the X-ray diffraction experiment) will, most likely, be greater than those recorded by the fluoresence of a ruby chip placed near the gasket edge.[90] Furthermore, the broadening of the ruby fluorescence signal under non-hydrostatic compression greatly increases the uncertainty in the pressure

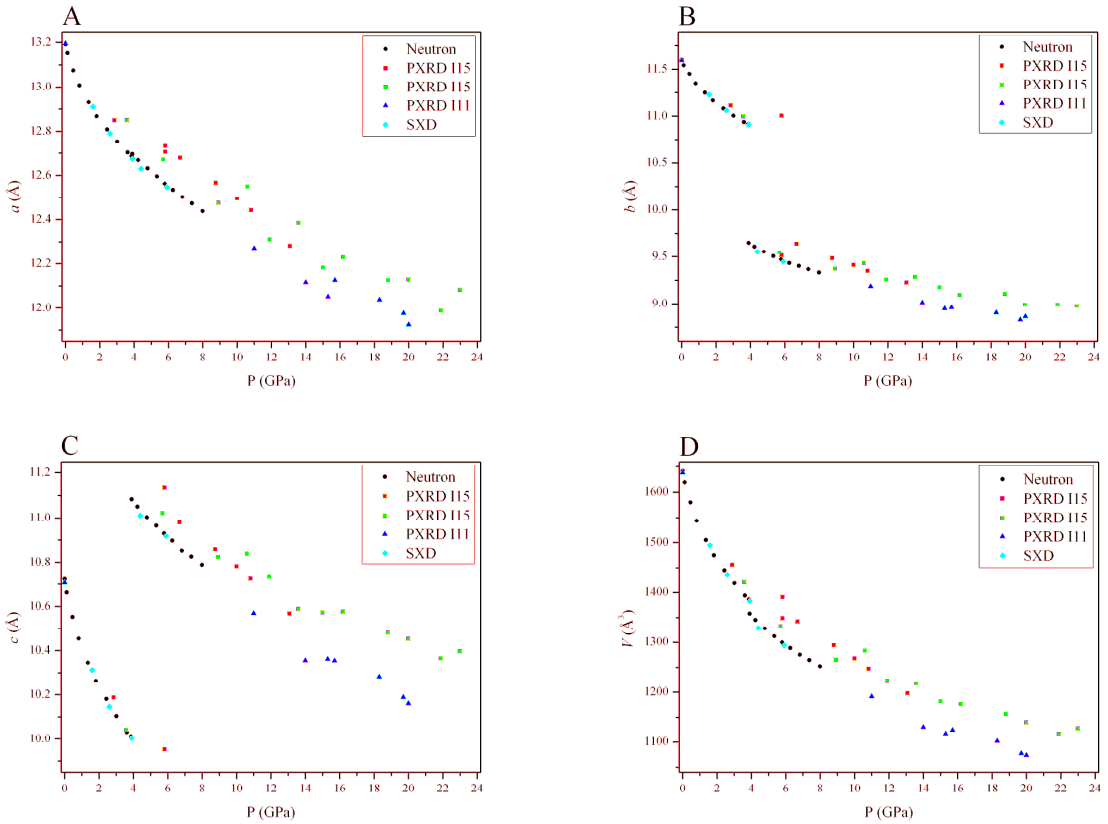

Figure 3.27 Variation in RDX unit cell parameters with pressure, as determined by Rietveld refinement of the X-ray powder diffraction patterns collected during both studies (with MeOH:EtOH and without pressure-transmitting medium). In addition, the unit cell compression of RDX-d_6 as determined by neutron powder diffraction [37] has been included, along with single-crystal X-ray data (SXD) collected on an APEX-II laboratory source (Mo Kα) [60], using MeOH:EtOH as pressure-transmitting medium.

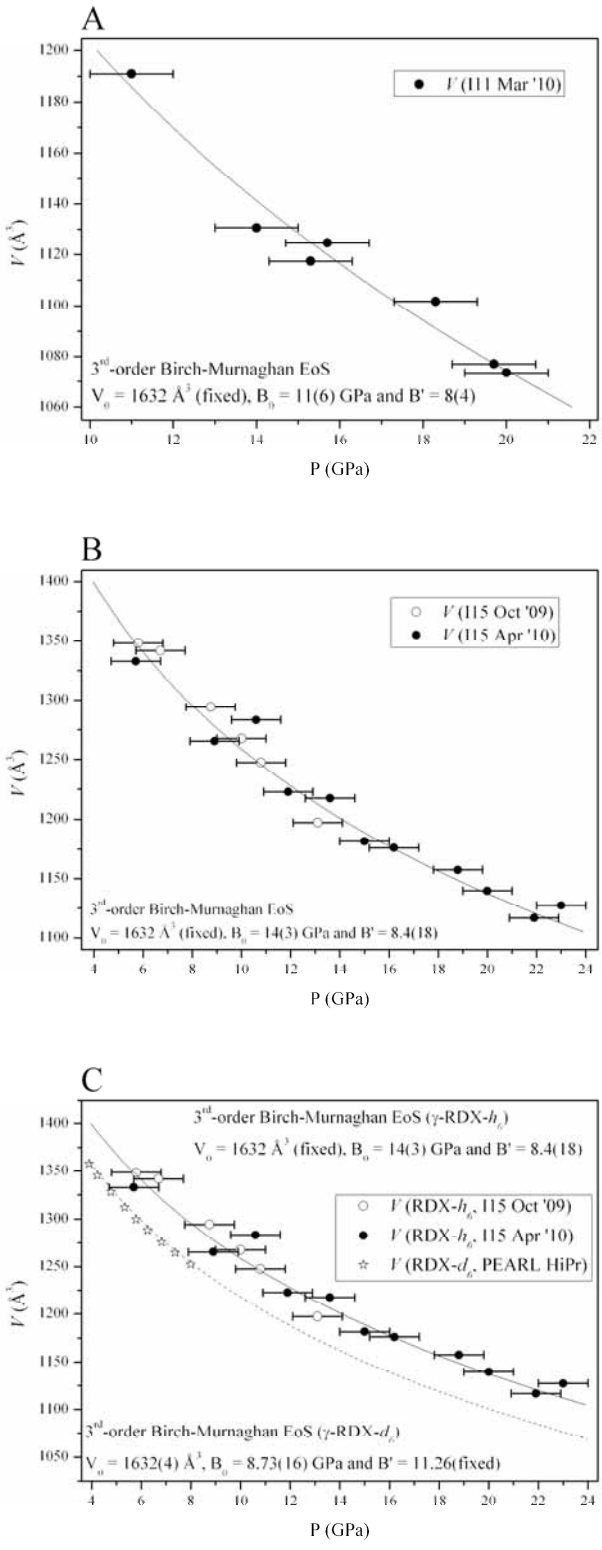

Figure 3.28 Compression of γ-RDX: (a) powder X-ray diffraction (PXRD) study conducted on RDX-h_6 (no pressure-transmitting medium); (b) PXRD study of RDX-h_6 compressed in MeOH:EtOH; and, (c) comparison of the EoS obtained for RDX-h_6 with that for RDX-d_6 reported in [39]. An uncertainty of ±1.0 GPa in the pressure measurements of the current study was used in the least squares refinement of the EoS; errors in V were smaller than the data symbols shown here.

measurement. It was therefore necessary to include a pressure error of ± 1.0 GPa in the least squares refinement of the equations of state (this has been reflected in the *PV*-plots below).

In addition, one may suggest that the influence of the pressure-transmitting medium at these elevated pressures may have greater consequences than has previously been anticipated. For example, it may be the case that the frozen pressure medium results in a pressure-hardening of the sample:medium matrix. An alternative interpretation is that the pressure medium may in fact be interacting with the sample, thus augmenting the sample's inherent resistance to compression. However, it should be noted that no extraneous peaks were observed in the patterns collected during compression indicating that solvate formation did not occur, certainly in the bulk material.

While the bulk moduli determined for the X-ray diffraction experiments are within error of each other [11(6) and 14(3) GPa], it is interesting to note that the B_0 reported by Oswald e*t al.* is significantly smaller [8.73(16) GPa] than the I15 study. This indicates that RDX is perhaps more resistant to compression than previously suggested, particularly in this higher pressure regime. This clearly underlines the importance of conducting compression studies to the highest possible/practicable pressures in order to gain an accurate representation of the structural response to pressure. This is especially true for high-pressure studies of energetic materials since these compounds may experience pressures in the range 10 – 100 GPa during detonation. However, in order to obtain more precise determinations of the bulk modulus (as well as V_0 and B'), it is still essential to obtain high quality diffraction data at minimal pressure. It is clear, therefore, that the current study should complement the existing compression data.

Nevertheless, the most important result of this study is that no evidence of a phase transition to δ-RDX was observed *ca* 18 GPa. It is certainly possible, however, that this phase transition may have been suppressed by the non-hydrostatic conditions, particularly if the transition involves a significant degree of molecular rearrangement. In their spectroscopic study of RDX (at pressures comparable to those recorded in this work), Ciezak *et al.* employed helium[6] as the pressure-transmitting medium, thus ensuring hydrostatic conditions in this pressure regime.[33, 34] At these elevated pressures, however, it may be possible that the helium pressure-transmitting medium may actually have an implict role in the $\gamma \rightarrow \delta$ transition by interacting with or even permeating the crystal lattice. Such a phenomenon has

[6] Helium has been shown to maintain hydrostaticity beyond 20 GPa, despite its pressure-induced solidification at 12.1 GPa. (Klotz *et al*., ref. [14] Chapter 2).

even been observed in MeOH:EtOH recently, whereupon a methanol solvate was formed by the application of pressure alone.[91]

Despite this marked difference in compression behaviour, the current study also complements Ciezak's spectroscopic investigation since it not only highlights the importance of choosing the pressure medium that is most suitable for the desired pressure range but also intimates that the role of the pressure medium should not be underestimated. It would therefore be extremely valuable to conduct a diffraction study of RDX to 20 GPa using He as the pressure medium in order to characterise the $\gamma \rightarrow \delta$ transition fully.

3.6 Conclusions

The structural data presented herein represent a signifcant contribution to the understanding of RDX under extreme conditions and will be valuable to scientists with a wide range of research interests: not only energetic materials but also those interested in understanding molecular compounds under extremes of temperature and/or pressure and the development of high-pressure technology and expertise.

The structure of the highly metastable β-RDX at ambient conditions has been determined – a significant achievement given the elusive nature of this polymorph. Although β-RDX has also been shown to be very prone to transform to the more stable α-form and hence is unlikely to be found in RDX munitions, the reconstructive nature of this transition may have significant implications for sensitivity and performance. The phase history of RDX samples may therefore be an important factor influencing the sensitivity of these samples to initiation.

Furthermore it has been shown that the β-form at ambient conditions is distinct from the high-pressure/high-temperature polymorph with which it has previously been confused. This form has now been re-named ε-RDX and has been structurally characterised by complementary X-ray single-crystal and neutron powder diffraction. The internationally unique capability of rapid heating and cooling *in situ* on the PEARL beamline (a technical development stimulated, in part, by this research programme) was exploited for the recovery of the ε-form to ambient pressure. Structural characterisation at ambient pressure (220 K) has also shown unequivocally that ε-RDX is denser than the α-form and would therefore be expected to exhibit a greater detonation velocity. This result is illustrative of the unrivalled opportunity that high-pressure techniques present for the recovery of novel materials with improved performance without the need for changing molecular structures.

X-ray diffraction studies of RDX have been extended to a pressure of ~20 GPa. Other than the $\alpha \rightarrow \gamma$ transition at 3.9 GPa, no phase transitions were observed although significant

differences in the compressibility of RDX were observed depending on whether a pressure-transmitting medium was used. Given this observation it is reasonable to suggest that δ-RDX may be observed in systems using different media and the pressures at which the γ → δ transition occurs may also be dependent on pressure media.

Finally, this study now allows the crystallographic data for the four polymorphs of RDX that have been structurally characterised to be summarised in Table 3.9.

	α-RDX	β-RDX	γ-RDX [37]	ε-RDX
Space Group	*Pbca*	$Pca2_1$	$Pca2_1$	$Pca2_1$
a (Å)	13.166(4)	15.1267(11)	12.5650(19)	7.519(4)
b (Å)	11.539(4)	7.4563(6)	9.4769(6)	11.643(5)
c (Å)	10.667(3)	14.3719(11)	10.9297(9)	9.177(4)
V (Å^3)	1620.6(5)	1621.0(2)	1301.5(2)	803.4(4)
Z	8	8	8	4
T (K)	220	150	293	220

Table 3.9 Crystallographic data for the four structurally characterised polymorphs of RDX. The data presented for the α-, γ- and ε-forms pertain to perdeuterated samples, while data collections for the β-form were performed on RDX-h_6. All data collections were performed at ambient pressure, except for γ-RDX – these data are correct at 5.2 GPa.

3.7 Suggestions for Further Work

The structural characterisation of the highly metastable β-form of RDX has presented the opportunity to explore, by diffraction methods, the effect that this form and the reconstructive β → α transition have on the crystal quality of commercial samples of RDX. This has obvious implications for performance, particularly sensitivity. It would therefore be extremely valuable to conduct whole powder pattern modelling on high-resolution powder diffraction data collected for not only the β-form but also samples of the α-form that have previously undergone the β → α transition. Comparison of these patterns with data collected for commercial samples of RDX would highlight any factors that may adversely affect performance, such as crystal defects. Such studies may also provide an experimental rationale for the observed insensitivity of RS-RDX, especially if one could reconcile this behaviour with the synthetic procedure. Finally, sensitivity studies should be conducted on these samples in order to provide a definitive assessment of the effect the β-form has on RDX sensitivity.

It would also be extremely valuable to conduct single-crystal X-ray diffraction studies on β-RDX using synchrotron radiation, particularly at very low temperatures. This would certainly facilitate the accurate determination of any disorder that exists within the structure

and will provide high-quality experimental evidence to complement the molecular dynamics simulations conducted in this study. High-temperature powder diffraction studies would also allow the verification of the spectroscopic observations of Infante-Castillo *et al*., who have reported an α → β solid-solid phase transition at 477 K.[28] Comparison of the powder diffraction patterns collected in this way with the simulated pattern calculated using the β-structure would either confirm their assertion or provide evidence for yet another polymorph of RDX. Finally, should it be possible to load a single crystal of β-RDX into a diamond-anvil cell, a high-pressure study of this metastable form may result in further polymorphic transitions that may not be accessible by the compression of α-RDX.

The recovery of ε-RDX to ambient pressure, its stability on warming to 220 K and its greater density (compared to the α-form) means that this represents a tantalising opportunity for revolutionising RDX munitions by the incorporation of a more powerful polymorph. In order to make ε-RDX viable for use in explosive formulation it will be necessary to explore the stabilisation of this high-pressure/high-temperature form, perhaps by the inclusion of an additive as has been successful in the desensitisation of ammonium nitrate (see Section 1.2.2). This doping approach, however, will be far from trivial since the ε-form has only ever been formed at extreme conditions, thus requiring the dopant be included in the sample before it is compressed and heated. Such an addition may dramatically affect the phase behaviour at elevated temperatures and pressures and it is, therefore, extremely difficult to predict the outcome of this experiment. An alternative approach would be to recover a sample of ε-RDX to ambient pressure (at low temperature) by the approach detailed in this work and subsequently perform doping at ambient pressure. This stabilised sample of ε-RDX could then potentially be used to seed batches of RDX to promote the large-scale crystallisation of ε-RDX. Of course, should this be successful, it will be necessary to conduct thorough testing of its thermal stability (primarily with respect to the α-form) as well as its sensitivity and detonation characteristics.

The structural characterisation of the β- and ε-forms at ambient pressure (150 K) now means that it will be possible to conduct density functional theory (DFT) calculations to determine the relative energies of these polymorphs with respect to α-RDX. These calculations will also provide an insight into the barriers to conversion that exist between the forms at ambient pressure. Furthermore, these values may be compared to the theoretically derived energy barriers published by Vladimiroff and Rice.[38]

In addition to the calculation of the relative energies under the same conditions, it would be extremely useful to conduct PIXEL calculations (see Section 1.3.2) to rationalise the phase

transitions at elevated temperatures and pressures.[92] Not only would these calculations provide an important insight into the reversible α → γ transition (at 3.9 GPa), but they would also shed light on the formation of the ε-form at elevated temperatures and pressures. Moreover, the large hysteresis during the decompression of ε-RDX is of particular interest, especially since an ε → γ transition is not observed. It would therefore be extremely interesting to assess the barriers to re-conversion of the ε-form to either γ- or α-RDX.

Finally, an X-ray powder diffraction study of RDX compressed to *ca* 20 GPa in helium is already planned. By re-creating the conditions under which δ-RDX has been observed spectroscopically, it is hoped that structural information on this form can be obtained. This would be a significant achievement as it would not only extend dramatically the pressure range for which the structural characterisation has been achieved for any energetic material but would also represent the completion of the (current) RDX phase diagram.

3.8 References

1. Henning, *German Patent, 104, 280*, 1899
2. Herz, *Swiss Patent, 88, 759*, 1920
3. Herz, *Chem. Zentr.*, 1921, **92**, 926.
4. W.E. Bachmann and J.C. Sheehan, *J.Am. Chem. Soc.*, 1949, **71**, 1842.
5. J. Akhavan, *The Chemistry of Explosives*, Royal Society of Chemistry, Cambridge, UK, 2004, 2nd edn.
6. A. Freche, J. Aviles, L. Donnio, and C. Spyckerelle, *Insensitive RDX (I-RDX)* in *Insensitive Munitions and Energetic Materials Symposium*, 2000, San Antonio, TX, USA.
7. P. Sjöberg, H. Hytti, R. Strandberg, A. Kariniemi, and M. Muilu, *PBX with Insensitive RDX - A New EIDS Substance for Underwater Use* in *International Annual Conference of ICT*, 2002, Karlsruhe, Germany.
8. T. Halvorsen, *Improved RDX, Properties and Processability* in *International Annual Conference of ICT*, 2002, Karlsruhe, Germany.
9. I.J. Lochert, R.M. Dexter, and B.L. Hamshere, *Evaluation of Australian RDX in PBXN-109*, Defence Science and Technology Organisation, Edinburgh, SA, Australia, DSTO-TN-0440, 2002.
10. D. Watt, F. Peugeot, R. Doherty, M. Sharp, D. Topler, and D. Tucker, *Reduced Sensitivity RDX- Where are we?* in *International Annual Conference of ICT*, 2004, Karlsruhe, Germany.
11. R.M. Doherty and D.S. Watt, *Propellants, Explos., Pyrotech.*, 2008, **33**, 4.
12. J.A. Ciezak and S.F. Trevino, *J. Phys. Chem. A*, 2006, **110**, 5149.
13. L. Pacheco-Londoño, W. Ortiz-Rivera, O. Primera-Pedrozo, and S. Hernández-Rivera, *Anal. Bioanal.Chem.*, 2009, **395**, 323.
14. R. Infante-Castillo, L. Pacheco-Londoño, and S.P. Hernández-Rivera, *Spectrochim. Acta, Part A*, 2010, **76**, 137.
15. I.F. Shishkov, L.V. Vilkov, M. Kolonits, and B. Rozsondai, *Struct. Chem.*, 1991, **2**, 57.
16. Y. Oyumi and T.B. Brill, *Combust. Flame*, 1985, **62**, 213.
17. T.R. Botcher and C.A. Wight, *J. Phys. Chem.*, 1994, **98**, 5441.

18. D. Chakraborty, R.P. Muller, S. Dasgupta, and W.A. Goddard, *J. Phys. Chem. A*, 2000, **104**, 2261.
19. E.P.H. Best, K.N. Geter, H.E. Tatem, and B.K. Lane, *Chemosphere*, 2006, **62**, 616.
20. X. Pan, B. Zhang, J.N. Smith, M.S. Francisco, T.A. Anderson, and G.P. Cobb, *Chemosphere*, 2007, **67**, 1164.
21. M. Vila, S. Lorber-Pascal, and F. Laurent, *Environ. Pollut.*, 2007, **148**, 148.
22. C.S. Choi and E. Prince, *Acta Cryst.*, 1972, **B28**, 2857.
23. P. Hakey, W. Ouellette, J. Zubieta, and T. Korter, *Acta Cryst.*, 2008, **E64**, o1428.
24. W.C. McCrone, *Anal. Chem.*, 1950, **22**, 954.
25. R.J. Karpowicz, S.T. Sergio, and T.B. Brill, *Ind. Eng. Chem. Prod. Res. Dev.*, 1983, **22**, 363.
26. R.J. Karpowicz and T.B. Brill, *J. Phys. Chem.*, 1984, **88**, 348.
27. P. Torres, L. Mercado, I. Cotte, S.P. Hernandez, N. Mina, A. Santana, R.T. Chamberlain, R. Lareau, and M.E. Castro, *J. Phys. Chem. B*, 2004, **108**, 8799.
28. R. Infante-Castillo, L.C. Pacheco-Londoño, and S.P. Hernández-Rivera, *J. Mol. Struct.*, 2010, **970**, 51.
29. B. Olinger, B. Roof, and H. Cady, in *Symposium International Sur Le Comportement Des Milieux Denses Sous Hautes Pressions Dynamiques*, 1978, Paris, France.
30. C.S. Yoo, H. Cynn, W.M. Howard, and N. Holmes, *Equations of State of Unreacted High Explosives at High Pressures* in *Proceedings of the 11th International Detonation Symposium*, 1998, USA.
31. B.J. Baer, J. Oxley, and M. Nicol, *High Pressure Res.*, 1990, **2**, 99.
32. P.J. Miller, S. Block, and G.J. Piermarini, *Combust. Flame*, 1991, **83**, 174.
33. J.A. Ciezak, T.A. Jenkins, Z. Liu, and R.J. Hemley, *J. Phys. Chem. A*, 2007, **111**, 59.
34. J.A. Ciezak and T.A. Jenkins, *Propellants, Explos., Pyrotech.*, 2008, **33**, 390.
35. Z.A. Dreger and Y.M. Gupta, *J. Phys. Chem. B*, 2007, **111**, 3893.
36. N. Goto, H. Fujihisa, H. Yamawaki, K. Wakabayashi, Y. Nakayama, M. Yoshida, and M. Koshi, *J. Phys. Chem. B*, 2006, **110**, 23655.
37. A.J. Davidson, I.D.H. Oswald, D.J. Francis, A.R. Lennie, W.G. Marshall, D.I.A. Millar, C.R. Pulham, J.E. Warren, and A.S. Cumming, *CrystEngComm*, 2008, **10**, 162.
38. T. Vladimiroff and B.M. Rice, *J. Phys. Chem. A*, 2002, **106**, 10437.
39. I.D.H. Oswald, D.I.A. Millar, A.J. Davidson, D.J. Francis, W.G. Marshall, C.R. Pulham, A. Cumming, A.R. Lennie, and J.E. Warren, *High Pressure Res.*, 2010, **30**, 280
40. T.D. Sewell, *J. Appl. Phys.*, 1998, **83**, 4142.
41. D.C. Sorescu, B.M. Rice, and D.L. Thompson, *J. Phys. Chem. B*, 1999, **103**, 6783.
42. T.D. Sewell and C.M. Bennett, *J. Appl. Phys.*, 2000, **88**, 88.
43. P.M. Agrawal, B.M. Rice, L. Zheng, and D.L. Thompson, *J. Phys. Chem. B*, 2006, **110**, 26185.
44. E.F.C. Byrd and B.M. Rice, *J. Phys. Chem. C*, 2007, **111**, 2787.
45. M.W. Conroy, I.I. Oleynik, S.V. Zybin, and C.T. White, *J. Appl. Phys.*, 2008, **104**, 113501.
46. M.S. Miao, Z.A. Dreger, J.M. Winey, and Y.M. Gupta, *J. Phys. Chem. A*, 2008, **112**, 12228.
47. D.C. Sorescu and B.M. Rice, *J. Phys. Chem. C*, 2010, **114**, 6734.
48. S. Grimme, *J. Comput. Chem.*, 2006, **27**, 1787.
49. V. Barone, M. Casarin, D. Forrer, M. Pavone, M. Sambi, and A. Vittadini, *J. Comput. Chem.*, 2009, **30**, 934.
50. J.E. Patterson, Z.A. Dreger, and Y.M. Gupta, *J. Phys. Chem. B*, 2007, **111**, 10897.
51. Z.A. Dreger, J.E. Patterson, and Y.M. Gupta, *J. Phys.: Conf. Ser.*, 2008, **121**, 042012.

52. M. Miao, Z.A. Dreger, J.E. Patterson, and Y.M. Gupta, *J. Phys. Chem. A*, 2008, **112**, 7383.
53. J.E. Patterson, Z.A. Dreger, M. Miao, and Y.M. Gupta, *J. Phys. Chem. A*, 2008, **112**, 7374.
54. S. Bulusu, J. Autera, and T. Axenrod, *J. Labelled Compd. Radiopharm.*, 1980, **17**, 707.
55. J.M. Besson, R.J. Nelmes, G. Hamel, J.S. Loveday, G. Weill, and S. Hull, *Physica B*, 1992, **180-181**, 907.
56. W.G. Marshall, D.J. Francis, C.J. Barry, O. Kirichek, C.R. Pulham, and M.G. Tucker, *manuscript in preparation*, 2010.
57. W.G. Marshall and D.J. Francis, *J. Appl. Crystallogr.*, 2002, **35**, 122.
58. A.D. Fortes, PhD Thesis, 2004, Department of Earth Sciences, University College, London, UK.
59. R. Von Dreele and A.C. Larson, *General Structure Analysis System (GSAS)*, 1986.
60. Bruker-Nonius, *APEX-II*, Bruker-AXS, Madison, WI, USA, 2000.
61. J. Cosier and A.M. Glazer, *J. Appl. Crystallogr.*, 1986, **19**, 105.
62. A. Altomare, G. Cascarano, C. Giacovazzo, A. Guagliardi, M.C. Burla, G. Polidori, and M. Camalli, *J. Appl. Crystallogr.*, 1994, **27**, 435.
63. P.W. Betteridge, J.R. Carruthers, R.I. Cooper, K. Prout, and D.J. Watkin, *J. Appl. Crystallogr.*, 2003, **36**, 1487.
64. L. Merrill and W.A. Bassett, *Rev. Sci. Instrum.*, 1974, **45**, 290.
65. S.A. Moggach, D.R. Allan, S. Parsons, and J.E. Warren, *J. Appl. Crystallogr.*, 2008, **41**, 249.
66. G.J. Piermarini, S. Block, J.D. Barnett, and R.A. Forman, *J. Appl. Phys.*, 1975, **46**, 2774.
67. A. Dawson, D.R. Allan, S. Parsons, and M. Ruf, *J. Appl. Crystallogr.*, 2004, **37**, 410.
68. Bruker-AXS, *SAINT*, Bruker-AXS, Madison, WI, USA, 2003.
69. S. Parsons, *SHADE, Program for Empirical Absorption Corrections to High Pressure Data*, The University of Edinburgh, UK, 2004.
70. G.M. Sheldrick, *SADABS*, University of Göttingen, Germany, 2004.
71. A.P. Hammersley, S.O. Svensson, M. Hanfland, A.N. Fitch, and D. Hausermann, *High Press. Res.*, 1996, **14**, 235
72. CPMD, 2008, IBM Corp. 1990-2008 and MPI für Festkörperforschung Stuttgart 1997-2001.
73. J.P. Perdew, K. Burke, and M. Ernzerhof, *Phys. Rev. Lett.*, 1996, **77**, 3865.
74. M. Elstner, P. Hobza, T. Frauenheim, S. Suhai, and E. Kaxiras, *J. Chem. Phys.*, 2001, **114**, 5149.
75. A.M. Reilly, PhD Thesis, 2009, School of Chemistry, University of Edinburgh.
76. J.S. Capes and R.E. Cameron, *Cryst. Growth. Des.*, 2006, **7**, 108.
77. A.M. Reilly, S. Habershon, C.A. Morrison, and D.W.H. Rankin, *J. Chem. Phys.*, 2010, **132**, 094502.
78. A.M. Reilly, S. Habershon, C.A. Morrison, and D.W.H. Rankin, *J. Chem. Phys.*, 2010, **132**, 134511.
79. D.D. Dlott and M.D. Fayer, *J. Chem. Phys.*, 1990, **92**, 3798.
80. L.N. Erofeev, Y.P. Tarasov, Y.B. Kalmykov, Y. Shu, V.V. Dubikhin, and G.M. Nazin, *Russ. Chem. Bull.*, 2001, **50**, 1000.
81. P. Scardi and M. Leoni, *Acta Cryst.*, 2002, **A58**, 190.
82. M. Herrmann, *Part. Part. Syst. Charact.*, 2005, **22**, 401.
83. Z.A. Dreger and Y.M. Gupta, *J. Phys. Chem. A*, 2010, **114**, 7038.
84. Z.A. Dreger and Y.M. Gupta, *J. Phys. Chem. A*, 2010, **114**, 8099.
85. F.P.A. Fabbiani, D.R. Allan, W.I.F. David, S.A. Moggach, S. Parsons, and C.R. Pulham, *CrystEngComm*, 2004, **6**, 505.

86. F.P.A. Fabbiani, D.R. Allan, S. Parsons, and C.R. Pulham, *CrystEngComm*, 2005, **7**, 179.
87. D.I.A. Millar, I.D.H. Oswald, D.J. Francis, W.G. Marshall, C.R. Pulham, and A.S. Cumming, *Chem. Commun.*, 2009, **45**, 562.
88. D.I.A. Millar, I.D.H. Oswald, C. Barry, D.J. Francis, W.G. Marshall, C.R. Pulham, and A.S. Cumming, *Chem. Commun.*, 2010, **46**, 5662.
89. R.J. Angel, M. Bujak, J. Zhao, G.D. Gatta, and S.D. Jacobsen, *J. Appl. Crystallogr.*, 2007, **40**, 26.
90. Y. Shen, R.S. Kumar, M. Pravica, and M.F. Nicol, *Rev. Sci. Instrum.*, 2004, **75**, 4450.
91. D.I.A. Millar, W.G. Marshall, H.E. Maynard-Casely, C.R. Pulham, and A.S. Cumming, *unpublished results,* 2010.
92. A. Gavezzotti, *Z. Kristallogr.*, 2005, **220**, 499.

Chapter 4

High-Pressure Structural Studies of CL-20

(2,4,6,8,10,12-hexanitrohexaazaisowurtzitane)

4 High-Pressure Structural Studies of CL-20

4.1 Introduction

2,4,6,8,10,12-hexanitrohexaazaisowurtzitane (HNIW, more commonly known as CL-20 after the China Lake Research Facility, USA) was first synthesised in the late 1980s [1] although the detailed synthetic procedure was only published in 1998.[2] CL-20 is a polycyclic nitramine with six nitro groups bonded to an isowurtzitane cage (see Figure 4.1). The low ratio of carbon atoms to nitramine moieties, combined with the inherent strain in the isowurtzitane cage and the increased density (with respect to its monocyclic analogue) have led to CL-20 being characterised as "the densest and most energetic explosive known."[3] It is not surprising therefore that a significant amount of research has been aimed at assessing its explosive performance [4], sensitivity [5] and thermal properties.[6-8] Furthermore spectroscopic and diffraction techniques have been used to explore the rich polymorphism of CL-20.

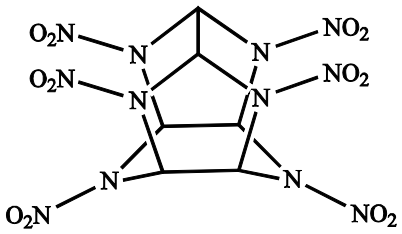

Figure 4.1 Molecular structure of CL-20.

4.2 Polymorphism of CL-20

4.2.1 Ambient-Pressure Studies

Four forms of CL-20 (α, β, γ, and ε) have been characterised at ambient conditions using FTIR spectroscopy and/or single-crystal X-ray diffraction [9-12], although it was only with the publication of the synthetic procedure that detailed structural information entered the open literature.[2] It is important to note, however, that the α-form is actually stabilised by varying amounts of water (0.25 – 0.57) [2, 13, 14] and is therefore not a true polymorph of CL-20 but a hydrate. Since it is common in the literature not to remove the water from the α-form prior to analysis, references to 'α-CL-20' should be taken to mean the 'α-hydrate' unless otherwise specified.

Of the 24 possible conformers elegantly summarised by Foltz *et al.* [6], steric hindrance and the mutual repulsion of the nearest oxygen atoms mean that only eight conformers are considered to be stable. Four of the most stable conformations, as determined by DFT

calculations [15], are represented in Figure 4.2 and it is interesting to note that three of these correspond to the molecular conformations found in the four structurally characterised forms: α and γ share the molecular conformation shown in II, β-CL-20 has been found to adopt the conformation I, while the ε-form exhibits conformation III.

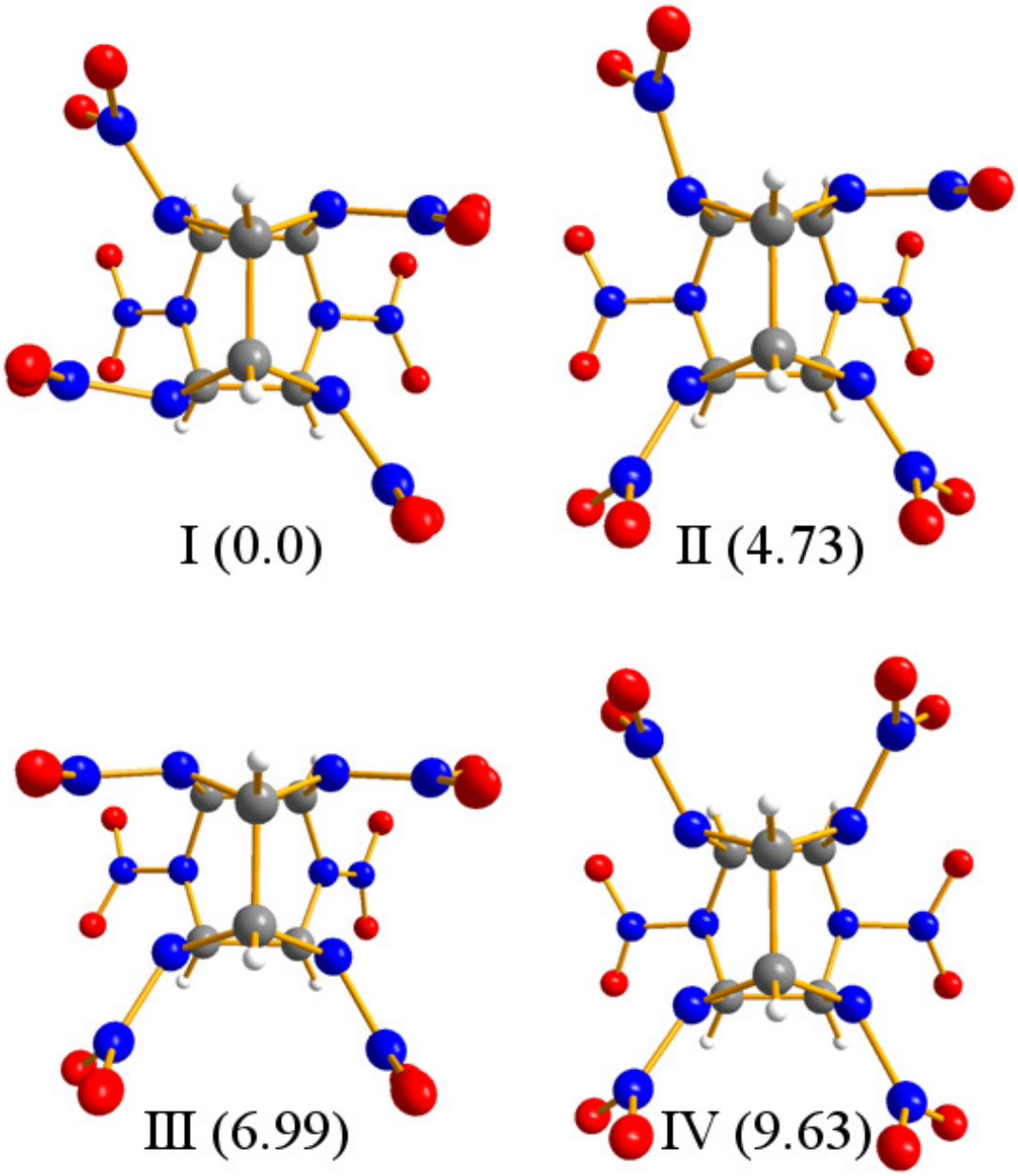

Figure 4.2 The most stable molecular conformations (including the relative energies, in kJ mol^{-1}, calculated by Kholod *et al*. [15]), three of which represent the molecular conformations of the known forms of CL-20. The conformation shown in I is adopted by β-CL-20, II is exhibited in both α- and γ-CL-20, while the ε-form adopts conformation III. It has also been proposed that the high-pressure ζ-form adopts the conformation shown in IV.

	α-CL-20[1]	β-CL-20[2]	γ-CL-20	ε-CL-20
Space Group	*Pbca*	$Pb2_1a$	$P2_1/n$	$P2_1/n$
a (Å)	9.485(2)	9.676(2)	13.231(3)	8.852(2)
b (Å)	13.225(4)	13.006(4)	8.170(2)	12.556(3)
c (Å)	23.673(3)	11.649(4)	14.876(3)	13.386(3)
β (°)			109.17(2)	106.82(2)
V (Å^3)	2969.5(11)	1466.0(10)	1518.9(8)	1424.2(8)
Z	8	4	4	4
D_c (Mg m^{-3})	1.981	1.985	1.916	2.044

Table 4.1 Summary of the crystallographic data for the four forms of CL-20 isolated at ambient temperature and pressure, as determined by Nielsen et al.[2] [1]α-CL-20 in this study refers to 1:0.25 CL-20:H_20. [2]A more conventional selection of $Pca2_1$ was made by Jacob *et al.* in their private communication to the CSD.[13]

This rich polymorphism at ambient conditions presents a significant complication for the commercial applications of CL-20 as a high explosive and for its industrial scale-up. For example, conversion to lower density phases will lead to volume expansion and stress-cracking with implications for sensitivity.[6] There has therefore been a considerable amount of research on characterising these forms, [16] their respective optimum crystallisation conditions [17-19], and their relative stabilities.[20] Thermal analyses [6, 7], kinetic studies using vibrational spectroscopy [8, 21] and DFT calculations [15, 22] have concluded that the ε-form is the most thermodynamically stable polymorph under ambient conditions, although measurements on the α-hydrate were complicated by the inclusion of water molecules.[23-25]

While ε-CL-20 has been shown to be the thermodynamically most stable form, and is therefore often precipitated as the final product of the synthetic procedure, it is possible to obtain the other polymorphs by re-crystallisation methods. For example, high quality crystals of the β-form were obtained by recrystallisation of the crude product in benzene [2] and high-boiling solvents, such as octane.[26] The crystallisation of the α-form, with varying degrees of hydration, is most commonly achieved by recrystallisation from concentrated nitric acid [2] but it has recently been shown to be possible to obtain large crystals of the α-form by the slow evaporation of a 'solution of γ-CL-20 dissolved in wet ethyl acetate'.[24] The water molecules may be removed from the α-CL-20 by prolonged heating ca 373 K, although Russell *et al.* comment that the direct preparation of anhydrous samples of the α-form has not been achieved.[20]

Upon heating, the α-, β-, and ε-forms all undergo an endothermic transition to the γ-form in the range 428 – 471 K.[27] Indeed, spectroscopic analysis of the high-temperature conversion of a sample of β-CL-20 contaminated with some of the α-form confirmed that this resulted in a phase transition to the γ-form, and not to a reported δ-form.[7] Irrespective of the starting polymorph, this high-temperature γ-form is then sufficiently stable to be recovered to ambient temperature.

4.2.2 High-Pressure Studies

Previous high-pressure studies have been reported for the ε-form (the most thermodynamically stable form at ambient conditions) and the γ-form. No experimental studies on the compression of the α- or β-forms have so far been published although the β-form has been included in the most recent computational study by Sorescu *et al.*[28]

ε-CL-20

The compression of polycrystalline ε-CL-20 has been studied by both X-ray powder diffraction [29-31] and Raman spectroscopy.[32] In their diffraction study, Gump *et al.* observed no phase transitions within the pressure range studied (up to 5.6 GPa at ambient temperature). The compression of the unit cell axes was not uniform, with the *b*-axis being ~ 2% more compressible over the whole pressure range. The ε-form was also observed to persist to 5 GPa (the maximum pressure studied) when the compression was carried out at 348 K and at 413 K, provided the sample was initially pressurised (to ~ 0.4 GPa) before heating to avoid the ε → γ thermal transition at ambient pressure.

The pressure range for this investigation was later extended by Ciezak *et al.* who used vibrational spectroscopy to examine the response of ε-CL-20 to compression to 27 GPa. Intensity changes and discontinuities in the pressure shifts of the vibrational modes led the authors to conclude that a sluggish transition from the ε-form to the γ-form occurred between 4.5 and 6.4 GPa. The authors also noted the existence of another transition that begins near 14.8 GPa but is not completed until 18.7 GPa. This phase transition results in the fifth polymorph of CL-20: ζ-CL-20.

γ-CL-20

The high-pressure ζ-form (obtained above 18 GPa by compression of the ε-form) has been shown to exist at much lower pressure when the γ-form is used as the starting material. The behaviour of γ-CL-20 under extreme conditions has been much more fully explored than for the ε-form. Russell *et al.* [20] used optical microscopy and infrared spectroscopy to assemble a pressure/temperature phase diagram in which the stability regions of all five forms of CL-

20 have been plotted along with the reversibility of the polymorphic transitions and the thermal decomposition region at elevated pressures. These results have been summarised in Figure 4.3.

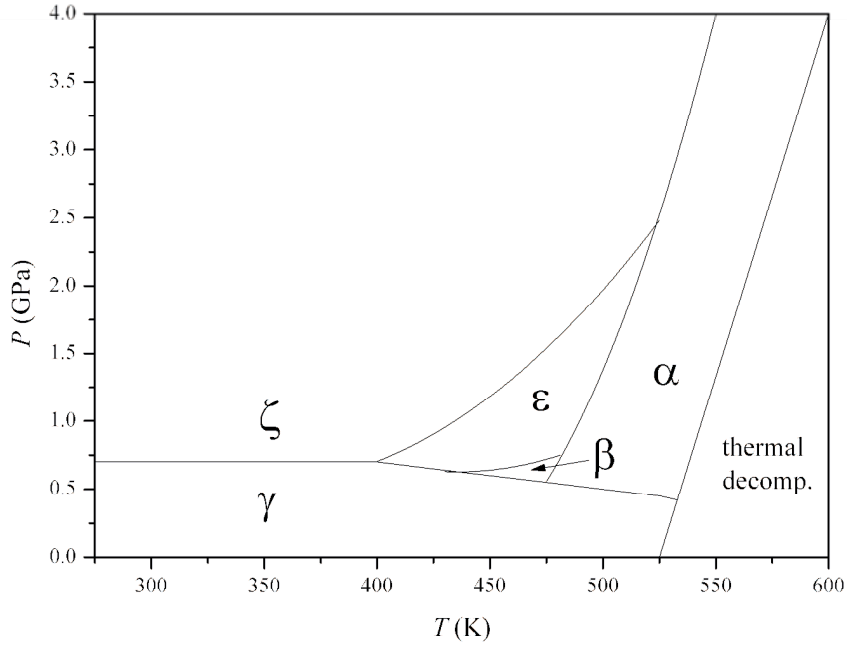

Figure 4.3 The pressure/temperature phase diagram for γ-CL-20 as determined by Russell *et al*. based on FTIR and optical polarising microscopy measurements using γ-CL-20 as starting material.

Moreover, Russell *et al.* investigated the high-pressure transition from γ-CL-20 to the ζ-form using energy dispersive X-ray powder diffraction.[12] In a further study, single crystals of the γ-form were also observed by optical microscopy to undergo a rapid and reversible transition to the ζ-form at 0.7 GPa and survive intact.[20] Comparison of the IR spectra for this high-pressure form with those for the α-, β-, and ε-forms confirmed that this was indeed a fifth form of CL-20. They observed fewer bands in the IR spectrum of ζ-CL-20 and therefore suggest that the ζ-form adopts a molecular conformation with higher symmetry. This observation is consistent with the results of DFT calculations on the different possible molecular conformations of isolated molecules of CL-20 - the fourth stable conformation depicted in Figure 4.2, in which all of the nitro groups adopt *exo*-orientations, has been proposed to correspond to the high-pressure ζ-form.[15] The pressure-induced transition to the ζ-form was also observed at 0.7 GPa in the diffraction study by Gump *et al*. They note that the '*X-ray patterns for this phase are similar to those of the ε phase, but not exactly the same*.'[29]

4.3 Aims

The importance of a detailed knowledge of the structure of CL-20 under extreme conditions has motivated an investigation into the high-pressure behaviour of both the ε- and γ-forms. The primary aims were therefore:

- to study the compression of ε-CL-20, in order to probe the nature of the proposed ε → γ transition;
- to obtain high-quality diffraction data to facilitate the calculation of an improved equation of state of ε-CL-20; and
- to compress γ-CL-20 into the high-pressure ζ-form in order to structurally characterise the fifth form of CL-20.

4.4 Experimental

4.4.1 Materials

Crystalline samples of ε-CL-20 were obtained from Dstl. Powder samples and single crystals of the γ-form were prepared by heating the ε-form to *ca* 470 K and by crystallisation from hot benzene, respectively. The phase purity of such samples of γ-CL-20 was confirmed by Raman spectroscopy and X-ray powder diffraction.

4.4.2 High-Pressure X-ray Powder Diffraction

High-pressure X-ray powder diffraction experiments were carried out using a Merrill-Bassett diamond-anvil cell (DAC) [33] equipped with 600 μm culet diamonds and a 250 μm thick tungsten gasket (pre-indented to a thickness of 100-150 μm) with a 300 μm hole. Pressure measurement was made by monitoring the R_1 fluorescence line of ruby spheres.[34] Compression of ε-CL-20 was undertaken using methanol:ethanol (4:1) as a pressure-transmitting medium; γ-CL-20 was compressed using Fluorinert FC-77 and MeOH:EtOH as pressure media. Data were collected at the Extreme Conditions Beamline (I15) at Diamond Light Source (λ = 0.48469 Å). The X-ray beam was collimated to a diameter of 50 μm and samples were exposed for 60 s. 2D diffraction patterns were collected using a Mar345 image plate, processed using FIT2D.[35] The powder diffraction data were utilised by the program FOX [36] that employed direct space global optimisation methods for structure solution of ζ-CL-20. Full-profile Rietveld refinements were carried out on all powder diffraction patterns using GSAS, in which a convolution of Gaussian (GU, GV), Lorentzian (LX, LY) and asymmetry (asym) coefficients was implemented to fit peak profiles (GSAS CW profile 2).[37]

4.4.3 High-Pressure Neutron Powder Diffraction

High-pressure neutron powder diffraction data were collected using the PEARL/HiPr diffractometer at the UK spallation neutron source, ISIS, at the STFC Rutherford Appleton Laboratory. Due to the complexity of the synthetic procedure, it was not possible to obtain a deuterated sample of CL-20 for these studies. It was therefore necessary to load a lightly ground sample of CL-20-h_6 into an encapsulated TiZr gasket [38] with perdeuterated methanol:ethanol (4:1) as pressure medium and Pb as pressure calibrant. The capsule assembly was then compressed with a type V3b Paris-Edinburgh (P-E) press equipped with standard single toroid anvils with cemented WC cores (Ni binder).[39] The P-E press ram pressure was monitored and varied by means of a computer-controlled hydraulic system.

Time-of-flight (ToF) neutron powder diffraction data were collected using the $2\theta = 90°$ detectors with a transverse (through-anvil) scattering geometry. The resulting summed pattern was then normalised with respect to the incident beam monitor and the scattering from a standard vanadium calibration sample. Lastly, the diffraction pattern intensity scale was corrected for the wavelength and scattering-angle dependence of the neutron attenuation by the anvil (WC) and gasket (TiZr) materials. Full-profile Rietveld refinements of the ToF neutron powder diffraction patterns were carried out using the GSAS package, in which a convolution of Gaussian (with coefficient σ_1) and Lorentzian (γ_1) functions was used to describe peak profiles (GSAS ToF profile 3).[37]

4.4.4 High-Pressure Single-Crystal X-ray Diffraction

High pressures were attained using a Merrill-Bassett diamond-anvil cell (DAC) [33] equipped with 600 μm culet diamonds and a 250 μm thick tungsten gasket (indented to ~100 μm) with a 300 μm diameter hole. In order to maximise the volume of reciprocal space that could be sampled it was necessary to use Böhler-Almax type diamonds and WC backing plates [40] that provide a wider opening angle than the typical beryllium backed DACs. Single crystals of γ-CL-20 were loaded into a DAC with either Fluorinert FC-77 or MeOH:EtOH (4:1) as the pressure-transmitting medium. Accurate determination of sample pressure was measured by the ruby fluorescence method [34] using a 632.8 nm excitation line from a He-Ne laser. The fluorescence was detected by a Jobin-Yvon LabRam 300. High-pressure data sets were collected using ω-scans in 12 settings of 2θ and φ with 0.3° step-size for 30 s.[41] X-ray diffraction intensities were collected using Mo-Kα radiation on a Bruker SMART APEX II CCD diffractometer.[42] Single-crystal data were processed according to the procedure described by Dawson *et al*.[41] Integration of data sets and global cell refinement was carried out using the program SAINT [43], in which 'dynamic masks'

were employed to prevent integration of areas of the detector shaded by the body of the DAC. SHADE [44] was used to reject reflections partly shaded by the DAC and absorption corrections were applied by SADABS [45] to allow for different path-lenghts of the X-rays through the crystal, depending on its orientation during the scan. In the case of ζ-CL-20, structure solution *via* direct methods was not possible and it was therefore necessary to use the program FOX [36] that employs direct space global optimisation methods. All other structures were solved by direct methods using SIR92 [46] and full-matrix least-squares-refinement against *F* were carried out using CRYSTALS.[47] All non-hydrogen atoms were refined anisotropically. The hydrogen atoms were geometrically placed on the parent carbon.

4.4.5 Ambient-Pressure Single-Crystal X-ray Diffraction

X-ray diffraction intensities were collected by Dr F. White (Crystallography Service, University of Edinburgh) using Cu-Kα radiation on an Oxford Diffraction SuperNova dual wavelength diffractometer equipped with an Atlas CCD detector and an Oxford Cryostream-*Plus* low-temperature device (100 K).[48] Data were integrated and a multi-scan absorption correction was applied using the CrysAlis Pro software package.[49] Structures were solved [46] and refined by full-matrix least squares against F^2 using all data.[47] All non-hydrogen atoms were refined anisotropically. The hydrogen atoms were geometrically placed on the parent carbon.

4.5 Results and Discussion

4.5.1 Compression of ε-CL-20

The initial focus of this study was to obtain high-quality X-ray powder diffraction data on ε-CL-20 in order to extend the pressure range of previous diffraction studies [29-31] to ~ 7 GPa thus allowing the critical examination of the proposed transition to the γ-form observed spectroscopically.[32] Polycrystalline ε-CL-20 was loaded into a diamond-anvil cell with methanol:ethanol (4:1) as the pressure-transmitting medium. X-ray powder diffraction patterns collected during the compression experiment at the Extreme Conditions Beamline (I15), Diamond Light Source, are shown in Figure 4.4. It was possible to carry out Rietveld refinements on all of the patterns collected (up to the maximum pressure studied) using the ε-CL-20 structural model – Figure 4.5 shows the quality of the Rietveld refinement for the pattern collected at 7.22 GPa. This is conclusive proof that the ε-form remains stable in this pressure regime and does not undergo a phase transition between 4.5 and 6.4 GPa as has been previously asserted.[32]

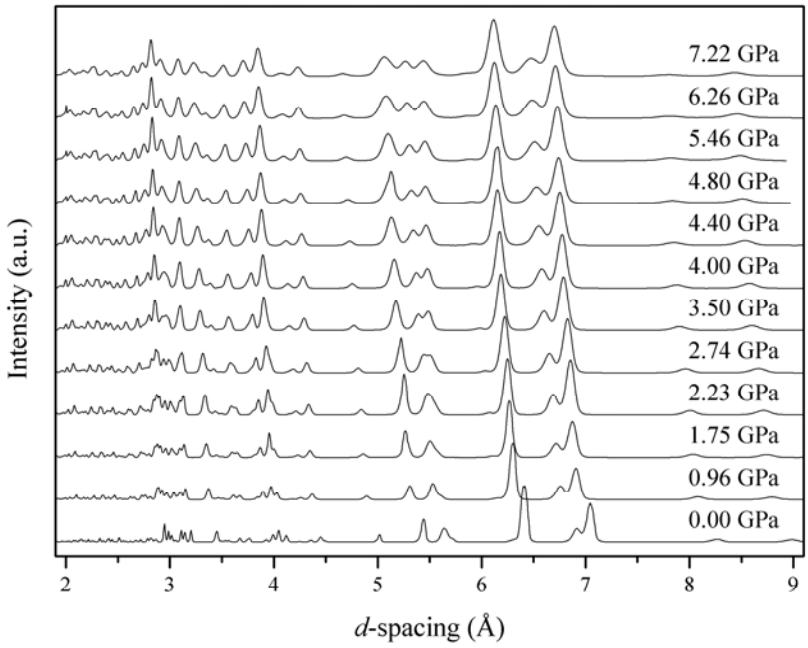

Figure 4.4 Series of X-ray powder diffraction patterns collected during the compression of ε-CL-20 to a maximum pressure of 7.22 GPa.

The variations in the unit cell parameters (*a*, *b*, *c*, *β* and *V*) are tabulated in Table 4.2 and represented graphically in Figure 4.6. The compression behaviour of the unit cell axes is broadly in agreement with that observed by Gump *et al.*: the *b*-axis is most compressible (~ 7%) and the differences in the compressibility of the *a*- and *c*-axes is within the experimental error of both studies. It is interesting to note that the gradient of the relative contraction of the unit cell volume (Figure 4.6(c)) appears to decrease *ca* 5.0 GPa. This may be indicative of a subtle adaptation of either the compression mechanism or, indeed, the structure itself in this pressure regime. Since it has been possible to perform full-profile Rietveld refinements of all the subsequent patterns using the ε-structure, it would appear that this is not evidence of a phase transition. Furthermore, characteristic diffraction peaks arising from the γ-form were not observed.

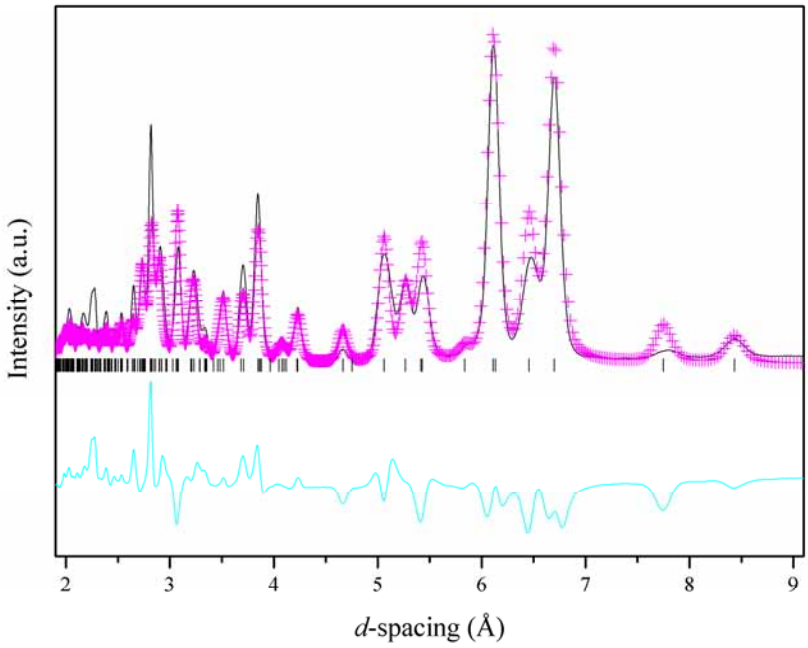

Figure 4.5 Rietveld refinements of the X-ray powder diffraction pattern collected at 7.22 GPa (using ε-CL-20 as the structural model, black tick marks). The experimental data (I_{obs}) are represented as pink crosses, the calculated pattern (I_{calc}) is shown in black and the difference (I_{obs} - I_{calc}) in cyan.

Previous observations of a phase transition to the γ-form at this pressure have been limited to discontinuities in the d$\bar{\nu}$/dP plots and the appearance of new spectral bands in the vibrational spectra. Upon close inspection of these data, however, it is suggested that these features have resulted simply from the resolution of peaks due to the relative hardening or softening of the vibrational modes at elevated pressures. Nevertheless, the change in the gradient of the relative contraction of the unit cell volume, coupled with this spectroscopic evidence, suggests that there is a modification to the intermolecular interactions at these pressures. Further investigation of the ε-form in this pressure regime would therefore be particularly worthwhile.

The compression of the unit cell volume has been fitted to a 3rd-order Birch-Murnaghan equation of state (EoS) with V_0 = 1431.8 Å^3 (fixed), B_0 = 9.5(22) GPa and B'_0 = 27(8). The high-quality of the Rietveld refinement of the pattern collected at 0.0 GPa in this study meant that it was possible to fix V_0, in order to increase the precision of the other parameters. The value of the isothermal bulk modulus (B_0) is smaller than that determined experimentally by Gump *et al.* [31] and the value calculated by Sorescu *et al.*, who used

molecular dynamics simulations [50] (13.6(20)[7] and 15.58 GPa, respectively). However, the pressure derivative (B') is larger (11.7(32) and 9.37, respectively). This indicates that the unit cell volume initially decreases more rapidly in the current study before becoming more resistant to compression.

P (GPa)	a (Å)	b (Å)	c (Å)	β (°)	V (Å^3)	wR_p
0.00	8.8667(3)	12.6020(5)	13.3912(6)	106.891(2)	1431.77(13)	0.049
0.96	8.7010(10)	12.2946(13)	13.1268(16)	106.332(7)	1347.6(4)	0.097
1.75	8.6596(11)	12.2013(16)	12.0443(15)	106.090(10)	1324.2(2)	0.213
2.23	8.6420(14)	12.1552(18)	13.008(2)	105.963(9)	1313.7(5)	0.151
2.74	8.6089(16)	12.077(2)	12.938(2)	105.750(10)	1294.7(7)	0.145
3.50	8.565(2)	11.971(3)	12.845(3)	105.401(14)	1269.9(7)	0.174
4.00	8.540(2)	11.919(3)	12.794(2)	105.24(2)	1256.7(3)	0.229
4.40	8.529(2)	11.873(4)	12.764(5)	105.00(3)	1248.5(11)	0.243
4.80	8.514(4)	11.825(5)	12.734(5)	104.82(3)	1239.5(11)	0.230
5.46	8.503(4)	11.788(6)	12.711(6)	104.62(3)	1233.0(11)	0.259
6.26	8.491(5)	11.743(6)	12.689(9)	104.47(3)	1225.2(14)	0.233
7.22	8.477(6)	11.700(7)	12.658(7)	104.39(3)	1216.1(17)	0.238

Table 4.2 Variation in the unit cell parameters of ε-CL-20 with pressure.

[7] Although the experimental values are within the limits of experimental error of each other, it is believed that the current study does indeed represent a smaller value of B_0. However, it would be extremely desirable to obtain more compression data, particularly in the low pressure (0 – 1 GPa) regime, in order to increase the precision of this value.

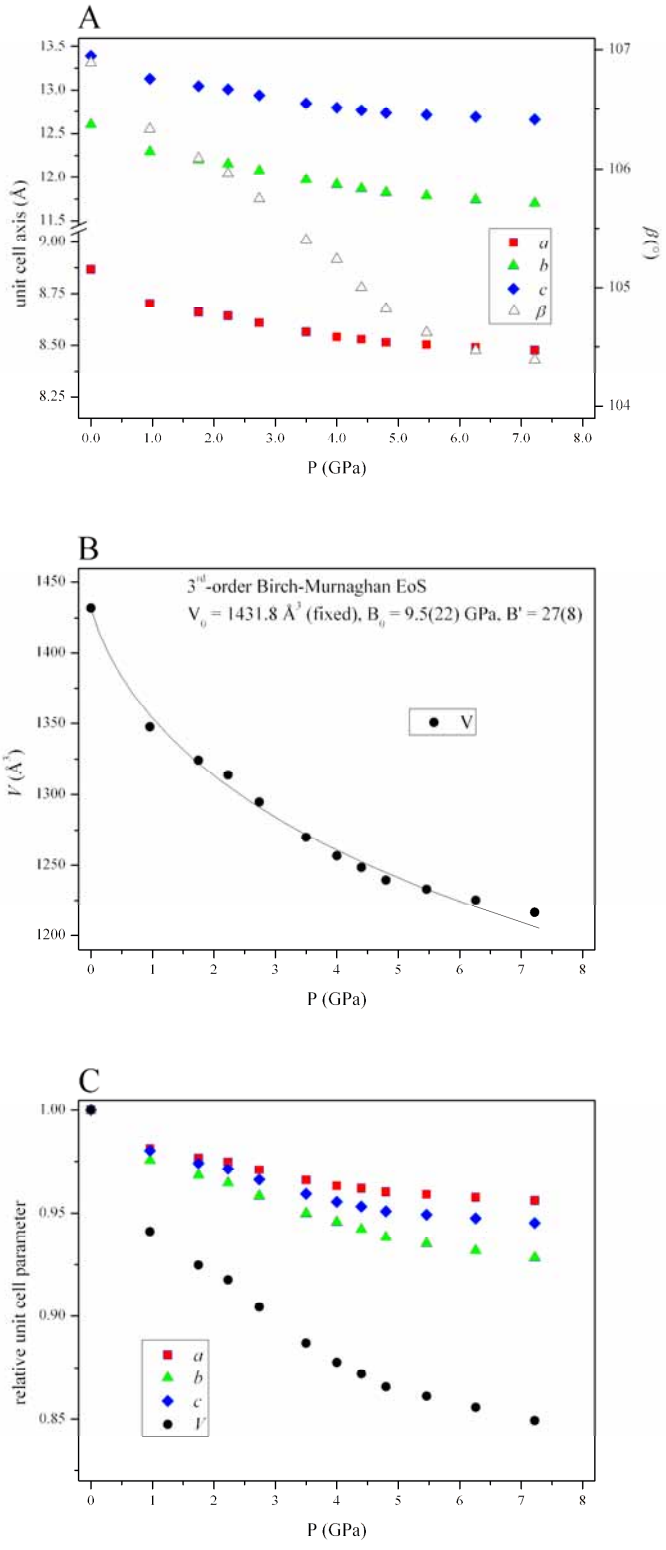

Figure 4.6 (a) Compression of the unit cell parameters (*a*, *b*, *c* and *β*) of ε-CL-20; (b) compression of the unit cell volume, fitted to a 3rd-order Birch-Murnaghan EoS; and, (c) relative contraction of the unit cell parameters.

A more significant observation, however, is that the unit cell volume is larger throughout this study than in any other experimental or theoretical study previously reported. In addition to the equations of state determined by Gump *et al.* and Sorescu *et al.*, recent DFT-D calculations have been conducted by Sorescu and Rice to determine the unit cell parameters at elevated pressure. These data are also presented in Figure 4.7.

The exact reason for this discrepancy is currently unclear. Gump and Peiris have assimilated three experimental compression studies into one table and it has therefore not been possible to plot each compression individually.[31] This would have facilitated the analysis of the relatively large scatter in the data and the identification of any experimental factors that could have contributed to this large variance. Furthermore, the determination of the unit cell parameters was based on indexings obtained from Gaussian fits of individual diffraction peaks (to determine *d*-spacings) rather than Rietveld refinement of the whole diffraction pattern (as in the present work). This is reflected in the relative errors of the two studies: the average uncertainty in the unit cell volume in Gump's study was ± 6.65 Å^3 compared to ± 0.76 Å^3 in this work.

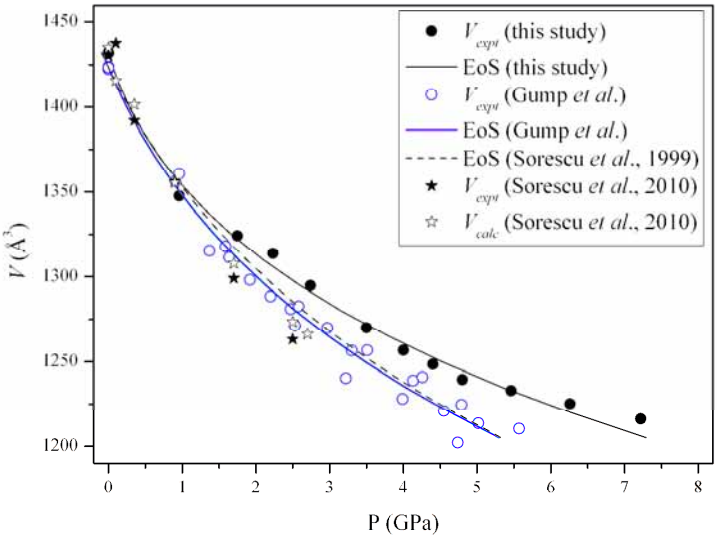

Figure 4.7 Plot of the compression of ε-CL-20: (a) this study, in which ε-CL-20 was compressed in MeOH:EtOH, (b) Gump *et al.* [31], using silicone fluid as pressure-transmitting medium, (c) theoretical equation of state determined by Sorescu *et al.* (1999) [50], and (d) *PV* data published by Sorescu *et al.* (2010), including experimental data from Pinkerton.[28]

The results of these studies and, more importantly, the discrepancies between this work and previous diffraction experiments conducted by Gump *et al.*[30, 31] highlight the importance of maintaining hydrostaticity throughout compression. Thus the selection of pressure-

transmitting medium is critical to the outcome of the experiment. While the pressure medium used in this work (4:1 mixture of MeOH:EtOH) has been shown to remain hydrostatic to 9.8 GPa (*i.e*. above the limit of this compression experiment), Gump *et al*. employed Dow Corning 200 Fluid (silicone oil) that has a hydrostatic limit of *ca* 1.0 GPa.[51] It is therefore suggested that the equation of state calculated for ε-CL-20 in the present study should be considered more reliable, since the possibility of deviatoric stresses arising from non-hydrostatic conditions can be discounted.

4.5.2 Compression of γ-CL-20

Compression in Fluorinert FC-77

The compression of the γ-form was initially investigated by X-ray powder diffraction. Polycrystalline γ-CL-20 was loaded into a diamond-anvil cell (DAC) with Fluorinert (FC-77) as the pressure transmitting-medium. Diffraction data were collected to a maximum pressure of 1.52 GPa at the Extreme Conditions Beamline (I15), Diamond Light Source. An example of the high quality of the data is presented in Figure 4.8. The γ-form was observed to persist on compression to 0.72 GPa, but at the next pressure point, 1.44 GPa, a significant change was observed in the powder diffraction pattern, indicative of a phase transition to the high-pressure ζ-form. This is shown in Figure 4.9.

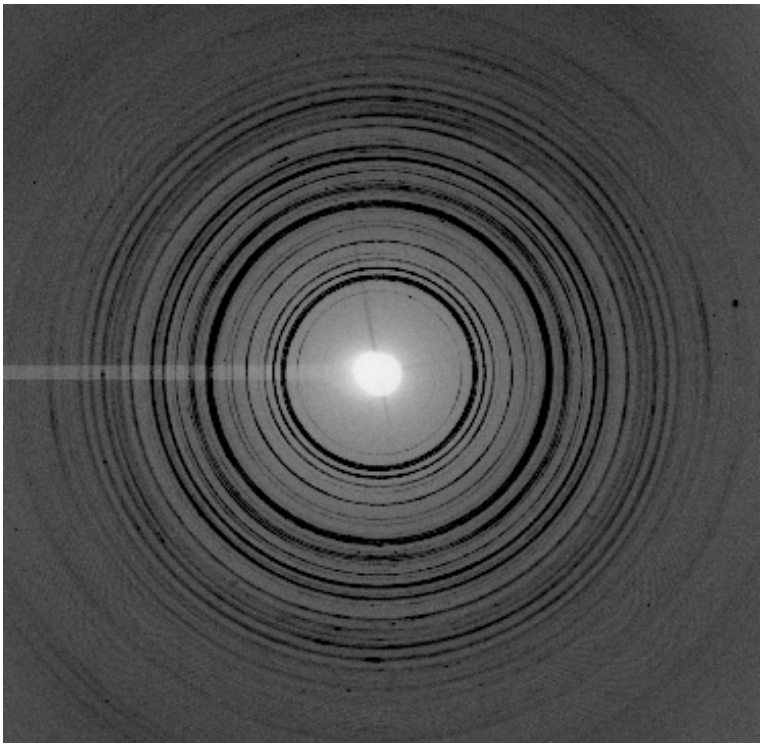

Figure 4.8 Raw powder diffraction data collected for ζ-CL-20 (1.44 GPa) at I15, DLS.

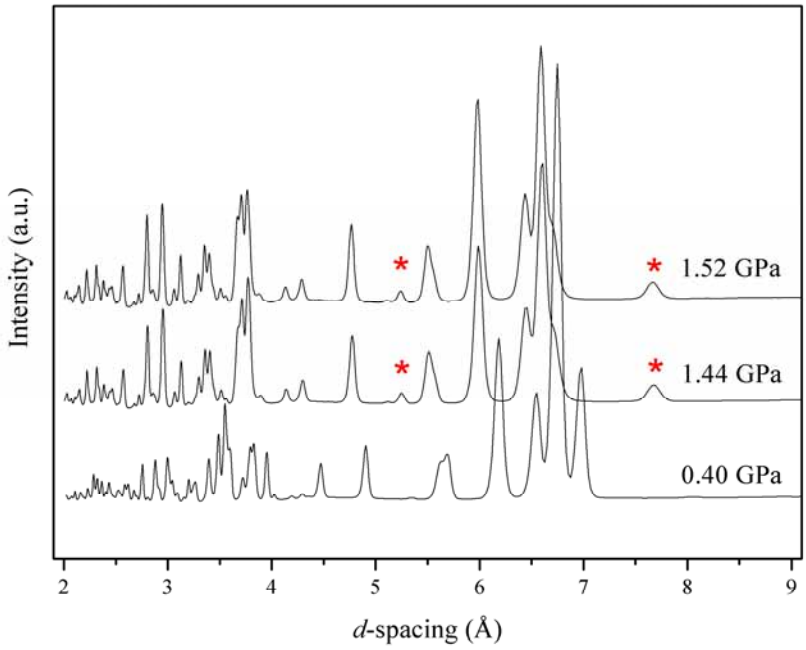

Figure 4.9 Comparison of the integrated X-ray powder diffraction patterns collected for γ-CL-20 (0.40 GPa) and ζ-CL-20 (1.44 and 1.52 GPa). The red asterisks show the diagnostic peaks of the ζ-form.

Despite the high quality data, attempts to index these patterns gave several possible solutions, none of which allowed structure solution. However, an important observation was that the difference between the X-ray powder diffraction patterns collected for γ- and ζ-CL-20 was subtle. Combined with previous optical observations [12], this suggested that hydrostatic compression of a single crystal through the γ → ζ transition might retain the integrity of the crystal, i.e. the phase transition is not reconstructive.

Crystals of the γ-form were grown from hot benzene and were loaded into a DAC, again using FC-77 as pressure medium (see Figure 4.10). The crystal was initially compressed to ~0.05 GPa to check crystal quality and the diffraction data were of sufficient quality to allow a full structural refinement of the γ-form. On compression to ~1.20 GPa, it was possible to index a set of reflections to a monoclinic cell [$P2_1/n$, a = 12.8244(8), b = 7.9029(8), c = 14.3622(6) Å and β = 111.205(4)°]. A second data-set was collected at 3.30(5) GPa with longer exposure times in order to improve data quality. It is common in high-pressure crystallography that data-sets suffer from low completeness due to shading from the steel body of the diamond-anvil cell. The completeness of both these datasets was ~60% and this, coupled with the complexity of the molecular structure, meant that structure solution *via* direct methods was not possible. Instead the indexing solutions obtained from the single-

crystal studies were used as a starting point for the structure solution from the powder diffraction patterns using the program FOX that employs direct space global optimisation methods.[36] This structural model was then refined (with no restraints) against each of the single-crystal datasets to give the molecular conformation shown in Figure 4.11.

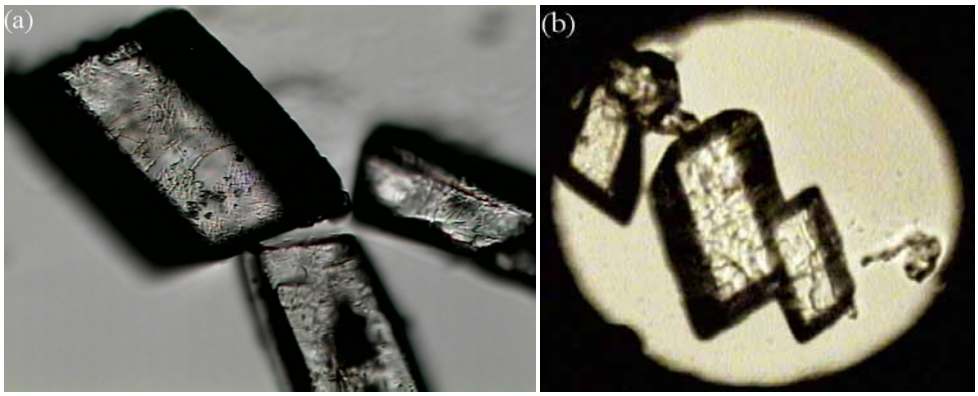

Figure 4.10 Single crystals of γ-CL-20: (a) at ambient conditions, and (b) loaded in DAC.

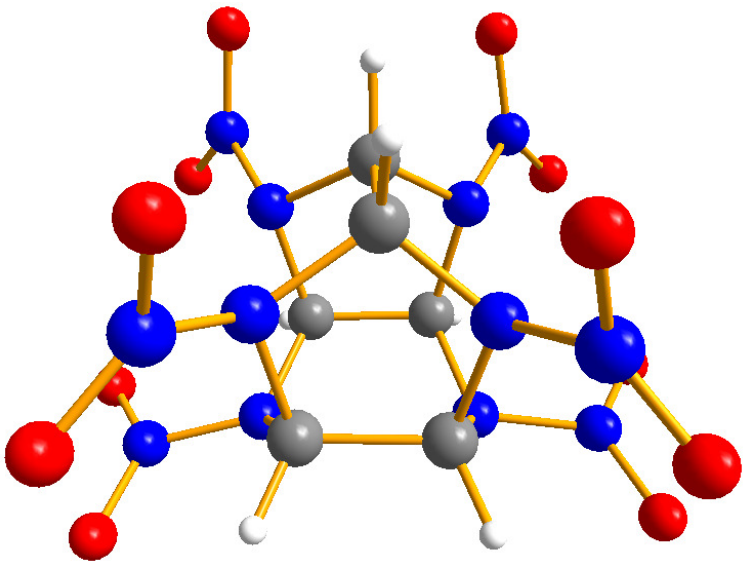

Figure 4.11 Molecular conformation of ζ-CL-20 obtained at 3.30(5) GPa.

Further confirmation that the crystal structure was correct was obtained by performing full-profile Rietveld refinements on all of the collected powder diffraction patterns, including those kindly provided by Gump and Peiris.[52] During the refinements restraints were applied to the geometry of the nitro groups, whilst the positions of the cage atoms were constrained to those obtained from the single-crystal refinements. Figure 4.12 shows an example of the quality of the Rietveld refinements for the patterns collected on the ζ-form.

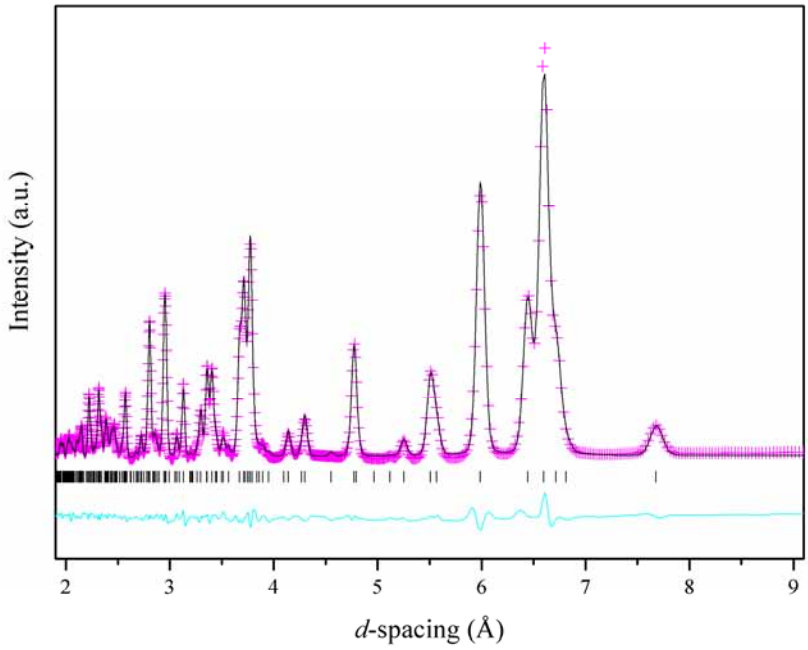

Figure 4.12 Fit of the Rietveld refinement of the ζ-CL-20 model (black tick marks) to the X-ray powder diffraction pattern recorded at 1.44(5) GPa. The experimental data (I_{obs}) are represented in pink, while the calculated pattern (I_{calc}) is shown as a black line. The difference curve ($I_{obs} - I_{calc}$) is shown in cyan.

In order to facilitate the comparison of the high-pressure ζ-form with the starting γ-form, the molecular conformations (determined from single-crystal diffraction) are presented together in Figure 4.13. This highlights that while the isowurtzitane cage does not change, the *exo*- and *endo*- spatial arrangement of the nitro groups with respect to the cage is different in the two forms. The ζ-form clearly adopts the conformation in which all of the nitro groups are *exo* with respect to the five- and six-membered rings, which is consistent with conclusions made on the basis of fewer bands being observed in the IR spectra.[12] Furthermore, this is the molecular conformation suggested by DFT calculations.[15] Given the relatively small energy differences between the most stable molecular conformation (0.0 – 9.63 kJ mol^{-1}), it is perhaps not surprising that compression of the γ-form will induce a phase transition to a conformation that allows more efficient crystal packing, as is exemplified in this case by a contraction of volume across the γ → ζ transition.

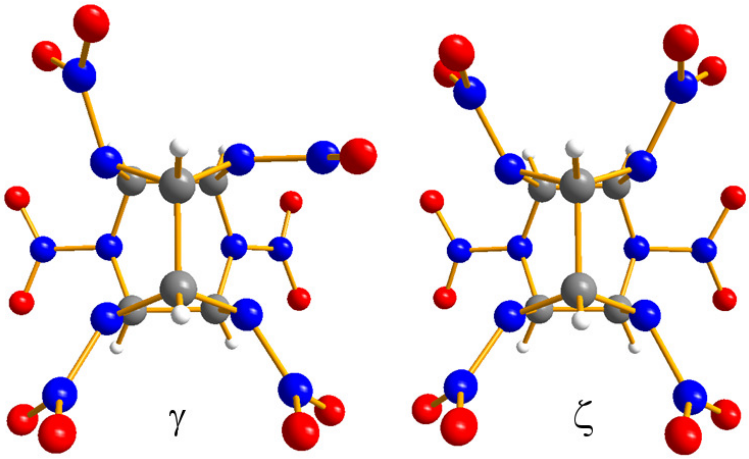

Figure 4.13 Molecular conformations of ζ- and γ-CL-20, showing that while the isowurtzitane cage does not change, the relative orientation of the nitro groups is different between the two polymorphs.

The packing in ζ-CL-20 retains the 'face-to-face' arrangement observed in the γ-form (where all five-membered rings of the cage are oriented about the same axis, see Figure 4.14). However, the closer packing and more symmetrical molecular conformation of the ζ-form allows a network of weak C-H…O interactions whereas these interactions form a chain in the γ-form. This network arrangement is more like that observed in ε-CL-20, which displays 'edge-to-face' packing. In this way, the ζ-form may be considered to display structural similarities with both γ- and ε-CL-20.

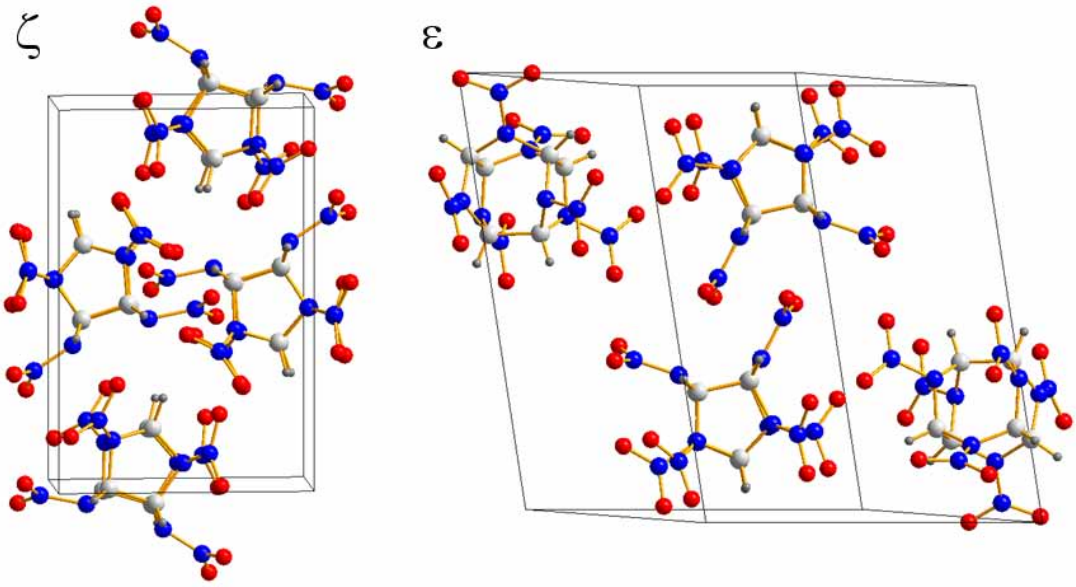

Figure 4.14 (a) The 'face-to-face' packing observed in ζ-CL-20; (b) the 'edge-to-face' packing of the ε-form. In both cases the unit cells are oriented such that the five-membered rings are viewed from above. Both polymorphs exhibit networks of intermolecular C-H…O interactions, in which each molecule interacts with two neighbouring molecules.

The structure solution of the high-pressure ζ-CL-20 is a significant achievement, given the complexity of the molecular conformation. These studies were limited, however, to relatively low pressures, due to the low hydrostatic limit of the pressure-transmitting medium in this study (Fluorinert is not considered to be hydrostatic at pressures greater than 1.2 GPa [53]). It was therefore thought prudent to carry out this compression in another medium in order to investigate the compression of γ-CL-20 to ~ 5 GPa. This would provide valuable information such as the density of ζ-CL-20 to compare to the ε-form at similar pressures as well as an equation of state for the high-pressure ζ-form.

Compression in Methanol:Ethanol

In order to provide complementary structural data, a neutron powder diffraction study was conducted at the PEARL-HiPr beamline (ISIS) using a Paris-Edinburgh Cell. In this case, the maximum pressure studied was 5.16 GPa, representing a significant extension of the pressure range over which this form has been studied previously. However, in order to maintain hydrostaticity in this pressure regime it was necessary to use a perdeuterated mixture (4:1) of methanol and ethanol as the pressure-transmitting medium.

A multiplot of the neutron powder diffraction patterns collected during this study is presented in Figure 4.15. It should be noted that the significant complexity of the synthetic procedure meant that it was not possible to obtain perdeuterated samples of γ-CL-20 for this study. As a result, the neutron powder diffraction patterns collected in this study exhibit a higher background than would normally be desired, due to the incoherent scattering from the hydrogen atoms (20 mol %) within the CL-20-h_6 sample. Despite this, there is clear evidence of a phase transition occurring between the first two patterns, collected at 0.10 and 0.57 GPa, respectively. For example, peaks at 2.3 and 3.8 Å in the pattern collected for the γ-form disappear from the pattern at 0.57 GPa. Furthermore, the peaks with strong intensities at 3.1 and 3.2 Å in the higher pressure pattern are simply not evident in the original pattern. Upon compression to 5.16 GPa, no further changes in the diffraction patterns indicative of a phase transition were observed. Unfortunately mechanical failure of the gasket resulted in sample detonation, causing damage to the WC anvils (see Figure 4.16) and thus curtailing the experiment. It was therefore not possible to investigate the decompression behaviour in this instance.

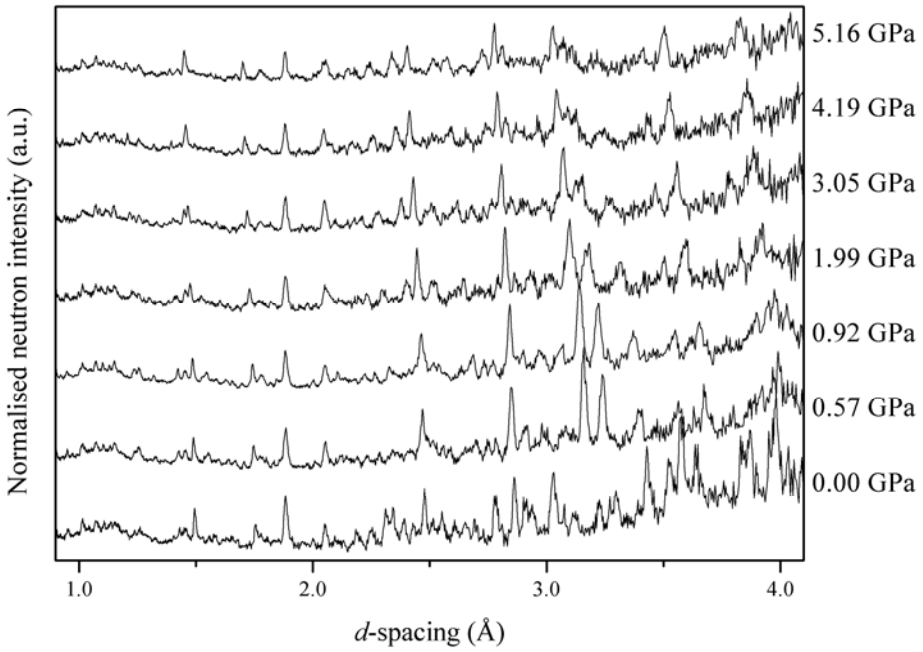

Figure 4.15 Multiplot of the neutron powder diffraction patterns collected during compression of γ-CL-20 in MeOD/EtOD.

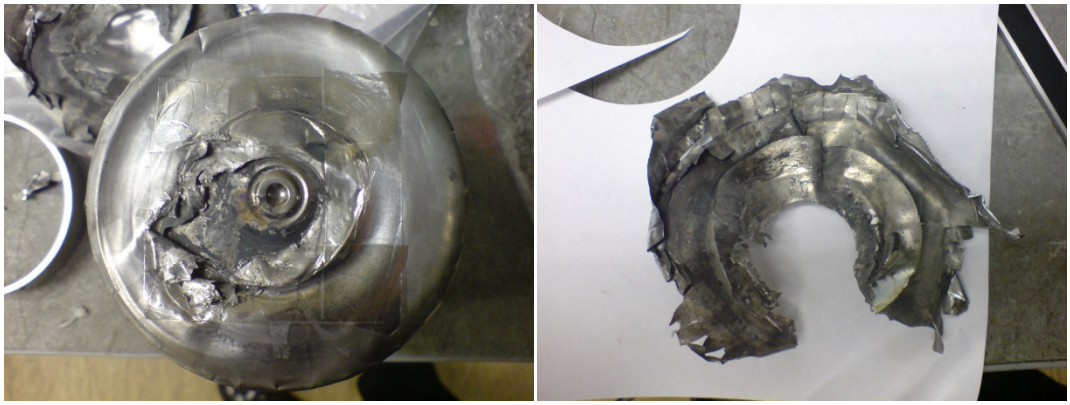

Figure 4.16 Photographs of the damage to the WC anvils due to the mechanical failure of the gasket and subsequent detonation of the sample. It should be noted that the PE-cell is contained in a metal vacuum tank and the whole experiment is conducted in an interlocked hutch. The experiment was rigorously assessed to ensure compliance with Health and Safety requirements; no members of the experimental team were in danger during the course of this experiment.

After confirming sample purity by Rietveld refinement of the initial pattern, refinement of the higher-pressure patterns was undertaken, with rather surprising results. Using the structural model of the ζ-form determined from the X-ray diffraction experiments described above, it was not possible to attain convergence. The quality of the Rietveld fit to the pattern collected at 3.05 GPa is shown in Figure 4.17. The marked differences between the observed

and calculated patterns are clear indications that the structural model used in this refinement is incorrect. In other words, the structure adopted upon compression of γ-CL-20 in MeOD/EtOD is *not* the same as that adopted when compression is performed in Fluorinert. This is a significant observation since it implies that the structural response of this material under compression is dependent upon the pressure-transmitting medium used. This, in addition to the importance of hydrostaticity discussed previously, underscores the complexity of high-pressure studies and the necessity for the publication of accurate experimental details.

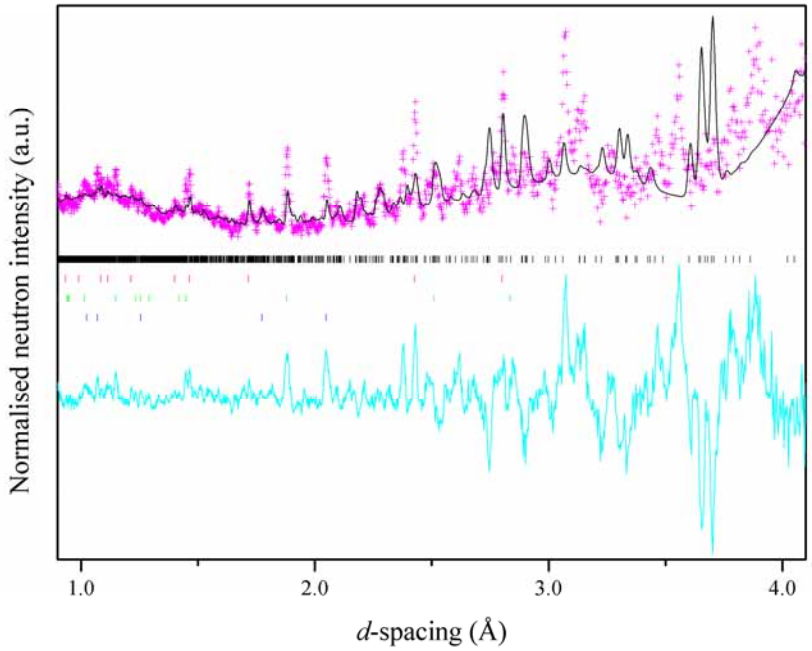

Figure 4.17 Rietveld refinement of the neutron powder diffraction pattern collected at 3.05 GPa using ζ-CL-20 structural model (black tick marks), along with the Pb pressure marker (red tick marks) and the diffracted intensities from the WC anvils and Ni binder (green and blue, respectively). Numerous mismatches are evident in this refinement and it is clear that the ζ-form is not adopted under these conditions.

This observation stimulated further investigations into the compression of γ-CL-20 in methanol:ethanol using single-crystal X-ray diffraction in order to provide a direct comparison with the analogous experiments using Fluorinert. It was decided that, in order to maximise data completeness in this experiment, two small crystals would be loaded into the diamond-anvil cell (DAC) in different orientations (as described in Section 2.2.3). In this way, two single crystals of the γ-form (produced by re-crystallisation of ε-CL-20 from hot benzene, as above) were loaded into a DAC, along with a small ruby chip to act as pressure

calibrant. Subsequent addition of the pressure-transmitting medium (4:1 MeOH:EtOH), however, resulted in the immediate formation of bubbles on the surface of the crystals. After a period of *ca* 20 mins the interaction between crystal and medium had progressed to such an extent that crystallinity was completely destroyed. This dramatic effect is shown in Figure 4.18.

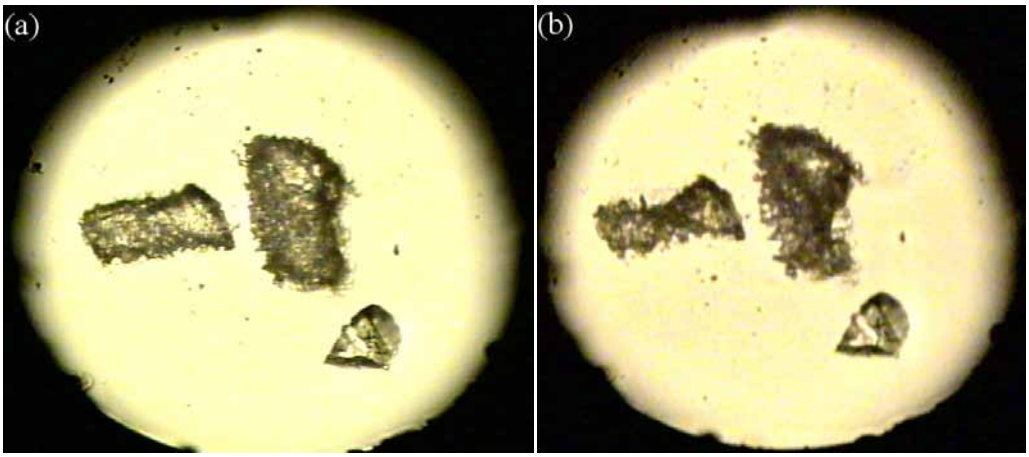

Figure 4.18 Photographs of single crystals loaded into a DAC with MeOH:EtOH as pressure-transmitting medium: (a) immediately after closure of the cell; and (b) after 20 mins, highlighting the complete destruction of the crystals. The ruby chip can be found in the bottom right quadrant of the sample chamber in both photographs.

In order to retain sufficient crystallinity to allow single-crystal diffraction, it was necessary to load a larger crystal (*ca* 150 x 75 x 50 μm) into the DAC. Thus, despite surface effects attributable to the interaction of the sample crystal with the medium, it was possible to obtain a data-set at 0.05 GPa of sufficient quality to allow a satisfactory structural refinement of γ-CL-20 ($P2_1/n$). Compression of this crystal to 0.5 GPa resulted in a distinct change in crystal morphology (see Figure 4.19), in accordance with the transition pressure determined in the neutron powder diffraction study. At this pressure, it was possible to index a set of reflections to an orthorhombic unit cell (*Pbca*, a = 9.6472, b = 13.1663, c = 23.3562 Å) and the quality of the data was such that structure solution was possible *via* direct methods.[46]

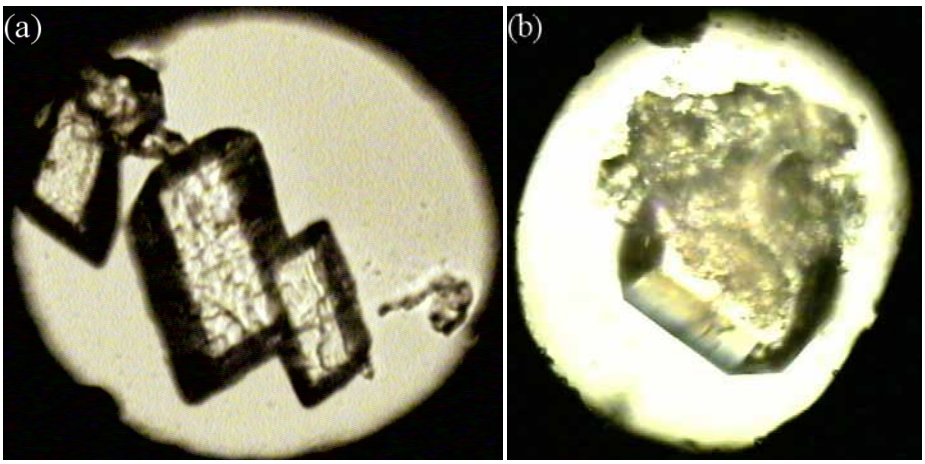

Figure 4.19 Comparison of the crystal morphology of the γ-form at ambient conditions and after compression to 0.5 GPa in MeOH:EtOH.

It is interesting to note that the unit cell dimensions, the crystal packing and the conformation of the CL-20 molecule in this form (shown in Figure 4.20) correspond extremely well those observed for α-CL-20, the hydrated form under ambient conditions. Crucially, however, the relatively low completeness (80%) of the high-pressure data-set meant that it was not possible to model the residual electron-density sufficiently to determine whether this was indeed the same form, that is a hydrate, or in fact a solvate of ethanol and/or methanol. This was further complicated by the suspected disorder of the solvent molecules within the crystal lattice. It was therefore hoped that this form was sufficiently metastable to allow its recovery to ambient pressure and its extraction from the DAC. Thus high-quality, low-temperature X-ray single-crystal diffraction data may be obtained.

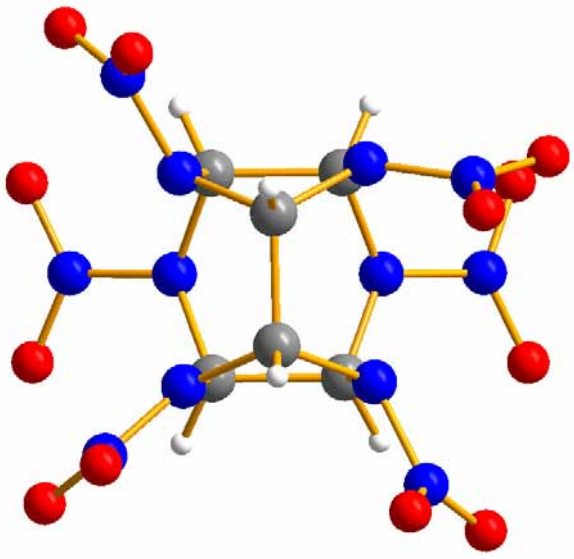

Figure 4.20 Comparison of the molecular conformation after compression of γ-CL-20 to 0.5 GPa in MeOH:EtOH.

Decompression of the sample to ambient pressure did not result in any visual indications of deterioration in crystal quality. Hence it was possible to obtain an orthorhombic unit cell indexing (*Pbca*) from a data collection performed (at 293 K) while the crystal was still confined to the DAC. Indeed the crystal was sufficiently stable to be manipulated and mounted on a fibre for data-collection at 100 K. The conformation of the CL-20 molecule and the crystal packing at this temperature were both consistent with the structure refinement at 0.5 GPa, confirming that neither decompression nor cooling had resulted in a phase transition.

Furthermore, the quality of the data was such that it has been possible to describe more accurately the solvent disorder within the structure. In contrast to the α-form, with which this structure shares a common molecular conformation and packing motif, the crystallised solvent is not water, but rather methanol. Moreover, the CL-20:MeOH ratio has been determined to be 1:0.5. The α-CL-20 structure reported by Golovina *et al.* [14] has been determined to contain a CL-20 to H_2O ratio of 1:0.57; meanwhile, in the studies by Nielsen *et al.* and Jacob *et al.* this was found to be 1:0.25.[2, 13] It should also be noted that the methanol molecules may adopt one of two orientations with respect to the rest of the unit cell, with approximately equal probability. Thus it has been necessary to model this disorder by the inclusion of two carbon atoms (with occupancy of 0.5) located at 180° to one another about the central oxygen atom, which resides on an inversion centre.

Despite these differences, however, the methanol molecules are broadly located in similar positions to those occupied by water molecules in the α-structures. Primarily, the solvent molecules are organised into channels running parallel to the *a*-axis at (*x*, *y*, 0) and (*x*, *y*, 0.5), as shown in Figure 4.21, with two whole molecules per unit cell in each channel. The positions of the solvent molecules in the crystal lattice coincide with voids within a lattice constructed solely from α-CL-20 molecules, as shown in Figure 4.21(c).

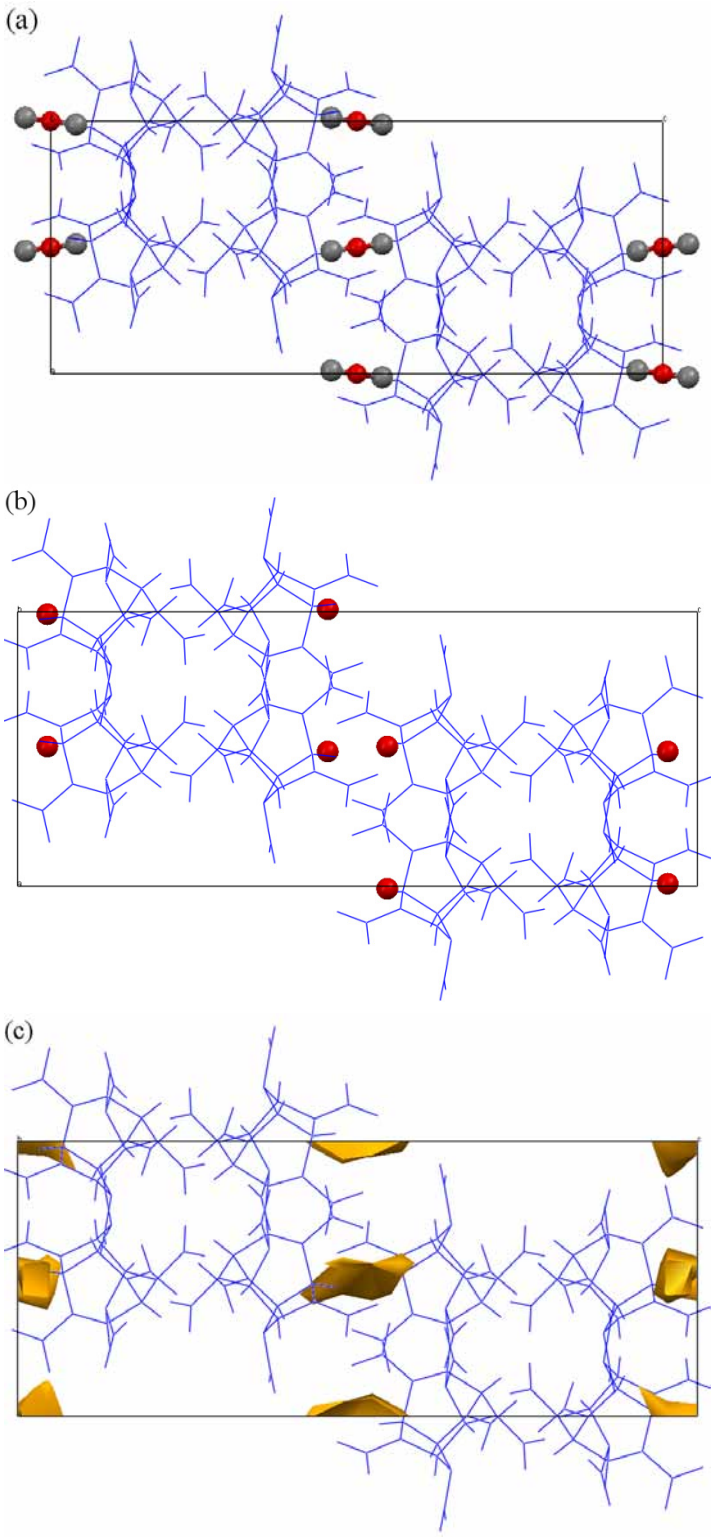

Figure 4.21 Comparison of the crystal structure of (a) the CL-20:MeOH solvate determined in this work with, (b) the α-CL-20 structure published by Jacob *et al.* In addition, void analysis of the dehydrated α-lattice has been conducted by manually deleting the water molecules from the structure reported by Jacob *et al.* and using a probe radius of 0.75 Å. These voids are shown in yellow in (c).

The inclusion of methanol molecules into this α-framework also has significant implications for the crystal density. It is interesting to note that, of the previously published structures of α-CL-20, the greatest crystal density (1.98 Mg m^{-3} at 295 K) is displayed by the structure reported by Nielsen *et al*. with a CL-20:H_2O ratio of 1:0.25, indicating perhaps that the swelling of the crystal lattice to incorporate more solvent molecules is not compensated by the added mass per unit cell. Golovina *et al.* and Jacob *et al.* both report a room temperature crystal density of 1.97 Mg m^{-3} for their 1:0.57 and 1:0.25 hydrates, respectively. In the current study, the crystal density has been determined to be 2.001 Mg m^{-3} at 100 K (as determined from full structure refinement) and 1.93 Mg m^{-3} at 293 K (based on unit cell indexing obtained from the diamond-anvil cell data-collection). Although it would be desirable to conduct an ambient-temperature data collection on a crystal mounted on a fibre, this clearly suggests that the methanol solvate is less dense than the hydrates. However, the room temperature density exceeds that of the γ-form (1.916 Mg m^{-3} at 293 K).[2] This has significant implications for its application as an energetic material, however, since a material's detonation is, to a first approximation, proportional to its crystal density.[54] This would perhaps indicate that CL-20 with solvent inclusions would be less powerful, although other factors, such as sensitivity for example, contribute to an overall assessment of energetic performance.

A summary of the pertinent crystallographic information from the data collections performed in this study is presented in Table 4.3, alongside information reported in the literature for α-CL-20.

	CL-20:MeOH		CL-20:H_2O		
Stoichiometry	2:1	2:1	1:0.57 [14]	1:0.25 [2]	1:0.25 [13]
Space Group	*Pbca*	*Pbca*	*Pbca*	*Pbca*	*Pbca*
a (Å)	9.773(2)	9.6445(5)	9.603(3)	9.485(2)	9.546(1)
b (Å)	13.346(3)	13.2186(7)	13.304(3)	13.225(4)	13.232(1)
c (Å)	23.925(5)	23.3407(8)	23.653(1)	23.673(3)	23.634(2)
V (Å^3)	3120.6(10)	2975.6(2)	3021.9(2)	2969.5(11)	2985.3(10)
D_c (Mg m^{-3})	1.93	2.001	1.97	1.98	1.97
T (K)	293	100	295	295	295

Table 4.3 Crystallographic information for the 'α-like' structure determined in this study at 293 and 100 K, presented alongside the published information for α-CL-20.

Using the structure of the CL-20:methanol solvate determined in this study, it was then possible to perform full-profile Rietveld refinements of the neutron powder diffraction

patterns collected during the compression of γ-CL-20 in MeOD:EtOD. It should be noted, however, that some intensity mismatches can be observed throughout. For example, the quality of the Rietveld refinement conducted on the pattern obtained at 5.16 GPa is shown in Figure 4.22. Inspection of the reflections most affected by the apparent intensity mismatches (for example, the (026) peak at ca 3.2 Å), suggests there exists a subtlety to the solvent disorder that has not been modelled sufficiently. Unfortunately, the relatively poor resolution of the neutron powder patterns and the restricted access to reciprocal space due to the Paris-Edinburgh cell (such studies are limited to a *d*-spacing range of 1 – 4.2 Å), have meant that it has not been possible to qualitatively assess the location of the methanol molecules within the lattice. In addition, given the large number of atoms in the asymmetric unit (39), it was thought prudent not to refine the atomic co-ordinates as this would introduce far more variables than would be appropriate for data of this quality. Despite this, all of the refinements conducted in this study have been stable and the unit cell parameters determined at each pressure have been tabulated (Table 4.4) and plotted below (see Figure 4.23).

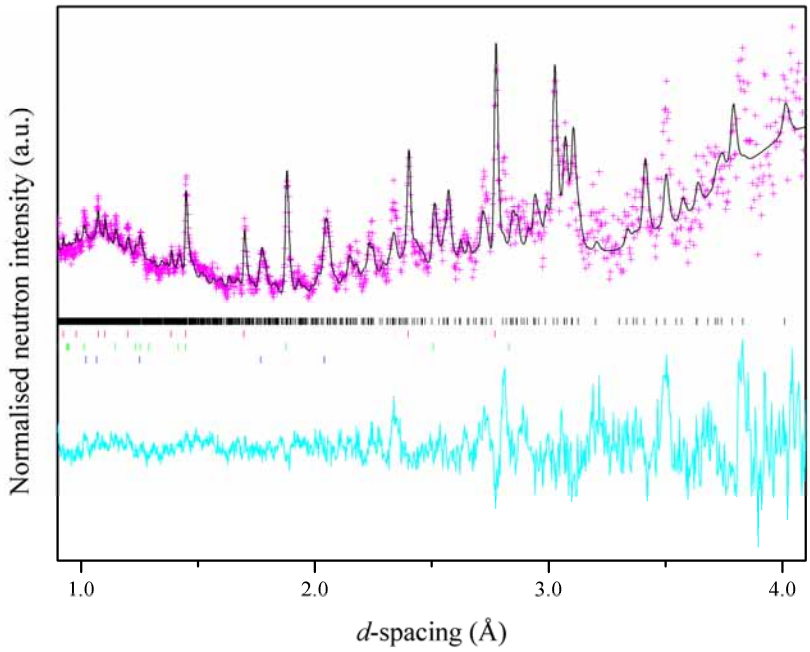

Figure 4.22 Plot of the Rietveld refinement of the pattern collected at 5.16 GPa using the structure determined for the CL-20:methanol solvate. The experimental data (I_{obs}) are represented as pink crosses, the calculated pattern (I_{calc}) is shown in black and the difference (I_{obs} - I_{calc}) in cyan. Tick-marks for each phase are also shown for clarity: CL-20:MeOD (black), Pb (red), WC (green) and Ni (blue).

P (GPa)	a (Å)	b (Å)	c (Å)	β (°)	V (Å^3)	wR_p
0.00	13.167(2)	8.1351(14)	14.839(2)	109.078(13)	1502.2(3)	0.026
0.57	9.594(3)	13.090(5)	23.267(7)		2922.0(11)	0.043
0.92	9.532(3)	13.001(5)	23.154(7)		2869.2(11)	0.040
1.99	9.395(4)	12.770(5)	22.898(7)		2747.3(12)	0.043
3.05	9.296(4)	12.610(5)	22.725(7)		2663.9(11)	0.042
4.19	9.205(4)	12.478(6)	22.557(8)		2590.8(13)	0.046
5.16	9.149(5)	12.387(6)	22.425(8)		2541.5(14)	0.052

Table 4.4 Variation of the unit cell parameters throughout compression of CL-20 in MeOD:EtOD to 5.16 GPa, indicating the transition from the pure γ-form to the CL-20:MeOD solvate.

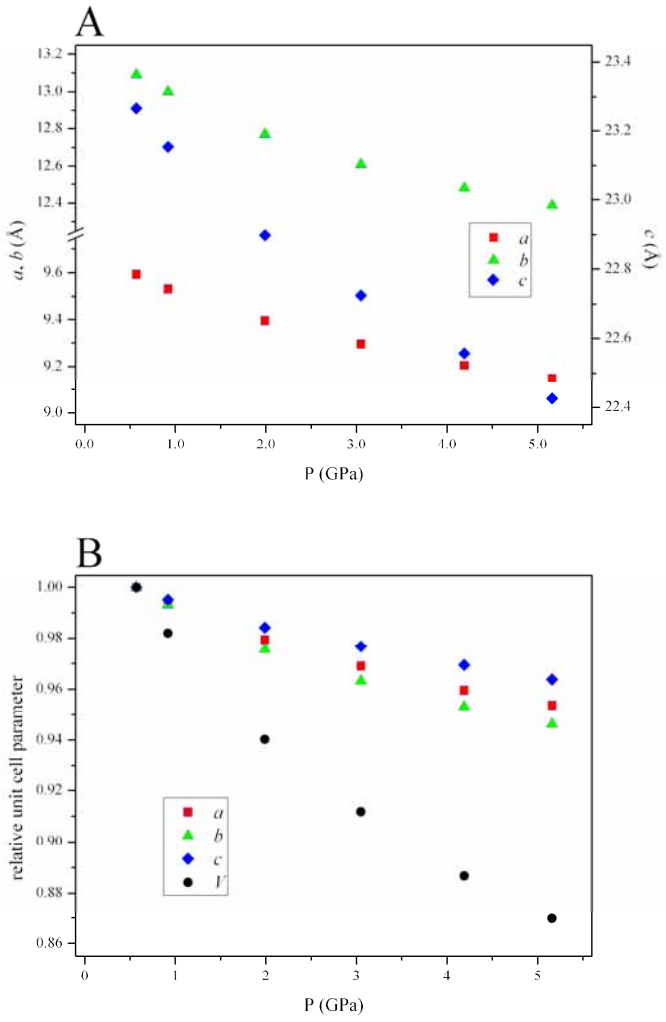

Figure 4.23 (a) The compression, and (b) the relative compression of the unit cell parameters of the CL-20:methanol solvate up to the maximum pressure (5.16 GPa).

The relative compression of the unit cell parameters shows that the *c*-axis, the direct normal to the alternating layers of methanol and CL-20 molecules, is least compressible, while the

b-axis is most compressible. Although the difference in the relative compression of these axes is small (*ca* 2% at 5.16 GPa), it perhaps underlines the important role of the methanol molecules in filling voids in the lattice. If these voids were not filled by solvent molecules, one may expect the *c*-axis to be, in fact, the most sensitive to high pressure since compression often manifests itself in the collapse of such voids and a shortening of inter-planar distances.

Furthermore, it is interesting to note that, as a whole, the CL-20:methanol structure displays similar compressibility to the pure ε-form. The smooth contraction of the unit cell volume (up to 5.16 GPa) has been fitted to both a 3rd-order Birch-Murnaghan and a Vinet EoS, as shown in Figure 4.24. In both cases, the unit cell volume at zero pressure has been fixed to the value determined by single-crystal X-ray diffraction at 293 K since CL-20-h_6 samples were used in both diffraction experiments. The coefficients of the Birch-Murnaghan EoS have been determined as V_0 = 3120.6 Å^3 (fixed), B_0 = 4.6(5) GPa and B' = 27(4). Visual inspection of this fit, however, clearly shows that this does not adequately describe the contraction of the unit cell volume, particularly at higher pressure. In this case, a much more satisfactory fit is obtained with a Vinet EoS with V_0 = 3120.6 Å^3 (fixed), B_0 = 6.6(5) GPa and B' = 13.6(8). If the Vinet equation of state is regarded as being more accurate, this suggests that the methanol solvate is marginally more compressible than the pure ε-form. In the current study, the bulk modulus of ε-CL-20 has been determined to be 9.5(22) GPa.

It should be noted, however, that calculation of the EoS based solely on the neutron powder diffraction data results in marked differences in the bulk modulus and its pressure-derivative, B'. Since no decompression study was carried out in this instance, no ambient pressure refinement has been possible. Instead, the EoS has been determined by fixing V_0 to be the unit cell volume at the first pressure where this form was observed, *i.e*. 2922.0 Å^3 at 0.57 GPa. Then, in line with the procedure outlined in Section 2.6, all succeeding pressures have been normalised to this pressure. The 3rd-order Birch-Murnaghan and Vinet equations of state determined in such a way are displayed in Figure 4.24(b). The coefficients have been found to be B_0 = 17.2(10) GPa and B' = 10.1(12) for the 3rd-Order Birch Murnaghan EoS; and, B_0 = 17.5(8) GPa and B' = 9.2(8) for the Vinet EoS. In contrast to the values above, the bulk moduli calculated in this way indicate that this structure is significantly less compressible than the ε-form. It is therefore of immediate interest to conduct a rigorous compression (and decompression) study of this form, preferably by high-resolution X-ray powder diffraction, in order to obtain a high-quality EoS for this material.

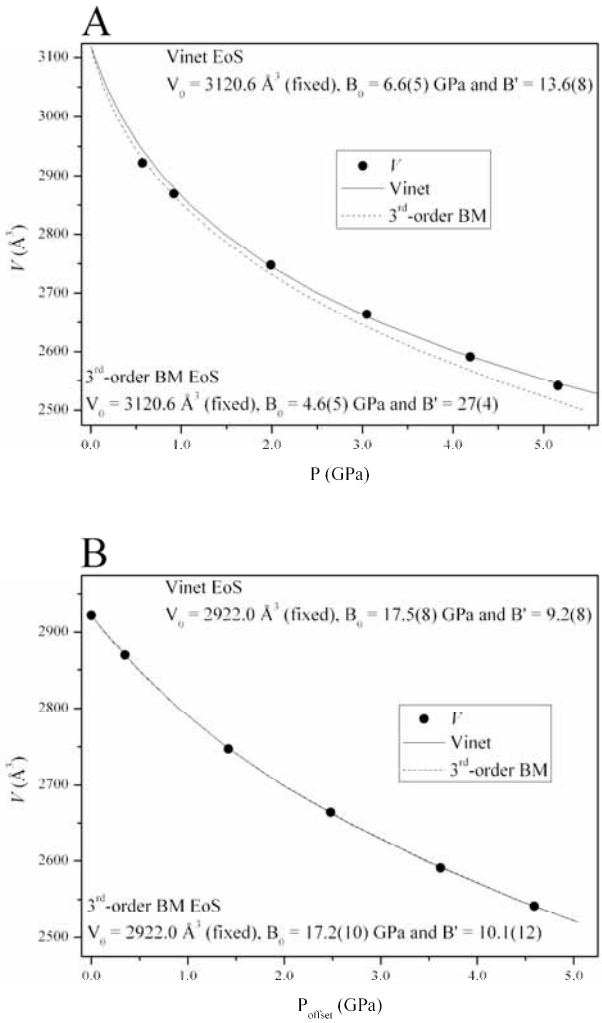

Figure 4.24 (a) Variation of unit cell volume of CL20:MeOH with pressure, including V_0 determined by X-ray single-crystal diffraction and a representation of the Vinet and 3rd-order Birch-Murnaghan equations of state; (b) the compression of the unit cell volume determined during the neutron powder diffraction experiment. In this case, pressures have been normalised to 0.57 GPa.

In addition to a re-examination of the compression behaviour of this methanol solvate, it would be highly desirable to conduct further analysis on the recovered material to determine quantitatively the degree of solvation, as well as the positions of the solvent molecules within the lattice. Current studies are therefore focussed on the spectroscopic (IR/Raman and NMR) and gravimetric (CHNO analysis and mass spectrometry) analysis, in addition to obtaining the desired high-quality diffraction data.

These studies should then be extended to explore the possibility of obtaining solvates and co-crystals of CL-20 at ambient conditions. For example, it may be possible to obtain a CL-20:methanol solvate at ambient pressure, which displays a different stoichiometry or a different molecular conformation for example. This would perhaps have significant

implications for crystal density and sensitivity. Moreover, in studies analogous to the recrystallisation of pharmaceuticals at pressure, the formation of co-crystals at elevated pressures should also be explored. Finally, an analysis of the thermal stability of such co-crystals must be undertaken. For example, crystal quality may be adversely affected by gradual desolvation during storage and, as a result, the material may actually become more sensitive. Furthermore, the desolvation products should be characterised as fully as possible in order to ascertain the resultant polymorph.

4.6 Conclusions

The structural data presented herein are illustrative of a significant advance in the structural characterisation of this important class of materials under extreme conditions. The level of complexity of the CL-20 molecule extends the limits to which high-pressure techniques may be applied, and highlights the need for employing a range of different methods for structure solution. These results will be of importance not only to the energetics community, for whom the high-pressure polymorphism of CL-20 has been a long-standing problem, but also to those solid-state chemists and physicists wishing to model the behaviour of this important class of nitramines.

The structure of the high-pressure ζ-form has been determined by a combination of single-crystal and powder X-ray diffraction. Compression of γ-CL-20 to $P > 0.72$ GPa in Fluorinert has been observed to result in a conformational change of the nitro groups with respect to the five- and six-membered rings. This change in molecular conformation imbues the high-pressure ζ-form with a higher degree of molecular symmetry and results in a crystal structure with similarities to both the γ- and ε-forms.

In a dramatic example of the effect the pressure-transmitting medium may have on the structural properties of a system, compression of γ-CL-20 in MeOH:EtOH has been found to result in the formation of a CL-20:MeOH (2:1) solvate, simply by the application of pressure. Furthermore, once formed (above 0.5 GPa), this solvate remains stable upon compression to at least 5.2 GPa *and* can be recovered to ambient pressure at ambient temperature. Although the methanol solvate has been found to be less dense than the ε-form, this result clearly highlights the opportunity that co-crystallisation techniques (at ambient conditions as well as at elevated pressure) present in the structure/property modification of these important materials.

Finally, the importance of the starting polymorph has also been illustrated by conducting a high-pressure X-ray powder diffraction investigation of the compression of ε-CL-20 to a

maximum pressure of 7.22 GPa. At no point was a pressure-induced phase transition to the γ-form observed, contrary to previous spectroscopic studies.[32] Furthermore, the equation of state describing the hydrostatic compression of ε-CL-20 has been determined. The significance of this result should not be overlooked, since previous EoS data have been determined under non-hydrostatic conditions.[31] It may be suggested therefore that the current study represents a more useful experimental account of the effects of pressure on the crystal structure and hence provides a more rigorous test of computational predictions.

4.7 Suggestions for Further Work

While the hydrostatic compression of the thermodynamically most stable form under ambient conditions, ε-CL-20, has been rigorously investigated to 7.22 GPa, no high-quality equations of state exist for the other forms of CL-20. High-pressure studies of the α- and β-forms are therefore imperative. As was evident in the compression study of the other metastable form, γ-CL-20, this may result in further phase transitions to novel polymorphs. It would also be extremely valuable to extend the pressure range for which the ζ-form has been structurally characterised. However, this will naturally be complicated by the hydrostatic limit of the Fluorinert pressure-transmitting medium (*ca* 1.0 GPa).

As has been illustrated by the compression of γ-CL-20 in MeOH:EtOH, the effect of the pressure-transmitting medium should not be underestimated. It is therefore suggested that compressions be conducted in a range of pressure media to ensure any structural effects of non-hydrostaticity and sample/medium interactions have been accounted for. It should also be noted that decompression often yields important information, particularly on the relative stability of high-pressure forms and kinetic barriers to their re-transformation. It is essential therefore that detailed decompression studies are undertaken and the recoverability of high-pressure polymorphs to ambient pressure is explored.

In this study, the application of pressure alone has been sufficient to produce the ζ-form and a CL-20:MeOH solvate. As has been shown to be extremely successful in the structural characterisation of ε-RDX (Section 3.5.2), the combined effects of temperature *and* pressure on CL-20 should also be explored. Given the rich polymorphism under ambient conditions, one would expect such studies to produce further polymorphs of CL-20, some of which may be recoverable to ambient pressure. Moreover, any recovered high-pressure forms would be expected to be denser, and therefore more powerful, than the starting polymorph.

The formation of a CL-20:MeOH solvate at 0.5 GPa also presents a significant opportunity for the development of these materials by co-crystallisation. The ability of CL-20 to form a

methanol solvate and hydrates of different stoichiometries clearly suggests that voids large enough to accommodate small molecules exist within the structure. This feature should therefore be exploited fully by the investigation of CL-20 co-crystals under ambient conditions, as well as at elevated pressure. For example, it would be interesting to compare the structures of the methanol solvate produced in this work with one that may be crystallised at atmospheric pressure. Given the dramatically different thermodynamic conditions under which they have been formed, one may reasonably expect differences to arise between the structures, for example in solvent location or stoichiometry.

Moreover, the inclusion of small molecules in the crystal lattice would certainly result in changes in the crystal density and, crucially, sensitivity. Co-crystallisation may therefore be viewed as an opportunity to tailor munitions at the molecular level, provided their structures, stability and energetic performance have been thoroughly investigated.

4.8 References

1. A.T. Nielsen, *Synthesis of Caged Nitramine Explosives* in *Joint Army, Navy, NASA, Air Force (JANNAF) Propulsion Meeting*, 1987, San Diego, USA.
2. A.T. Nielsen, A.P. Chafin, S.L. Christian, D.W. Moore, M.P. Nadler, R.A. Nissan, D.J. Vanderah, R.D. Gilardi, C.F. George, and J.L. Flippen-Anderson, *Tetrahedron*, 1998, **54**, 11793.
3. R.S. Miller, in *Decomposition, Combustion and Detonation Chemistry of Energetic Materials*, 1995, Pittsburgh, USA.
4. R.L. Simpson, P.A. Urtiew, D.L. Ornellas, G.L. Moody, K.J. Scribner, and D.M. Hoffman, *Propellants, Explos., Pyrotech.*, 1997, **22**, 249.
5. H. Bazaki, S. Kawabe, H. Miya, and T. Kodama, *Propellants, Explos., Pyrotech.*, 1998, **23**, 333.
6. M.F. Foltz, C.L. Coon, F. Garcia, and A.L. Nichols III, *Propellants, Explos., Pyrotech.*, 1994, **19**, 19.
7. M.F. Foltz, C.L. Coon, F. Garcia, and A.L. Nichols III, *Propellants, Explos., Pyrotech.*, 1994, **19**, 133.
8. V.V. Nedelko, N.V. Chukanov, A.V. Raevskii, B.L. Korsounskii, T.S. Larikova, O.I. Kolesova, and F. Volk, *Propellants, Explos., Pyrotech.*, 2000, **25**, 255.
9. R.Y. Yee, M.P. Nadler, and A.T. Nielsen, in *JANNAF Propulsion Meeting*, 1990, Anaheim, USA.
10. K.J. Kraeutle, in *JANNAF Propulsion Meeting*, 1988, Huntsville, USA.
11. K.J. Kraeutle, in *JANNAF Proceedings*, 1990, Cheyenne, USA.
12. T.P. Russell, P.J. Miller, G.J. Piermarini, and S. Block, *J. Phys. Chem.*, 1992, **96**, 5509.
13. G. Jacob, L. Toupet, L. Ricard, and C. G, *Private Communication to the CSD*, 1999.
14. N. Golovina, A. Raevskii, N. Chukanov, B. Korsounskii, L. Atovyman, and S. Aldoshin, *Rossijskij Khimicheskij Zhurnal*, 2004, **48**, 41.
15. Y. Kholod, S. Okovytyy, G. Kuramshina, M. Qasim, L. Gorb, and J. Leszczynski, *J. Mol. Struct.*, 2007, **843**, 14.
16. P. Goede, N.V. Latypov, and H. Östmark, *Propellants, Explos., Pyrotech.*, 2004, **29**, 205.
17. J.H. Kim, Y.C. Park, Y.J. Yim, and J.S. Han, *J. Chem. Eng. Jpn.*, 1998, **31**, 478.

18. D.M. Hoffman, *Propellants, Explos., Pyrotech.*, 2003, **28**, 194.
19. M.H. Lee, J.H. Kim, Y.C. Park, J.H. Hwang, and W.S. Kim, *Ind. Eng. Chem. Soc*, 2007, **46**, 1500.
20. T.P. Russell, P.J. Miller, G.J. Piermarini, and S. Block, *J. Phys. Chem.*, 1993, **97**, 1993.
21. J. Li and T.B. Brill, *Propellants, Explos., Pyrotech.*, 2007, **32**, 326.
22. G. Zhou, J. Wang, W.D. He, N.B. Wong, A. Tian, and W.K. Li, *J. Mol. Struct. THEOCHEM*, 2002, **589-590**, 273.
23. X.J. Xu, W.H. Zhu, and H.M. Xiao, *J. Phys. Chem. B*, 2007, **111**, 2090.
24. N. Chukanov, V. Zakharov, B. Korsunskii, A. Raevskii, V. Nedelko, S. Vozchikova, T. Larikova, N. Golovina, and S. Aldoshin, *Russ. J. Phys. Chem. A*, 2009, **83**, 29.
25. N. Chukanov, V. Dubovitskii, V. Zakharov, N. Golovina, B. Korsunskii, S. Vozchikova, V. Nedelko, T. Larikova, A. Raevskii, and S. Aldoshin, *Russ. J. Phys. Chem. B*, 2009, **3**, 486.
26. D.I.A. Millar, H.E. Maynard-Casely, and C.R. Pulham, *unpublished results,* 2010.
27. T.P. Russell, P.J. Miller, G.J. Piermarini, and S. Block, *J. Phys. Chem.*, 1992, **96**, 5509.
28. D.C. Sorescu and B.M. Rice, *J. Phys. Chem. C*, 2010, **114**, 6734.
29. J.C. Gump and S.M. Peiris, *Proc. Int. Det. Symposium, USA*, 2006, 1045.
30. J.C. Gump, C.A. Stoltz, and S.M. Peiris, *AIP Conf. Proc.*, 2007, **955**, 127.
31. J.C. Gump and S.M. Peiris, *J. Appl. Phys.*, 2008, **104**, 083509.
32. J.A. Ciezak, T.A. Jenkins, and Z. Liu, *Propellants, Explos., Pyrotech.*, 2007, **32**, 2774.
33. L. Merrill and W.A. Bassett, *Rev. Sci. Instrum.*, 1974, **45**, 290.
34. G.J. Piermarini, S. Block, J.D. Barnett, and R.A. Forman, *J. Appl. Phys.*, 1975, **46**, 2774.
35. A.P. Hammersley, S.O. Svensson, M. Hanfland, A.N. Fitch, and D. Hausermann, *High Press. Res.*, 1996, **14**, 235
36. V. Favre-Nicolin and R. Cerny, *J. Appl. Crystallogr.*, 2002, **35**, 734.
37. R. Von Dreele and A.C. Larson, *General Structure Analysis System (GSAS)*, 1986.
38. W.G. Marshall and D.J. Francis, *J. Appl. Crystallogr.*, 2002, **35**, 122.
39. J.M. Besson, R.J. Nelmes, G. Hamel, J.S. Loveday, G. Weill, and S. Hull, *Physica B*, 1992, **180-181**, 907.
40. S.A. Moggach, D.R. Allan, S. Parsons, and J.E. Warren, *J. Appl. Crystallogr.*, 2008, **41**, 249.
41. A. Dawson, D.R. Allan, S. Parsons, and M. Ruf, *J. Appl. Crystallogr.*, 2004, **37**, 410.
42. Bruker-Nonius, *APEX-II*, Bruker-AXS, Madison, WI, USA, 2000.
43. Bruker-AXS, *SAINT*, Bruker-AXS, Madison, WI, USA, 2003.
44. S. Parsons, *SHADE, Program for Empirical Absorption Corrections to High Pressure Data*, The University of Edinburgh, UK, 2004.
45. G.M. Sheldrick, *SADABS*, University of Göttingen, Germany, 2004.
46. A. Altomare, G. Cascarano, C. Giacovazzo, A. Guagliardi, M.C. Burla, G. Polidori, and M. Camalli, *J. Appl. Crystallogr.*, 1994, **27**, 435.
47. P.W. Betteridge, J.R. Carruthers, R.I. Cooper, K. Prout, and D.J. Watkin, *J. Appl. Crystallogr.*, 2003, **36**, 1487.
48. J. Cosier and A.M. Glazer, *J. Appl. Crystallogr.*, 1986, **19**, 105.
49. Oxford Diffraction Ltd, *CrysalisPRO Software*, Abingdon, UK, 2010.
50. D.C. Sorescu, B.M. Rice, and D.L. Thompson, *J. Phys. Chem. B*, 1999, **103**, 6783.
51. R.J. Angel, M. Bujak, J. Zhao, G.D. Gatta, and S.D. Jacobsen, *J. Appl. Crystallogr.*, 2007, **40**, 26.
52. J.C. Gump and S.M. Peiris, *personal communication*, 2009.
53. T. Varga, A.P. Wilkinson, and R.J. Angel, *Rev. Sci. Instrum.*, 2003, **74**, 4564.

54. J. Akhavan, *The Chemistry of Explosives*, Royal Society of Chemistry, Cambridge, UK, 2004, 2nd edn.

Chapter 5

Structural Investigation of a Series of Inorganic Azides

Part 1: NaN_3, CsN_3 and TlN_3

5 Structural Investigation of a Series of Inorganic Azides (Part 1)

5.1 General Introduction to Inorganic Azides

5.1.1 Azides as Energetic Materials

Inorganic azides [general formula $M^{n+}(N_3)_n$] have been widely used as energetic materials on account of their rapid decomposition to produce large amounts of nitrogen gas according to Equation (1):

$$M^{n+}(N_3)_n\,(s) \rightarrow M\,(s) + {}^{3n}/_{2}\,N_2\,(g) \qquad (1)$$

Upon initiation by stimulus, such as heat or impact, the heavy metal azides such as $Pb(N_3)_2$ and AgN_3 transition to detonation very rapidly making them ideal for use as primary explosives, although the extremely high sensitivity of copper and gold azides makes these impractical for use in munitions. Lead(II) azide is, in fact, the most widely used primary explosive, despite well-documented concerns over its environmental and toxicological effects.[1] Replacement of $Pb(N_3)_2$ in primers and detonators has proved to be very challenging because alternatives must have comparable explosive performance (in terms of explosive power and instantaneous response to initiation), while remaining chemically and thermally stable and compliant with existing health and safety regulations.[2] Other azides, such as NaN_3, are more difficult to initiate and decompose rapidly producing large volumes of N_2 gas, but do not detonate. This is particularly attractive for use as gas generators: NaN_3 for example has been used in automotive air-bags.[3]

Recent developments in the use of these compounds have focussed on the production of large amounts of nitrogen from a polymeric 'high-energy density material', which would be expected to burn rapidly with the release of environmentally clean by-products (i.e. $N_2(g)$ only). Peiris and Russell used the novel approach of photolysing NaN_3 under high pressure (up to 5.0 GPa) using visible light, λ = 514 nm.[4] It was hypothesised that by performing the reaction at these pressures, the azide radicals produced during photolysis would bond with other azide species to form larger molecules with high nitrogen content. Spectroscopic analysis led the authors to conclude tentatively that the product was either N_7^- or Cl_2N_6 (where $Cl^{\bullet}$ radicals originated from the NaCl pressure-transmitting medium) although the product was not recoverable to ambient pressure.

Eremets *et al*. have also reported the formation of polynitrogen species formed from sodium azide although they noted that application of pressure alone was sufficient to create a new species.[5] On the basis of their Raman spectroscopic study, they report a new phase observed above 19 GPa. The increased interaction between the azide ions at these pressures suggested a phase composed of larger clusters of nitrogen atoms. Raman measurements in the pressure range 50 – 120 GPa indicated that at these pressures an amorphous 'non-molecular' nitrogen species is formed, on the basis of the disappearance of modes attributable to the azide unit. Laser heating (up to 3300 K) and the application of large shear deformations to the sample by rotation of the diamond anvils were both found to accelerate these transitions. Although these non-molecular species could be stabilised on decompression to below 1 GPa, it was not possible to recover and characterise them at atmospheric pressure.

5.1.2 Structural Considerations

In general, azides can be broadly classified into three categories depending on their structures: molecular, ionic and co-ordinative azides.[6] Molecular azides, in which one terminal N-atom of the N_3 group is covalently bound to another atom or group (such as H, Me or a transition metal [7]), play an important role in synthetic chemistry, but are not a focus of this study.

In ionic azides the discrete cations and N_3^- anions are separated by distances greater than the sum of their respective ionic radii. Furthermore the anions are always perfectly linear and symmetric (the N-N bond lengths are equal and do not deviate significantly from 1.17 Å [8]). The electron density distribution around the N_3^- ion in sodium azide correlates well with the theoretical resonance model:

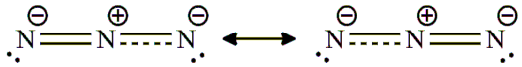

where the displaced double bond lines indicate bonding π-electrons, which lie out of the plane of the paper, perpendicular to the other bonding π-electrons,. This gives rise to a formal net positive charge on the central nitrogen of + 0.71 while the terminal N atoms each carry a charge of - 0.86.[9]

Co-ordinative azides may be considered to be an intermediate case between the ionic and molecular azides: the metal atoms are in close enough proximity to one (or more) azide group such that weak covalent interactions can occur between them, leading to polymeric networks in which the metal atoms are linked to one another *via* bridging azide units.[6] In

these cases (typically heavy metal azides) the linearity of the anion is generally retained, although some deviations have been observed (for example, in $Pb(N_3)_2$). The N-N bond lengths within the azide, however, are markedly dependent on the environments of each of the terminal N-atoms. If the terminal nitrogens are at similar distances away from two neighbouring metal atoms one would expect the N-N bond lengths to be similar, but if one N atom is only weakly interacting with one neighbouring metal, while the other N atom is surrounded by three metals, this will result in an asymmetry in the N-N bond lengths.

5.1.3 Structure and Sensitivity

Despite the rich polymorphism displayed by inorganic azides (*vide infra*), their chemical and structural simplicity makes them ideal for modelling deflagration/detonation reactions. Moreover, this family of compounds displays a wide range of sensitivities to detonation, ranging from the almost inert Group 1 azides to the very sensitive copper azides.[10] As a result, recent computational studies have focussed on understanding the electronic structure of these compounds, with a view to rationalising their explosive decompositions.[11-15] The most recent theoretical study of these important systems, however, has instead investigated the relationship between the sensitivity of a given azide and its crystal structure. Cartwright and Wilkinson report a linear correlation between impact sensitivity and the minimum non-bonded N…N distance across a wide variety of (ionic and co-ordinative) azides.[10] This is consistent with theoretical and experimental results [16], which indicate that a primary explosive should be capable of decomposition to products (in this case solid metal and $N_2(g)$) with a simple rearrangement of electrons and minimal atomic displacement.[10] While this model is appealing, primarily in its simplicity, the authors admit that no account has been made for the thermochemistry of the azides and most importantly the enthalpies of formation. Moreover their measure of sensitivity is limited to the sensitivity to impact and does not consider other initiation events such as heat, shock or friction, which may require a more nuanced description.

It is also pertinent to discussions of sensitivity to mention that temperature and/or pressure (such as in a detonation event) will undoubtedly affect the intermolecular distances and may lead to phase transitions. It is therefore absolutely critical to obtain structural information on these materials under extreme conditions in order to assess any theoretical models rigorously. Interestingly inorganic azides and diamond-anvil cell technology seem inextricably linked for this very reason. Compressibility studies on what were regarded as unstable materials were not seriously considered previously because of the danger of explosion in relatively crude large volume presses.[17] The small volume of sample required

for diamond-anvil studies meant that it became possible to carry out high-pressure X-ray diffraction studies safely. For example, Weir *et al.* reported the compressibilities of single crystals of $Pb(N_3)_2$, $Ba(N_3)_2$, KN_3, TlN_3 and NaN_3 to a maximum pressure of 2.2 GPa.[18] Subsequent high-pressure studies have utilised volumetric analysis, thermal analysis and spectroscopy to extend this field to other inorganic azides and to higher pressures. A summary of this body of work is included in the following sections.

In this study, the structural properties of a series of binary azides are to be investigated at extreme conditions: the ionic azides NaN_3, CsN_3, TlN_3 and NH_4N_3, and the co-ordinative azides AgN_3 and $Pb(N_3)_2$. This chapter focuses on the structural characterisation of the 'simple' inorganic azides (NaN_3, CsN_3 and TlN_3) by a combination of X-ray and neutron powder diffraction. The results of neutron powder diffraction studies during the compression of ammonium azide, silver azide and lead(II) azide, meanwhile, are discussed in Chapter 6.

5.2 Polymorphism of the 'Simple' Inorganic Azides

5.2.1 NaN_3

Sodium azide may adopt either of two crystal structures at atmospheric pressure, depending on temperature. The high-temperature β-form ($T > 292$ K) was shown to adopt rhombohedral symmetry ($R\bar{3}m$) by Hendricks and Pauling (1925) [19]; this structure was subsequently refined by several research groups.[8, 20-22] The rhombohedral structure of the β-form may be regarded as a distortion of the cubic NaCl structure in which the chloride anions are replaced by the rod-like azide ions (N_3^-). The azide ions lie parallel to the body diagonal of the former NaCl unit cell (see Figure 5.1) and the body diagonal thus becomes elongated. From this structure it is then preferable to re-define the unit cell in keeping with crystallographic convention and thus the rhombohedral setting is chosen. From Figure 5.1 it is also clear that β-NaN_3 may also be described as a layered structure with alternating layers of sodium and azide ions parallel to the (111) direction, which is consistent with the cubic close packing of spherical ions. Within these layers, the azide ions are aligned perpendicular to the plane of the azide layer.

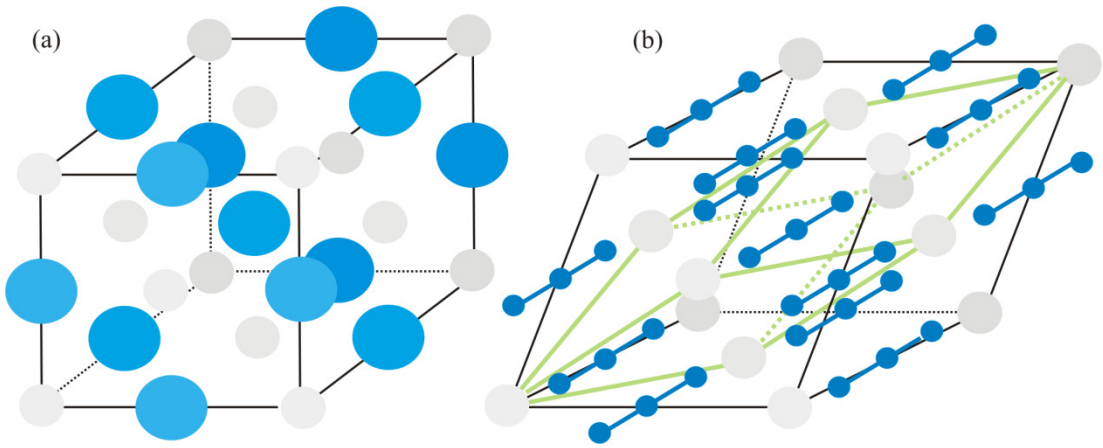

Figure 5.1 Comparison of the structures of NaCl and β-NaN_3: (a) the face-centred cubic structure of NaCl is elongated along the body diagonal upon the substitution of Cl^- with N_3^-, resulting in (b) the rhombohedral structure of β-NaN_3, the unit cell of which is shown in green. In both diagrams the Na^+ cations are shown in grey; the anions meanwhile are blue.

On the basis of their neutron diffraction measurements, in which the lateral distances between Na^+ and N_3^- units in the same layer are longer than expected and the N-N bond is shorter than expected, Choi and Prince suggest that the azide ions are tilted about the three-fold axis in a disordered manner which preserves the overall $\bar{3}m$ symmetry.[21] This model is consistent with the dynamic disorder model proposed by Iqbal, on the basis of his Raman spectroscopic observations.[23] The calculated orientational density distribution of the azide ions based on this model is in good agreement with the electron density maps of Stevens and Hope that are distinctly triangular in shape with the apexes pointing between the neighbouring Na^+ ions.[22]

It is also possible to define a monoclinic unit cell for β-NaN_3 that facilitates comparison with the low temperature α-form (*C*2/*m*), see Figure 5.2. The structure of α-NaN_3 was first determined by X-ray powder diffraction on samples cooled from the β-form.[8] (The phase transition was first observed during electron paramagnetic resonance measurements of Mn^{2+} doped crystals although the α-form was (wrongly) assumed to have orthorhombic symmetry [24]). Observations in the X-ray powder diffraction patterns led the authors to propose a displacive model for the β → α transition in which the layers of sodium atoms are sheared perpendicular to the *b*-axis and the azide ions are tilted away from the original body diagonal (see Figure 5.2). The structure of the α-form was later confirmed by a combination of X-ray single-crystal and powder diffraction.[25]

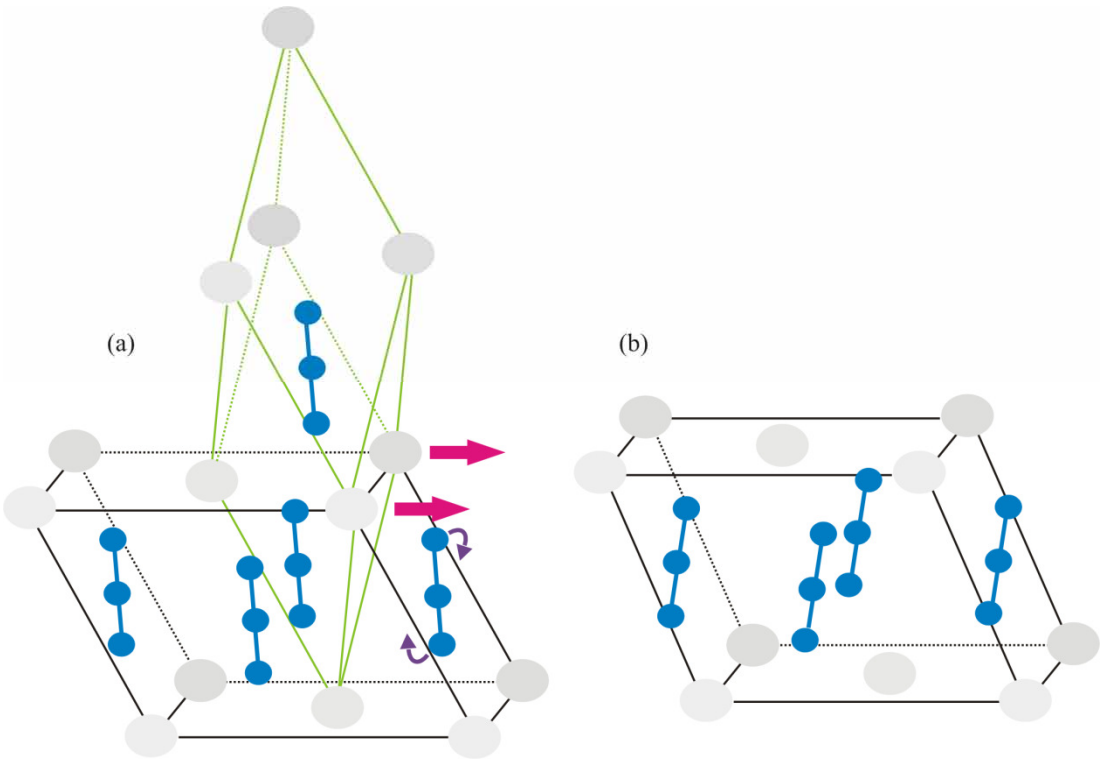

Figure 5.2 Comparison of β- and α-NaN_3: (a) in addition to the rhombohedral unit cell (shown in green), a monoclinic structure may be selected for β-NaN_3. Upon the β → α transition, the azide anions (blue) undergo a slight rotation and the cation (grey) layers are sheared. The monoclinic structure of α-NaN_3 is shown in (b).

The β → α phase transition in sodium azide (observed at a transition temperature, T_c, between 286 and 295 K [26]) has been studied by numerous analytical techniques in order to establish its true nature, *i.e.* is it weakly first order or a continuous second-order phase transition? Initially an order-disorder model was favoured, which explained the apparent second-order behaviour.[8, 27, 28] This was supported by the observation that degenerate Raman modes split [23, 26] and is consistent with the disordered model of the high-temperature phase proposed by Choi and Prince on the basis of their neutron diffraction experiments.[21]

Heat capacity measurements were unfortunately ambiguous [29, 30]: any discontinuities or thermal hysteresis loops were too small for the authors to be confident enough to exclude experimental error. Furthermore the result was significantly dependent on sample preparation – inhomogeneous strain within the sample gave rise to smearing of the specific heat, which could be mistaken for a continuous transition.[30] Midorikawa *et al.*, however, were able to observe by polarising microscopy a distinct phase front between two phase domains in a single crystal of sodium azide.[31] At the same time, Hirotsu's study of the birefringence of a single crystal also gave clear evidence for a first order transition.[32]

These contemporaneous results had a significant impact on opinion in the literature – subsequent observations have been contextualised using models that emphasise the displacive nature of the transition.[33-36]

Careful measurements of the unit cell parameters and symmetry-breaking shear strains as a function of temperature between 12 and 295 K confirmed that the transition involves a coupling of the canting of the azide anion (order-disorder) with the shearing of the sodium layers (displacive).[25] This is illustrated in Figure 5.2. As a final corroboration the authors report a small discontinuity in their measurements at 292.2 K that led them to conclude that this was the exact transition temperature, that the phase transition is ferroelastic and that it is weakly first order.

In addition to the considerable interest in the structural modifications of sodium azide within a few degrees of room temperature, there have been diffraction and spectroscopic studies undertaken at high temperatures and/or high pressure. Müller and Jöbstl observed no phase transitions from the β-form on heating to its decomposition point (548 K) at atmospheric pressure.[37] Increasing pressure at ambient temperature, however, seems to parallel the effect of cooling at ambient pressure. Bradley *et al*. first observed a splitting in their X-ray powder diffraction patterns upon increasing pressure to 0.25 GPa.[38] Although structure determination was not possible in this case, the authors note the similarity with the $\beta \rightarrow \alpha$ transition on cooling and propose that a similar transition could occur on compression. In their pioneering work on the compressibility of energetic materials, Weir *et al*. were able to apply the 'new' diamond-anvil cell technology to carry out single-crystal X-ray diffraction studies on NaN_3.[18] They obtained a monoclinic indexing for sodium azide at ~1.0 GPa, which was consistent with the low-temperature α-form.

Comparison of Raman spectra collected for the high-pressure form with those for the low-temperature α-form also confirmed that these were indeed the same phase.[36] Furthermore, it was possible to plot the linear pressure/temperature dependence of the β/α phase line between 0 - 0.3 GPa and 253 – 373 K. The pressure range for spectroscopic studies was later extended to 4.0 GPa by Christoe and Iqbal, who noted that the $\beta \rightarrow \alpha$ transition occurs at 0.07 GPa and that, once formed, the α-form remains stable to the highest pressures studied.[39] More recently neutron powder diffraction has been used to observe the structural response of α-NaN_3 to compression (up to a maximum pressure of 1.2 GPa). Rietveld refinement of data collected at 0.5 GPa shows that compression involves both a distortion of the unit cell and a tilt of the linear anions in the monoclinic plane.[40]

Finally, Pistorius and Campbell White report evidence of a third distinct phase of sodium azide obtained at elevated temperatures and pressures.[41] A volume discontinuity was observed during compression of the β-form at ~ 357 K (between 2.6 and 3.0 GPa). This β → γ transition is reported to be quite sluggish, but proceeded much more quickly when compression was performed at 373 K. It was also possible to observe a transition from the α-form to the γ-form at 333 K and 2.8 GPa but this transition was so sluggish at lower temperatures that it became 'virtually unobservable'.

The primary aim of the current study was to obtain neutron powder diffraction data of sufficient quality to allow structure solution of this high-pressure/high-temperature γ-form. Given the sluggish nature of the phase transitions *to* this form, it was also hoped that by cooling to ambient temperature before decompressing it would be possible to recover γ-NaN_3 to ambient pressure. Furthermore compression of sodium azide at ambient temperature (to 6.0 GPa) was carried out in order to assess critically the compression mechanism proposed by Knorr and Depmeier.[40]

5.2.2 CsN_3

While structures related to the NaCl structure are typical for compounds with small cations like Li^+ and Na^+, azides of larger alkali metals (K^+, Rb^+, Cs^+) adopt structures closely related to CsCl. Again the substitution of the spherical chloride anions with the rod-like N_3^- ions gives rise to a distortion of the cubic lattice, but CsN_3-II (as well as KN_3 and RbN_3) crystallises in the tetragonal space group *I*4/*mcm* at ambient temperature and pressure.[42] Figure 5.3 illustrates this tetragonal distortion and highlights the alternating layers of Cs^+ and N_3^- ions that lie perpendicular to the tetragonal *c*-axis. In contrast to NaN_3, within the azide layers the anions are oriented perpendicular to their nearest neighbours. This is electrically very favourable because the electronegative termini of the azide units are directed at the electropositive central nitrogen of the next nearest anion. Furthermore the caesium cations are surrounded by the terminal N-atoms of eight azide ions in a slightly distorted square antiprism (see Figure 5.4), which is extremely advantageous in terms of electrostatic energy.[43, 44]

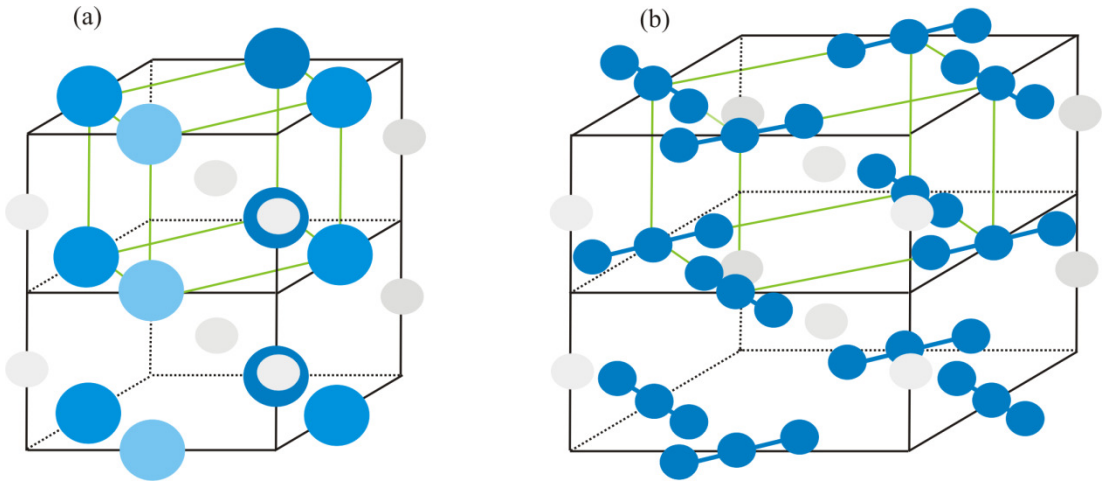

Figure 5.3 Comparison of (a) the cubic structure of CsCl and (b) the tetragonal structure of CsN_3-II. The unit cell of the cubic form is highlighted in green. The inclusion of the linear anions in CsN_3 gives rise to a lengthening of the unit cell *a*- and *b*-axes, while the alternating layers of azide layers results in a doubling of the *c*-axis.

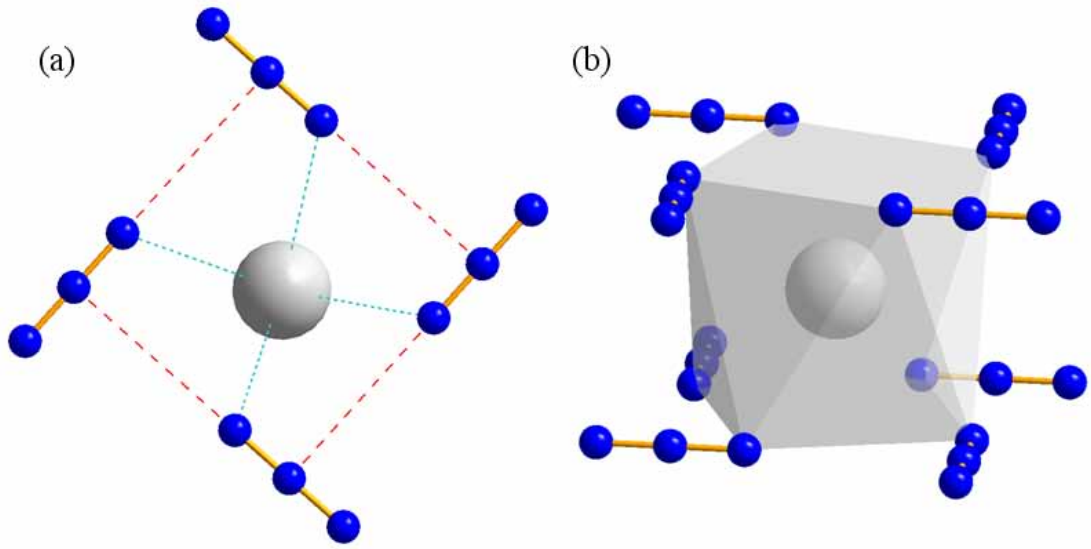

Figure 5.4 (a) Intraplanar interactions of azide anions (red) and their interactions with the cations located in the layers immediately above and below (cyan); and, (b) the square antiprism around a Cs^+ cation.

The tetragonal structure of CsN_3 has been investigated spectroscopically at ambient temperature [45] and on cooling to 20 K.[46, 47] At no point during the cooling experiment was a phase transition observed. Upon warming, however, CsN_3 undergoes a reversible transition (at 424 K) to a cubic phase CsN_3-I, first indexed by Müller and Jöbstl.[37] They were able to accurately reproduce the observed relative intensities in their X-ray powder diffraction patterns using a model based on the cubic CsCl phase ($Pm\bar{3}m$). In order to satisfy this cubic symmetry, however, the linear N_3^- ions would be required to either rotate freely or be randomly oriented. They concluded that free rotation is not likely to occur due to steric

hindrance and that instead the azide ions are oriented at random parallel to the edges of the cubic unit cell. In effect, a particular azide ion may be found (with equal probability) to align itself with any of the unit cell axes. This disorder model was later supported by differential thermal analysis and Raman spectroscopic observations.[47, 48] Entropy values for the I/II transition were too low to account for the free rotation of the anion (based on calculations by Müller and Jöbstl). Broadening of the R(E_g) mode associated with the hindered rotation of the N_3^- parallel to the *c*-axis is also consistent with a disordering process in which the azides 'jump' from one crystal site to another.[49] Recently, however, molecular dynamics simulations of this transition suggest that in the cubic phase the N_3^- ion can perform random hindered rotations about all three spatial axes.[50] In fact, these movements are observed on warming the tetragonal phase causing the lattice to expand along the tetragonal *c*-axis up to the point at which the cubic form is adopted.

In addition to the variable temperature studies at atmospheric pressure, Pistorius presented evidence for a phase transition from both the tetragonal and cubic phases to a high-pressure phase III. The transition pressure at room temperature was ~0.4 GPa although this moved to higher pressures when the compression was carried out at elevated temperatures.[48] The slope of the transition line (38 K/0.1 GPa) led the author to conclude (erroneously) that the tetragonal form should transform to the 'high-pressure phase' upon cooling at atmospheric pressure near 143 K – this has subsequently been disproven.[47] The existence of a high-pressure form was, however, substantiated by Iqbal and Christoe although their spectroscopic measurements indicated a slightly higher transition pressure (0.6 GPa at ambient temperature).[47] A further observation which may have significance for any attempts at structure solution is that CsN_3-III would consist of two sets of crystallographically non-equivalent N_3^- sites (based on splitting of vibrational modes over this transition). To date no structural information has been obtained for this form.

The current study therefore focussed on obtaining high-quality powder diffraction data during the compression of CsN_3 at ambient temperature in order to solve this high-pressure form III. A further aim was to extend the pressure range to 6.0 GPa, in order to identify and characterise any additional high-pressure forms.

5.2.3 TlN_3

Under ambient conditions, thallium azide has been found to be isostructural with CsN_3-II (*I*4/*mcm*), [42, 44, 51] with a contraction of the unit cell commensurate with the reduction in cationic radius.[43] Moreover, TlN_3 undergoes a reversible phase transition at 568 K to a high-temperature cubic form, which is reported to be analogous to CsN_3-I ($Pm\bar{3}m$) although

no unit cell parameters have been published for this form.[37] Spectroscopic measurements over this transition suggest a similar disorder model to the cubic form [52] although this has been disputed by a recent study by Liu *et al.* using molecular dynamics (MD) simulations to model the azide disorder.[53] They report a transition to the disordered cubic phase at a lower temperature than that observed experimentally (530 K), in which the tetragonal *c*-axis lengthens allowing the re-assignment of the unit cell whereby the high-temperature *c*-axis (*c*') can be related to the original tetragonal axes according to: $c'/\sqrt{2} = a,b$. Moreover they note the onset of azide disorder occurs below the phase transition, mirroring the results of an analogous simulation performed on CsN_3.[50] They suggest that this disordering of the anions on warming is accompanied by slight displacement of the thallium cations and the central nitrogen atoms, such that the Tl-Tl, Tl-N_{centre} and N_{centre}-N_{centre} radial distribution functions become uniform over the transition.[53]

Despite the uncertainty over the mechanism for this order-disorder phase transition, it is pleasing to compare analogous systems such as CsN_3 (but also RbN_3 and their related HF_2^- compounds) in order to perhaps rationalise their common phase behaviour. This has been summarised elegantly by Fuith who noted that the tetragonal → cubic transition temperature decreased with increasing cationic radius: larger cations open the structure more effectively in the tetragonal *c*-direction.[43]

In contrast to CsN_3, thallium azide also undergoes a reversible phase transition to a low temperature phase at 248 K. Mauer *et al*. were able to obtain an orthorhombic unit cell for this form (TlN_3-IV), but unfortunately space group determination and structure solution were not possible based on their X-ray powder diffraction data. Furthermore single crystals did not remain intact over this transition.[54] Studies utilising vibrational spectroscopy to investigate TlN_3 at low temperatures found supporting evidence for this transition at similar temperatures (233 – 240 K).[26, 55]

The observation that the transition to the low temperature form was rapid, with a volume change of < 0.1% [54] led Pistorius to conclude that this form was distinct from the high-pressure phase III that he reported in 1969.[48, 56] In his original high-pressure study he noted a sluggish phase transition at 0.7 GPa upon compression at room temperature (Weir *et al.* report the reconstructive phase transition to be between 0.3 and 0.54 GPa [18]). In order to compare this form with the low temperature phase IV, he subsequently carried out a similar compression study at ~ 240 K. He not only observed the transition to TlN_3-IV upon cooling but also a transition at 246 K and 0.15 GPa that was assumed to be to the high-pressure phase III.[56]

A later spectroscopic study proposed a structural model for this high-pressure phase based on the orthorhombic structure of silver azide (*vide infra*) based on more vibrational modes being observed in the Raman spectrum of the high-pressure form.[57] This lattice is derived from the tetragonal structure by means of an out-of-plane rotation of the N_3^- ions, resulting in two crystallographically distinct azide sites, hence the observed splitting. In the current study, neutron powder diffraction was utilised to structurally characterise this form (to test this hypothesis) and to investigate its phase stability up to a maximum pressure of 7.0 GPa. Furthermore, variable temperature X-ray diffraction was performed in order to allow structure solution of the low-temperature TlN_3-IV and to provide experimental evidence for the high-temperature form I, thus complementing previous computational studies.

5.2.4 A Note on Nomenclature

It should be noted that no consensus exists in the literature regarding the naming of different polymorphs of the inorganic azides. Both Greek letters and Roman numerals are used, at times interchangeably. While confusing, every effort has been made in this thesis to follow the generally accepted naming scheme for each individual compound. In order to facilitate comparison between the various forms, the important crystallographic information for each polymorph is presented in Table 5.1, along with the pressure/temperature conditions at which each form is found.

5.3 Aims

Table 5.1 highlights not only the rich polymorphism of these relatively simple materials but also the relative dearth of structural data at non-ambient conditions. The overarching aim of this study was therefore to structurally characterise this series of inorganic azides at high pressure, and, in the case of sodium azide, at high temperature *and* high pressure. Finally the ambient-pressure polymorphism of thallium azide was explored by variable temperature X-ray powder diffraction.

Polymorph	Space Group	*a* (Å)	*b* (Å)	*c* (Å)	*α* (°)	*β* (°)	*γ* (°)	Atomic positions?	*P*/*T* conditions	Ref.
α-NaN_3	*C*2/*m*	6.1654(5)	3.6350(3)	5.2634(6)	90	107.543(5)	90	Yes	Ambient *P*; *T* < 292 K *P* > 0.07 GPa; Ambient *T*	[25],[39]
β-NaN_3	$R\bar{3}m$	3.646(2)	3.646(2)	15.213(5)	90	90	120	Yes	Ambient *P*; *T* > 292 K	[8]
γ-NaN_3	-	-	-	-	-	-	-	-	*P* > 3.0 GPa; *T* > 373 K	[41]
CsN_3-I	$Pm\bar{3}m$	4.53(1)	4.53(1)	4.53(1)	90	90	90	No	Ambient *P*; *T* > 424 K	[37]
CsN_3-II	*I*4/*mcm*	6.5412(4)	6.5412(4)	8.0908(5)	90	90	90	Yes	Ambient *P*; *T* < 424 K	[44]
CsN_3-III	-	-	-	-	-	-	-	-	*P* > 0.6 GPa; Ambient *T*	[47]
TlN_3-I	$Pm\bar{3}m$	-	-	-	90	90	90	No	Ambient *P*; *T* > 568 K	[37]
TlN_3-II	*I*4/*mcm*	6.208(1)	6.208(1)	7.355(2)	90	90	90	Yes	Ambient *P*; 248 K < *T* < 568 K	[44]
TlN_3-III	-	-	-	-	-	-	-	-	*P* > 0.7 GPa; Ambient *T*	[48]
TlN_3-IV	-	8.7178(6)	8.7655(7)	7.3659(7)	90	90	90	No	Ambient *P*; *T* < 248 K	[54]

Table 5.1 Structural information for all polymorphs of sodium azide, caesium azide and thallium azide.

5.4 Experimental

5.4.1 Materials

Polycrystalline samples of NaN_3 (99.5%) and CsN_3 (99.95% purity) were purchased from Sigma-Aldrich and used as received. Thallium azide was prepared by the precipitation reaction of Tl_2SO_4 and NaN_3. Sample purity was confirmed by ambient pressure X-ray diffraction for NaN_3, CsN_3 and TlN_3.

5.4.2 High-Pressure Neutron Powder Diffraction

High-pressure neutron powder diffraction data were collected using the PEARL/HiPr diffractometer at the UK spallation neutron source, ISIS, at the STFC Rutherford Appleton Laboratory. Polycrystalline samples of each compound under investigation (NaN_3, CsN_3, and TlN_3) were loaded, in turn, into an encapsulated TiZr gasket [58] with perdeuterated methanol:ethanol (4:1) as pressure-transmitting medium and Pb as pressure calibrant.[59] The capsule assembly was then compressed with a type V3b Paris-Edinburgh (P-E) press equipped with standard single toroid anvils with cemented WC cores (Ni binder).[60] The P-E press ram pressure was monitored and varied by means of a computer-controlled hydraulic system.

Time-of-flight (ToF) neutron powder diffraction data were collected using the $2\theta = 90°$ detectors with a transverse (through-anvil) scattering geometry. The resulting summed pattern was then normalised with respect to the incident beam monitor and the scattering from a standard vanadium calibration sample. Lastly, the diffraction pattern intensity scale was corrected for the wavelength and scattering-angle dependence of the neutron attenuation by the anvil (WC) and gasket (TiZr) materials. Full-profile Rietveld refinements of the ToF neutron powder diffraction patterns were carried out using the GSAS package, in which a convolution of Gaussian (with coefficient σ_1) and Lorentzian (γ_1) functions was used to describe peak profiles (GSAS ToF profile 3).[61] Details of any restraints applied (when necessary) during refinement will be outlined in the relevant sections below.

5.4.3 High-Pressure/High-Temperature Neutron Powder Diffraction

In addition to the ambient temperature compression experiment described above, NaN_3 was investigated at high pressure *and* high temperature at the PEARL/HiPr beamline (ISIS). In this case, a Paris-Edinburgh V4 cell was equipped with a variable temperature insert to allow rapid heating and cooling *in situ*.[62] Perdeuterated methanol:ethanol (4:1) was used as the pressure-transmitting medium and pressures were calibrated to an internal Pb standard. Data were collected and processed using the procedure outlined in Section 5.4.2.

5.4.4 High-Pressure X-ray Powder Diffraction

The X-ray powder diffraction experiment on CsN_3 was performed using a Merrill-Bassett diamond-anvil cell (DAC) [63] equipped with 600 μm culet diamonds and a 250 μm thick tungsten gasket (pre-indented to a thickness of 100-150 μm) with a 300 μm hole. Pressure measurement was made by monitoring the R_1 fluorescence line of ruby spheres [64] and hydrostaticity was maintained by using methanol:ethanol (4:1) as pressure-transmitting medium. Data were collected at the Extreme Conditions Beamline (I15) at Diamond Light Source (λ = 0.44492 Å). The X-ray beam was collimated to a diameter of 50 μm and samples were exposed for 10 s. 2D diffraction patterns were collected using a Mar345 image plate, processed using FIT2D.[65] Le Bail refinements of the powder diffraction patterns were completed using GSAS.[61]

5.4.5 Ambient Pressure X-ray Powder Diffraction

The purities of NaN_3, CsN_3 and TlN_3 were confirmed by ambient pressure X-ray powder diffraction. Data were collected in reflection mode, on a Bruker D8 Advance Diffractometer (Cu $K\alpha_1$ radiation) equipped with a position sensitive detector (PSD).[66] An exposure time of 1 hr over a 2θ range of 10 – 60° was sufficient in each case to verify sample purity.

Low-temperature X-ray powder diffraction data were collected for TlN_3 in transmission mode (capillary diameter 0.5 mm) using a Bruker D8 Advance Diffractometer [67] (Cu $K\alpha_1$ radiation) equipped with a Lynxeye Si PSD detector and an Oxford Crystostream low-temperature device.[68] In order to ensure comprehensive powder averaging throughout the complete 2θ range, data were collected for 8 hrs at 293 K, and at 100 K to allow structure solution of the low-temperature TlN_3 form IV. Shorter data collections (1 hr) were performed at 20 K intervals between 80 and 280 K. Rietveld refinement of each diffraction pattern data was undertaken in GSAS in which a convolution of Gaussian (GU, GV), Lorentzian (LX, LY) and asymmetry (asym) coefficients was implemented to fit peak profiles (GSAS CW profile 2).[61]

Finally, the high-temperature phase transition in TlN_3 was investigated by X-ray powder diffraction on a Bruker D8 Advance Diffractometer (reflection mode).[66] The sample was mounted in a TTK-450 variable temperature stage [69] and data were collected using a position sensitive detector (Cu $K\alpha_1$ radiation). X-ray powder diffraction patterns were collected over a 2θ range of 15 – 60° (4 hr) at 20 K intervals between 300 and 560 K; additional data were collected in the temperature range immediately surrounding the reported transition temperature (568 K). Le Bail refinements of the powder diffraction patterns were carried out using GSAS.[61]

5.5 Results and Discussion

5.5.1 NaN_3

High-Pressure, Ambient-Temperature Neutron Diffraction Study

The initial aim of this study was to obtain an accurate value for the pressure at which the rhombohedral β-form transforms to the monoclinic α-form. For this reason, the load applied to the sample initially was minimal (6 tonnes, typically enough to seal the sample capsule without increasing sample pressure). Refinement of the unit cell parameters of the internal Pb pressure marker and comparison with its equation of state at 293 K [59] showed that the sample was indeed at atmospheric pressure. The neutron powder diffraction pattern collected at this stage showed reasonable agreement with the pattern calculated based on the structure of the β-form (see Figure 5.5). On closer inspection however there appeared to be some broadening in the two main peaks (~3.0 Å) as well as a degree of asymmetry, particularly in the peak at d = 3.1 Å.

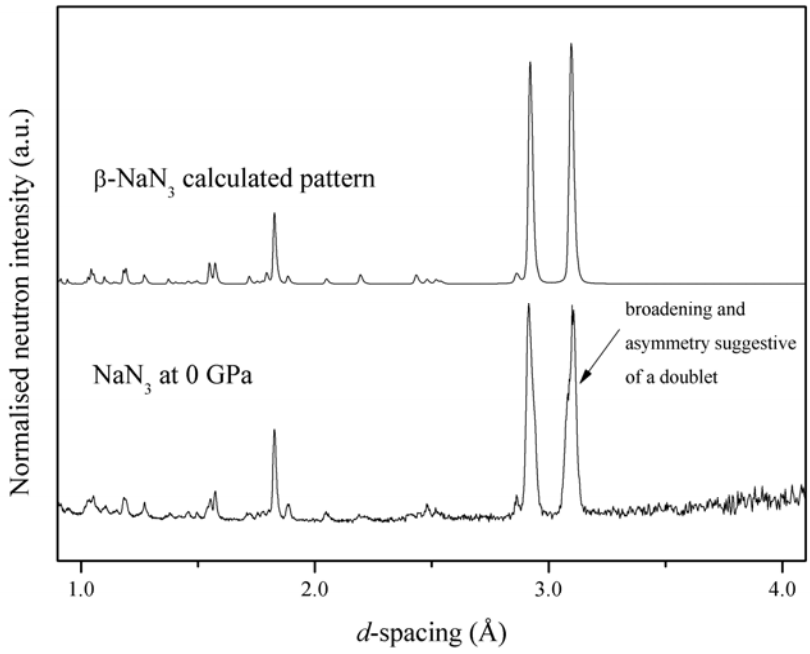

Figure 5.5 Comparison of the neutron powder diffraction pattern collected for NaN_3 at 0 GPa with the pattern calculated for β-NaN_3.

While the atmospheric temperature in the experimental hall (July) was above 293 K for the initial runs of this study, it is certainly possible that the experimental hutch may have been cooler than the rest of the facility (i.e. T < 292 K), which would result in the *thermal* phase

transition to the α-form. Using the monoclinic structure as a model for the refinement, it was then possible to achieve a much better fit to the experimental data, which was reflected in lower values for the goodness-of-fit, χ^2, (1.58 vs 3.60) and the weighted R-factor (0.048 vs 0.134). Addition of 1 tonne in load, which resulted in a pressure increase of 0.1 GPa, resulted in much better resolution of the four peaks in the region where there were only two in the rhombohedral phase (~3.0 Å), see Figure 5.6.

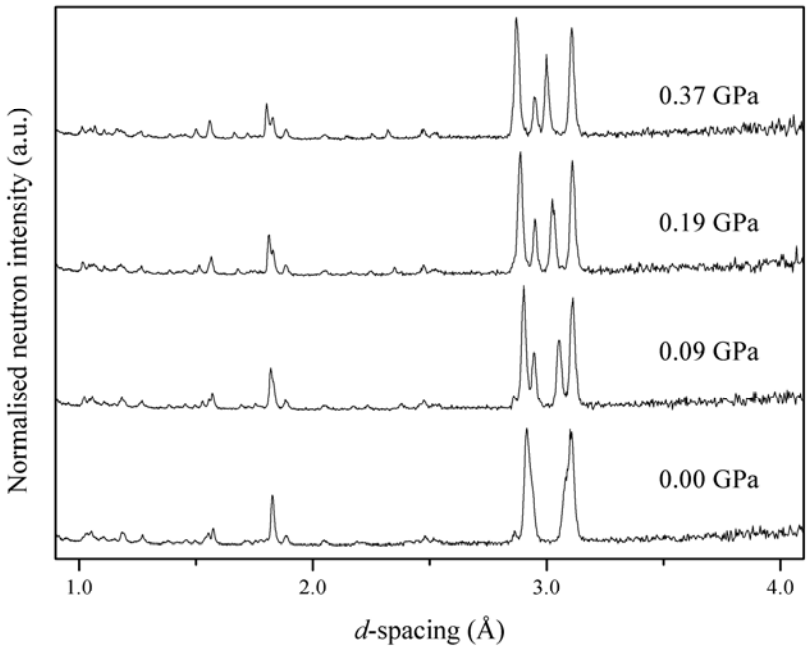

Figure 5.6 Neutron powder diffraction patterns collected for α-NaN_3 between 0.0 and 0.4 GPa, highlighting the splitting of the two peaks attributable to the rhombohedral β-form into four peaks in the monoclinic α-form.

It was then possible to use the α-structure as a model for refinement of all of the diffraction patterns collected up to the maximum pressure studied (6.06 GPa), indicating that α-NaN_3 does not undergo a phase transition in this pressure regime. A multiplot of all of the diffraction patterns collected during compression can be found in Figure 5.7, while the unit cell parameters for α-NaN_3 at each pressure are tabulated in Table 5.2 and plotted in Figure 5.8.

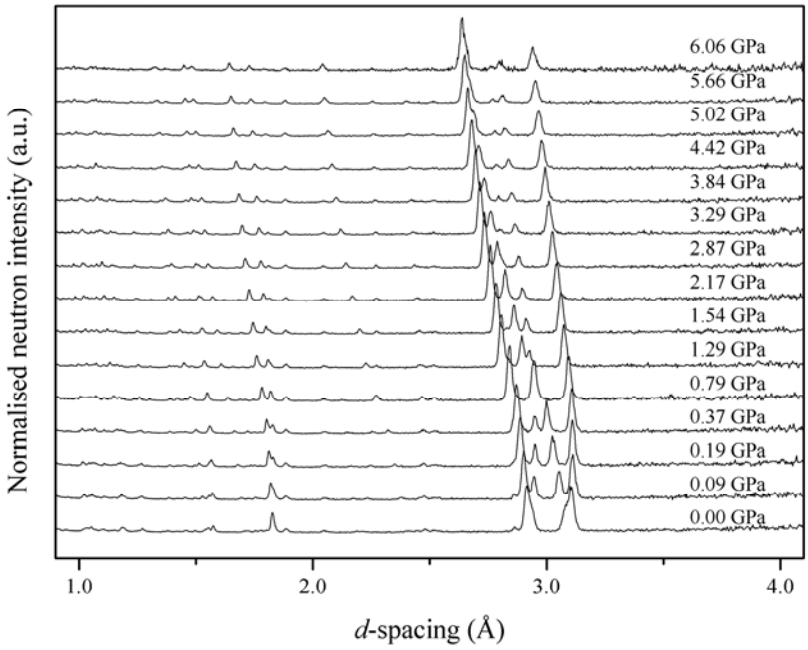

Figure 5.7 Multiplot of the neutron powder diffraction patterns collected for α-NaN_3 during compression to a maximum of 6.06 GPa. Other than the gradual movement of peaks to lower *d*-spacing with pressure, no changes indicative of a phase transition are observed.

P (GPa)	*a* (Å)	*b* (Å)	*c* (Å)	*β* (°)	*V* (Å^3)	wR_p
0.00	6.3027(4)	3.6526(2)	5.4525(8)	111.551(9)	116.748(14)	0.048
0.09	6.2785(4)	3.6552(2)	5.4070(7)	110.458(8)	116.260(12)	0.059
0.19	6.2483(4)	3.6529(2)	5.3654(7)	109.490(8)	115.445(12)	0.059
0.37	6.2169(3)	3.6478(2)	5.3284(6)	108.687(7)	114.468(11)	0.056
0.79	6.1476(4)	3.6305(2)	5.2588(6)	107.212(9)	112.114(11)	0.055
1.29	6.0720(4)	3.6069(2)	5.1935(6)	105.860(7)	109.413(11)	0.072
1.54	6.0228(4)	3.5901(2)	5.1570(5)	105.086(7)	107.664(10)	0.058
2.17	5.9664(4)	3.5689(2)	5.1160(5)	104.237(7)	105.592(10)	0.061
2.87	5.9122(4)	3.5474(2)	5.0802(5)	103.494(7)	103.607(10)	0.065
3.29	5.8687(4)	3.5298(2)	5.0536(6)	102.909(7)	102.040(10)	0.072
3.84	5.8259(4)	3.5111(2)	5.0280(6)	102.376(8)	100.460(11)	0.073
4.42	5.7879(5)	3.4931(2)	5.0061(6)	101.931(8)	99.027(11)	0.075
5.02	5.7510(5)	3.4766(2)	4.9859(7)	101.506(9)	97.683(12)	0.090
5.66	5.7175(6)	3.4606(2)	4.9685(7)	101.128(10)	96.457(13)	0.084
6.06	5.6924(12)	3.4474(5)	4.9552(14)	100.836(20)	95.51(3)	0.252

Table 5.2 Variation in the unit cell parameters of α-NaN_3 with pressure.

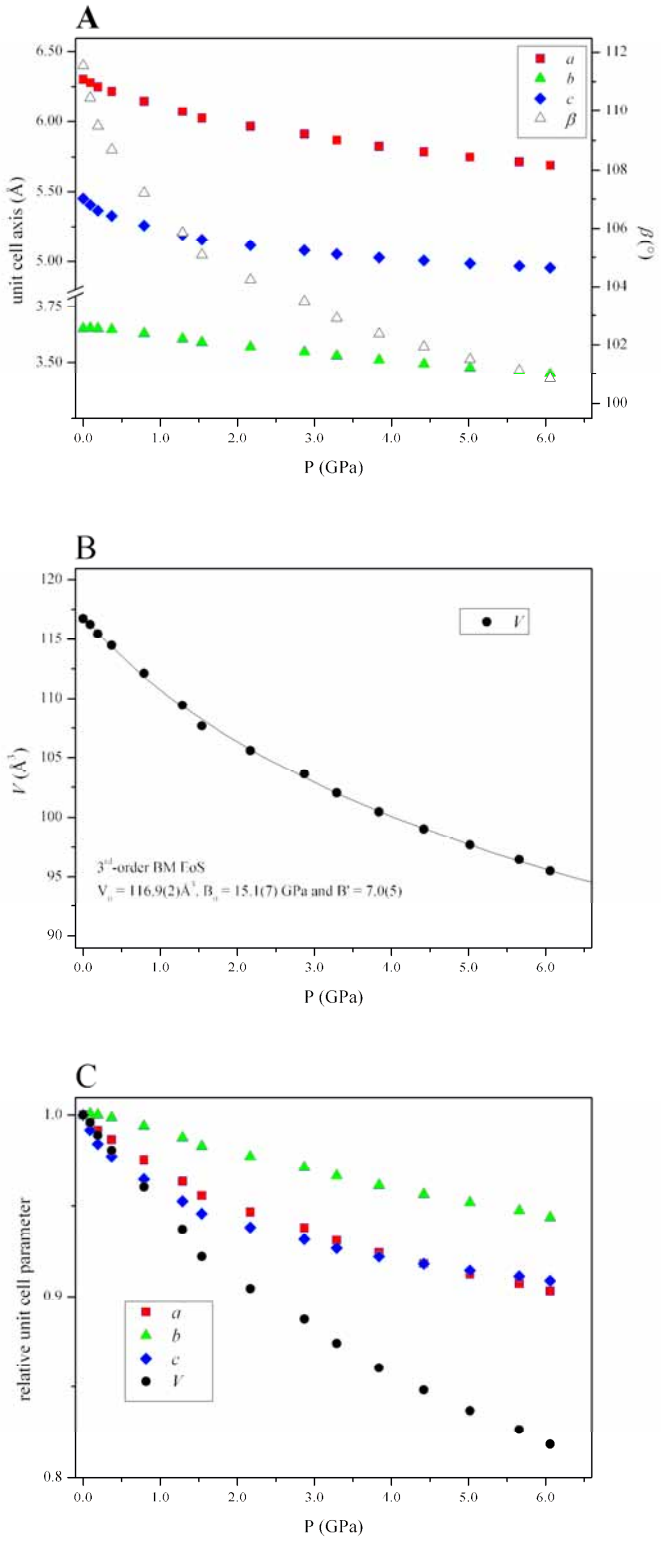

Figure 5.8 (a) Compression of the unit cell parameters (*a*, *b*, *c*, and *β)* of α-NaN_3; (b) smooth variation of unit cell volume, *V*, with pressure, including 3rd-order Birch-Murnaghan EoS; and, (c) relative compression of the unit cell parameters.

The relative compression of the unit cell axes highlights that the *b*-axis is significantly less compressible than either of the other two, which is consistent with previous compressibility measurements.[18] The greater compressibility of the *a*-axis is perhaps to be expected – this is the direction perpendicular to layers made up of alternating Na^+ and N_3^- ions (see Figure 5.9). In the case of the *c*-axis, however, its contraction is accompanied by the sharp reduction in the β-angle (from 111.5° to 100.8° over 6.0 GPa). Examination of the crystal structure allows one to rationalise the concerted contraction of the *c*-axis and the monoclinic angle in terms of a rotation of the azide ions within the *ac*-plane. Comparison of the structure determined at 5.66 GPa with the ambient pressure structure (during the same experiment) shows that the azide ion is becoming more oblique to the *c*-axis, allowing the Na^+ cations to pack more closely (see Figure 5.9). This compression mechanism is in line with that reported by Knorr and Depmeier.[40]

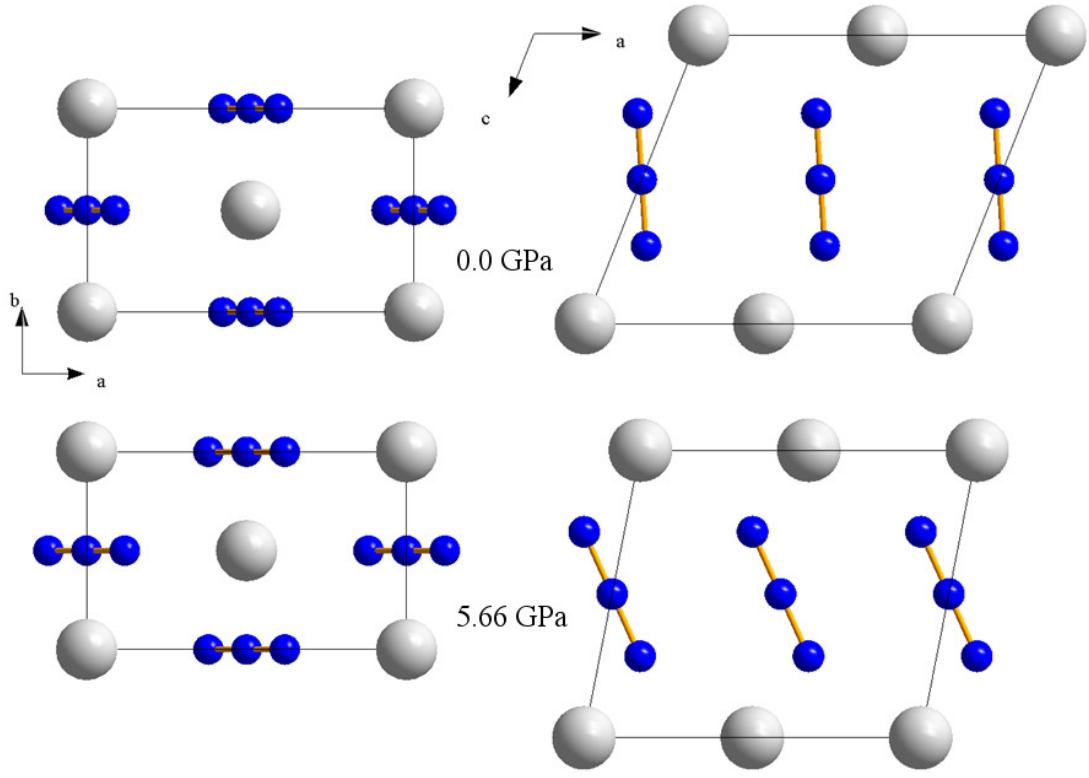

Figure 5.9 Comparison of the structures determined at 0.0 GPa and 5.66 GPa: viewed down the *c*-axis to highlight the interplanar contraction of the *a*-axis; and viewed down the *b*-axis to show the rotation of the azide anions in the monoclinic plane.

Moreover the rotation of the azide within the monoclinic plane can be represented graphically by plotting the variation in the angles created between the linear anion and the unit cell *a*- and *c*-axes throughout the compression. These can be found in Figure 5.10, which shows that this rotation does not display a linear dependence on pressure but seems to

approach a limit at the maximum pressure studied (6.06 GPa). It would therefore be very interesting to conduct further structural studies beyond this pressure range to investigate how the unit cell compression manifests itself, and whether further compression may, in fact, induce a phase transition.

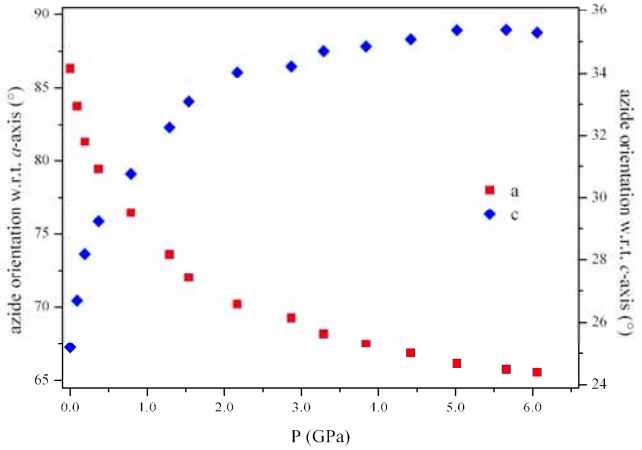

Figure 5.10 Azide ion orientation with respect to the *a*- and *c*-axes upon compression.

An interesting aspect of the compression of the *b*-axis is that it initially undergoes a small, but significant, expansion before undergoing an almost linear contraction with pressure. The exact reason for this is still unclear, although it is certainly likely that the rotation of the anions may result from or result in this small pressure-induced expansion. It is also worth noting that the change in gradient (between the initial expansion and subsequent contraction) may, in fact, be suggestive of a second-order phase transition. No discontinuity is observed in the pressure-volume plot but this may be due to the change in the *b* parameter being masked by concurrent changes in the other parameters. Such a phenomenon has been observed in high-pressure studies of minerals – a continuous phase transition was detected in lawsonite ($CaAl_2Si_2O_7(OH)_2.H_2O$) by plotting the 'normalised stress', defined as $F_E = P/3f_E(1+2f_E)^{5/2}$, against the Eulerian finite strain $f_E = ((l_0/l)^2-1)/2$, where l_0 = unit cell parameter (*a*, *b*, *c*) at zero pressure.[70] Unfortunately it has not been possible to carry out similar analyses for sodium azide due to the lack of data points in the 'low-pressure' phase. It would therefore be desirable to collect high-quality unit cell data at very low pressure (0 – 0.3 GPa) to investigate the true nature of the change in the *b*-axis within this pressure regime.

Finally a 3rd-order Birch-Murnaghan equation of state [71] has been fitted to the isothermal compression of the unit cell volume over the pressure range 0 – 6.06 GPa, assuming no

second-order phase transitions occur. Using Angel's program EoSFIT [72] the values calculated were: V_0 = 116.9(2) Å^3, B_0 = 15.1(7) GPa and B' = 7.0(5). The unit-cell volume at zero pressure (V_0) is in excellent agreement with the value obtained experimentally (116.75(1) Å^3) determined at atmospheric pressure. Furthermore, it has been possible to construct an F_E vs f_E plot analogous to that described above for the isothermal compression of the unit cell volume, see Figure 5.11. In this case it should be noted that $f_E = ((V_0/V)^{2/3}-1)/2$. All data points lie on a straight line (correlation coefficient, R^2 = 0.8597), the intercept of which represents the bulk modulus (B_0 = 15.3 GPa). The gradient, $3B_0(B'-4)/2$, is in very good agreement with the calculated value (calc. = 67.95, m = 65.0).[73] The values of B_0 and B' calculated for α-NaN_3 show that it has very similar compressibility to the isostructural LiN_3 (B_0 = 19.1(14) GPa and B' = 7.3(5))[74] and is comparable, but slightly more compressible, than the alkali halides.[75, 76]

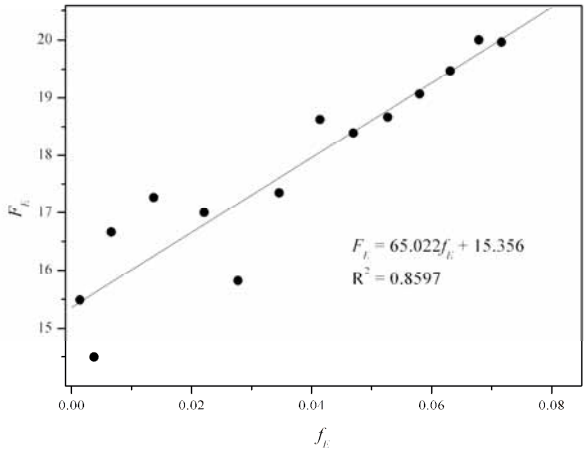

Figure 5.11 Plot of the 'normalised stress' (F_E) against Eulerian finite strain (f_E) for the isothermal compression of the unit cell volume of α-NaN_3.

High-Pressure, High-Temperature Study

In addition to characterising the high-pressure behaviour of NaN_3 at ambient temperature, the observation of a third from of sodium azide at elevated temperatures and pressures motivated further study. As in the previous study, a sample of β-NaN_3 was loaded into the sample capsule in the P-E press, but this time it was possible to characterise the pressure-induced β → α phase transition by carrying out the initial compression at 294 K. As is shown in Figure 5.12, it was possible to refine the neutron powder diffraction pattern collected at 0.13 GPa using the $R\bar{3}m$ form, but by 0.70 GPa this phase has transformed to the monoclinic α-form. The α-form was then compressed (at 294 K) to 1.91 GPa before warming and

pressurising alternately to get to the pressure-temperature regime in which Pistorius observed this new form (2.8 GPa at 333 K).[41] In accordance with the reported sluggishness of this transition, no changes in the diffraction pattern were observed during this data collection (~ 0.5 hr).

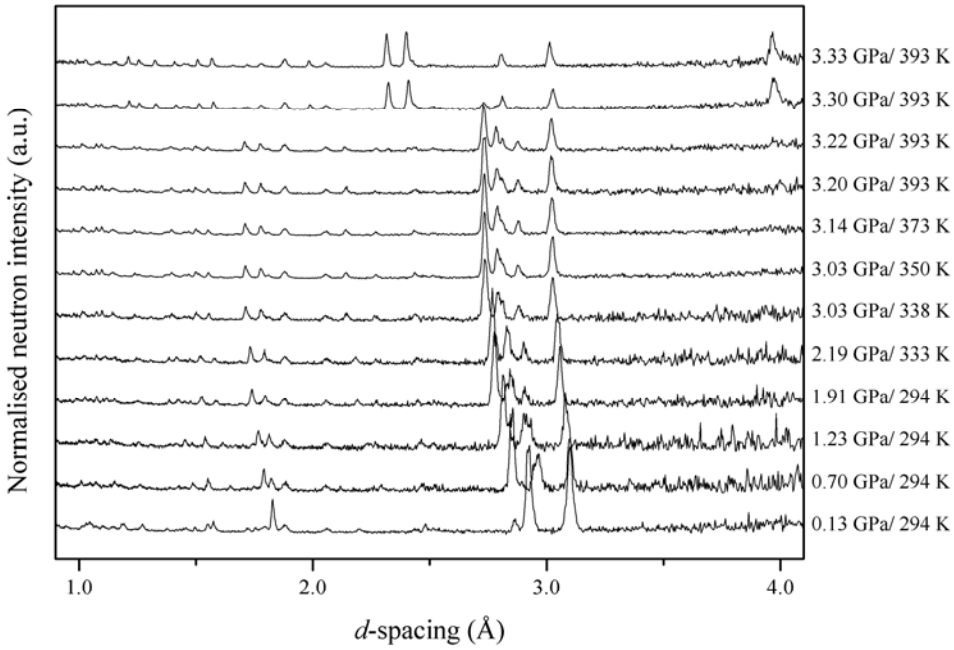

Figure 5.12 Neutron diffraction patterns collected during the compression/warming of NaN_3 to 3.33 GPa and 393 K. This multiplot shows not only the phase transition from the α-form to the γ-form, but also the β → α transition occurring between 0.13 and 0.70 GPa at 294 K.

As the rate of the α → γ transition was reported to increase at higher temperatures, the sample was warmed to 393 K at constant load, but still no changes in the diffraction patterns were evident over the course of 6 hours. Refinement of the Pb pressure marker showed, however, that the act of heating the sample resulted in an increase in sample pressure from 2.77 GPa to 3.20 GPa and it is possible that this counterbalanced the promoting influence of increasing the temperature. This is again in agreement with Pistorius's observation that the γ-form phase line has a positive slope, although according to his study, under these conditions the β-form should be present *not* the α-form.

Increasing the applied load to 40 tns at 393 K (sample pressure 3.22 GPa) resulted in the appearance of weak peaks (~2.32 and ~2.42 Å), which could not be attributed to the α-form. It was only upon further compression to 3.51 GPa, however, that a pure sample of the γ-form was observed, highlighting the significant kinetic barrier to this transition. The quality of the

diffraction pattern collected at 3.51 GPa/393 K was such that it was possible to determine the space group as *I*4/*mcm*.[77] This is the same space group adopted by the azides of the larger alkali metals and full-profile Rietveld refinement was possible using atomic co-ordinates based on the tetragonal structure of CsN_3-II. The quality of the Rietveld refinement for the γ-form is shown in Figure 5.13.

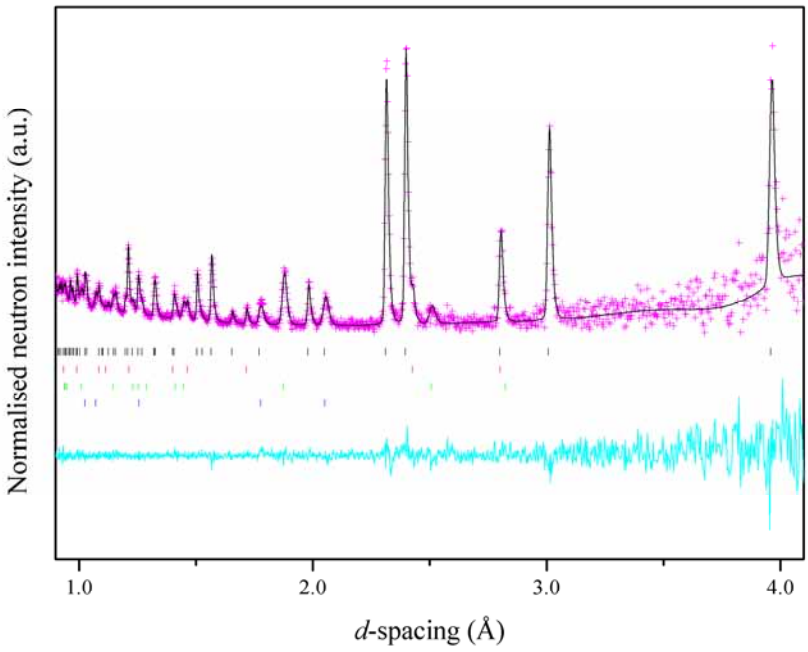

Figure 5.13 Rietveld refinement of the pattern collected for γ-NaN_3 at 3.33 GPa and 393 K. The experimental data (I_{obs}) are represented as pink crosses, the calculated pattern (I_{calc}) is shown in black and the difference (I_{obs} - I_{calc}) in cyan. Tick-marks for each phase are also shown for clarity: γ-NaN_3 (black), Pb (red), WC (green) and Ni (blue).

In the tetragonal structure of γ-NaN_3, the azide anions and sodium cations are organised intro alternating layers perpendicular to the *c*-axis. Within the layers, the azide ions are oriented normal to their nearest neighbours, resulting in the favourable interaction between the electronegative termini and electropositive central N-atom. This geometry gives rise to the square-antiprism co-ordination environment, formed by the terminal N-atoms of eight azide anions round one Na^+, rather than the very-slightly-distorted octahedral environment observed in the monoclinic form. The most significant change over the α → γ transition, however, is in the distances separating neighbouring cation layers. In α-NaN_3, each cation is surrounded by six others within the same plane (at distances of either 3.54 or 3.44 Å) and an additional two positioned directly above and below in the neighbouring layers (5.07 Å). In the tetragonal γ-form the (slight) lengthening of the intraplanar distances between

neighbouring cations (to 3.60 Å) is accompanied by a dramatic decrease in the interplanar separation (to 3.01 Å). This is highlighted in Figure 5.14. It is this dramatic shortening of the distance between the planes that results in the 7.8 % contraction of the molecular volume over the transition (between 3.22 and 3.30 GPa).

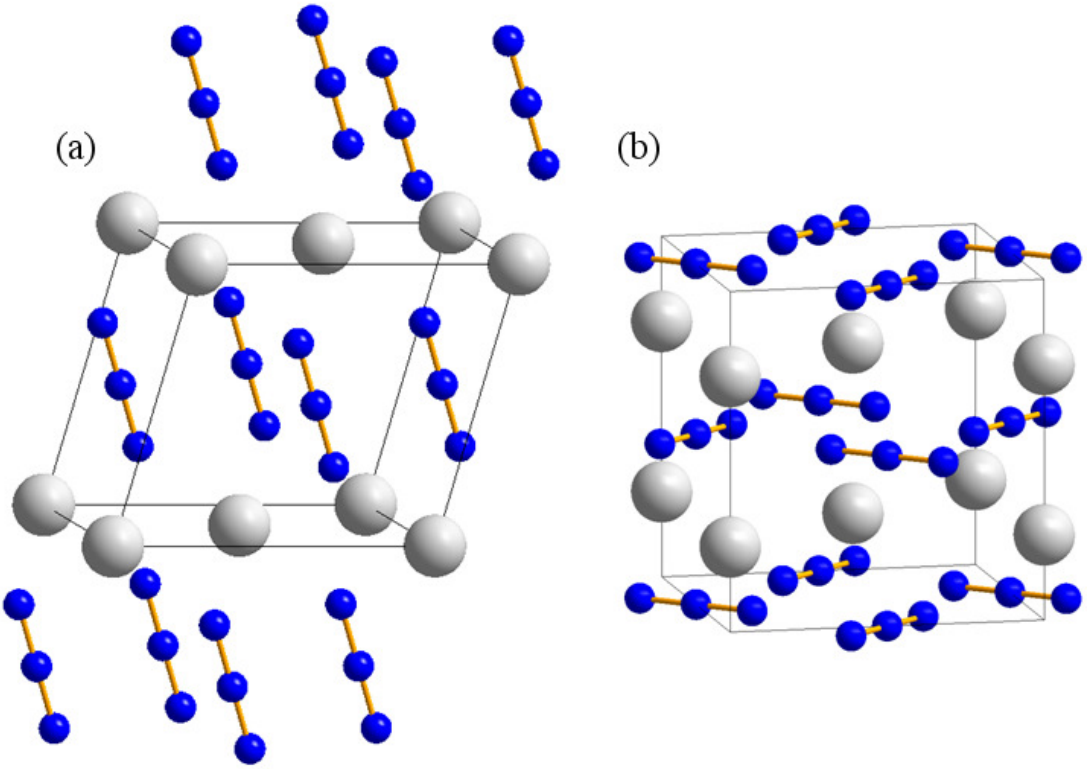

Figure 5.14 Comparison of the structures of (a) α-NaN_3 at 3.22 GPa, and (b) γ-NaN_3 at 3.30 GPa. The structures have been oriented such that the rotation of all of the azide anions over the phase transition is highlighted.

The significant amount of rearrangement in the structure (and the resultant dramatic reduction in molecular volume) explains the sluggish nature of the transition. Furthermore it suggests that the γ-form may display significant hysteresis upon cooling and subsequent decompression and may therefore be recoverable to ambient conditions. It was for this reason that we carefully monitored the cooling of γ-NaN_3 to ambient temperature (at constant load of 51 tns) as well as its decompression, in order to determine the exact conditions under which it may undergo a phase transition, most likely to the α-form.

Cooling from 393 K to 313 K (sample pressure decreased from 3.51 to 3.27 GPa) did not result in any phase transition – the unit cell parameters are tabulated below (Table 5.3). This facilitated direct comparison between the α-form obtained in the ambient temperature compression study above and the γ-form in the present study. The molecular volume of the

α-form at 3.29 GPa (293 K) is 102.909(7) Å^3, compared to 93.889(17) Å^3 obtained for the γ-form at 3.27 GPa (313 K). This clearly shows that the γ-form is the denser form (by 8.8%).

T (K)	*P* (GPa)	Form	*a* (Å)	*b* (Å)	*c* (Å)	*β* (°)	*V* (Å^3)	wR_p
294	0.13	β	3.64684(17)		15.222(3)		175.32(3)	0.106
294	0.70	α	6.1721(11)	3.6373(6)	5.2817(19)	107.66(3)	113.00(4)	0.199
294	1.23	α	6.0907(12)	3.6139(6)	5.2061(18)	106.11(2)	110.10(4)	0.314
294	1.91	α	6.0055(10)	3.5826(5)	5.1422(14)	104.82(2)	106.96(3)	0.174
333	2.19	α	5.9838(11)	3.5749(5)	5.1316(15)	104.57(2)	106.24(3)	0.211
333	2.46	α	5.9224(10)	3.5493(5)	5.0836(14)	103.64(2)	103.85(3)	0.202
338	3.03	α	5.9139(9)	3.5476(5)	5.0841(14)	103.59(2)	103.68(3)	0.199
350	3.03	α	5.9118(5)	3.5459(2)	5.0802(7)	103.55(1)	103.53(1)	0.063
373	3.14	α	5.9091(5)	3.5439(2)	5.0802(7)	103.53(1)	103.41(1)	0.066
393	3.20	α	5.9073(7)	3.5430(3)	5.0802(10)	103.53(1)	103.37(2)	0.130
393	3.22	α	5.9019(6)	3.5414(3)	5.0732(9)	104.45(1)	103.12(2)	0.083
393	3.30	γ	5.6114(3)		6.0418(4)		190.24(2)	0.082
393	3.33	γ	5.5965(3)		6.0136(4)		188.35(2)	0.082
383	3.47	γ	5.5962(4)		6.0092(6)		188.20(3)	0.195
373	3.34	γ	5.5957(4)		6.0093(5)		188.17(3)	0.146
363	3.35	γ	5.5950(3)		6.0096(4)		188.13(2)	0.089
353	3.24	γ	5.5947(4)		6.0076(5)		188.04(2)	0.205
343	3.29	γ	5.5943(3)		6.0063(5)		187.97(2)	0.149
333	3.28	γ	5.5937(3)		6.0047(4)		187.88(2)	0.077
313	3.27	γ	5.5932(3)		6.0023(4)		187.78(2)	0.078
300	2.47	γ	5.6169(4)		6.0553(6)		191.04(3)	0.116
		α	5.933(3)	3.5512(2)	5.079(5)	103.96(7)	103.85(9)	
300	1.32	α	6.068(2)	3.6006(9)	5.187(3)	105.85(4)	109.02(6)	0.207
300	0.00	α	6.2957(14)	3.6573(8)	5.434(2)	110.70(3)	117.04(5)	0.134

Table 5.3 Unit cell parameters (*a*, *c* and *V*) obtained NaN_3 throughout the variable temperature and pressure neutron powder diffraction study. The pattern collected at 300 K and 2.47 GPa was successfully refined as a mixed phase of both the α- and γ-forms; structural data for both forms is presented under these conditions.

It was only upon decompression that the first indications of a phase transition were observed – the pattern collected at 2.63 GPa (300 K) was successfully refined as a mixed phase of the α- and γ-forms. Further decompression to 1.32 GPa resulted in a clean pattern of the α-form, which remained upon decompression to atmospheric pressure. These patterns, however,

showed significant peak broadening when compared to the lowest pressure pattern obtained for the *same* form during compression (shown in Figure 5.15). Although the shorter data collection time for the recovered form has certainly resulted in a lower signal-to-noise ratio, this would be not be expected to have an effect on the observed peak-widths. Peak broadening in this case is therefore indicative of significant strain within the sample, arising from the considerable re-arrangement required during the $\gamma \rightarrow \alpha$ transition.

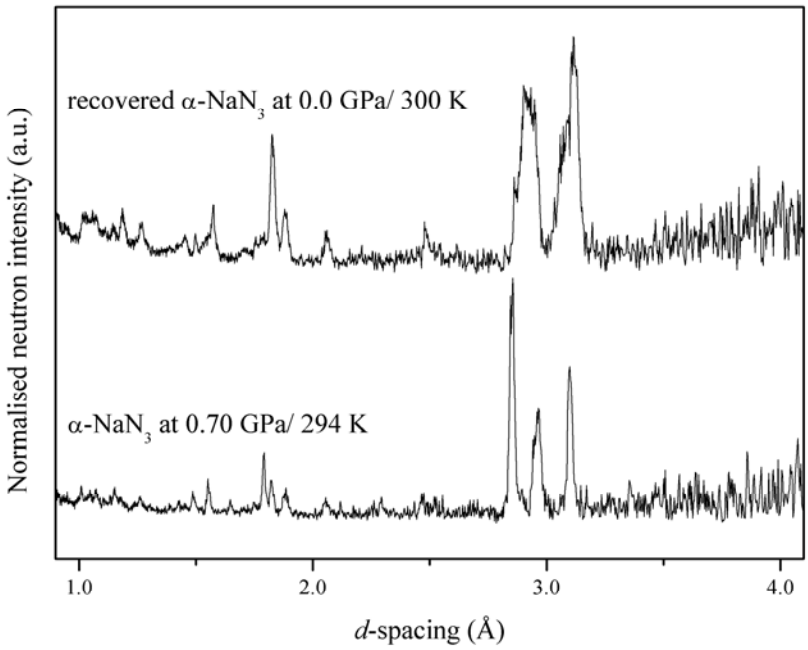

Figure 5.15 Comparison of the neutron powder diffraction patterns collected for α-NaN_3 before the high-pressure/high-temperature phase transition to the γ-form (bottom) and after decompression and cooling (top). The peak broadening in the recovered pattern is clear evidence of significant strain within the sample following the $\gamma \rightarrow \alpha$ transition.

Summary: NaN_3

The ambient-temperature, high-pressure behaviour of NaN_3 has been characterised to a maximum pressure of 6.06 GPa. It was not possible to characterise the pressure-induced $\beta \rightarrow \alpha$ phase transition, but once formed the α-form has been shown to be stable to the limit of this study. The compression mechanism involves a rotation of the azide ions within the monoclinic plane, although this seems to approach a limit at the highest pressures studied. It would therefore be intriguing to perform diffraction studies at even higher pressure to examine whether this, in fact, results in a phase transition.

In addition, the high-pressure, high-temperature polymorph of NaN_3 has been structurally characterised for the first time. This γ-form has been shown to adopt a tetragonal structure analogous to the structure adopted by the other ionic azides at ambient conditions (e.g. CsN_3 and TlN_3). In this way, the application of pressure may be regarded as being analogous to moving down a group in the periodic table, by forcing smaller metal cations to adopt higher co-ordination numbers. The considerable structural rearrangement (and dramatic reduction in volume) results in a significant kinetic barrier for the α → γ transition, which is also reflected in the hysteresis observed during cooling and decompression. Furthermore phase history has a marked effect on sample quality – samples of α-NaN_3 recovered from the γ-form show evidence of considerable crystallographic strain. Of particular importance is the effect this may have on performance characteristics, such as sensitivity.

5.5.2 CsN_3

High-Pressure Neutron Powder Diffraction Study

The ambient-temperature, high-pressure polymorphism of caesium azide has been investigated by both X-ray and neutron powder diffraction. In a similar study to the compression study of NaN_3 above, the initial aim of this experiment was to identify the transition pressure from CsN_3-II to the high-pressure form III that has previously been observed spectroscopically.[47] In contrast to the above study, not only was a transition to this form observed (at 0.32 GPa), but two further high-pressure polymorphs have also been identified. A multiplot of the neutron powder diffraction patterns collected during compression, including patterns representative of these forms, is shown in Figure 5.16.

Polycrystalline CsN_3-II (*I*4/*mcm*) was loaded into the sample capsule and its structure was confirmed by Rietveld refinement of the neutron powder diffraction pattern collected at 0.13 GPa. Compression to 0.32 GPa resulted in the appearance of weak peaks at ~2.9 and 3.1 Å which could not be fit by the tetragonal structural model. It was possible to drive this transition to completion by increasing the applied load from 8 to 9.5 tns (resulting in an increase in sample pressure to 0.54 GPa).

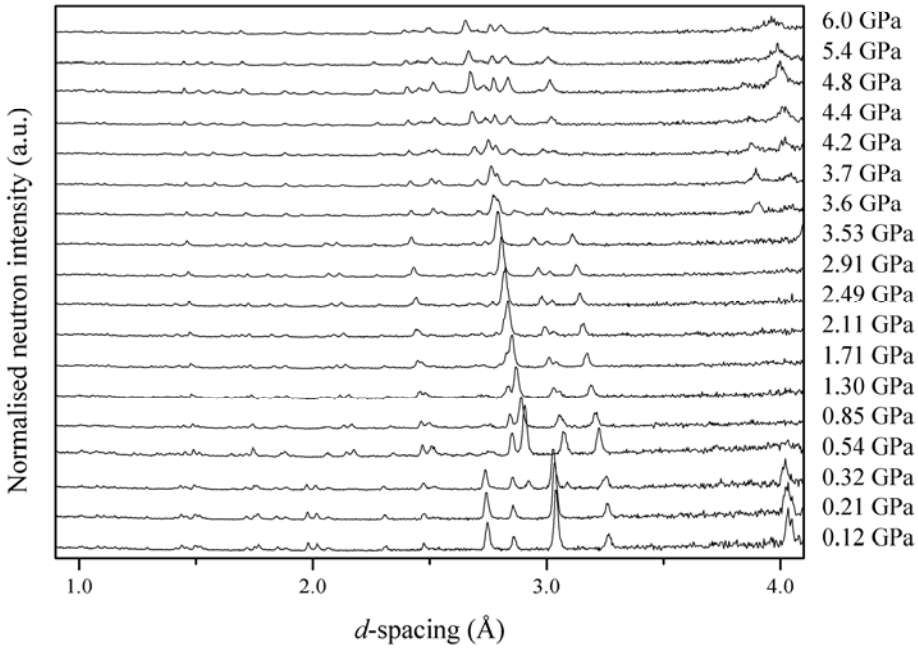

Figure 5.16 Multiplot of neutron powder diffraction patterns collected for CsN_3. The pattern collected at 0.32 GPa has features attributable to forms II and III – this transition is completed in the next pattern (0.54 GPa). Since it has not been possible to perform full-profile refinements on the patterns collected above 3.53 GPa, the pressures have been estimated based on the position of the Pb (200) and (111) peaks and are therefore less precise.

The neutron powder diffraction data collected at 0.54 GPa (3 hrs) were of sufficient quality to allow CsN_3-III to be indexed to a monoclinic unit cell; subsequent Le Bail refinement of the powder pattern using this unit cell then facilitated space-group determination ($P2_1/c$). Atomic positions were initially generated by a monoclinic distortion of the original tetragonal unit cell and subsequent Rietveld refinement. Using this structure it was possible to carry out full-profile Rietveld refinements on all of the neutron powder diffraction patterns collected for CsN_3-III, up to a maximum pressure of 3.53 GPa. It should be noted that while bond angle restraints [180(2)°] were initially applied to each of the two individual azide groups, the final cycle of refinement could be undertaken without this restraint. The unit cell parameters obtained during refinement of the neutron powder diffraction patterns are tabulated in Table 5.4 and represented graphically in Figure 5.18(a).

Comparison of the monoclinic structure of CsN_3-III with the tetragonal form II (see Figure 5.17) clearly shows that the layered structure is largely retained over the transition, although half of the azide anions undergo a 45° rotation out of the *bc*-plane. This results in alternate layers of 'flat' and 'canted' azide anions, thus accounting for previous spectroscopic

observations of two different azide environments.[47] Within the flat layer of anions each azide retains its perpendicular orientation with respect to its nearest neighbours, thus maintaining the electrostatically favourable interactions between the negative termini and positive central nitrogens. Moreover, the cations remain situated in the pocket formed by the arrangement of four terminal nitrogen atoms, although the displacement of the cation from (0.25, 0.5, *z*) results in four discrete Cs…N distances (ranging from 3.155 to 3.227 Å at 0.54 GPa). This feature, along with the rotation of alternate anion layers, gives rise to a considerable distortion of the octahedral co-ordination sphere around each cation; the 8 nearest azide termini now no longer reside in two parallel planes but in planes oriented at ~17° to one another. It is interesting to note that this angle does not vary significantly throughout compression, a feature that is reflected in the relative contraction of the Cs…N and interplanar Cs…Cs distances. No particular interaction appears to be more susceptible to compression throughout the stability range of CsN_3-III.

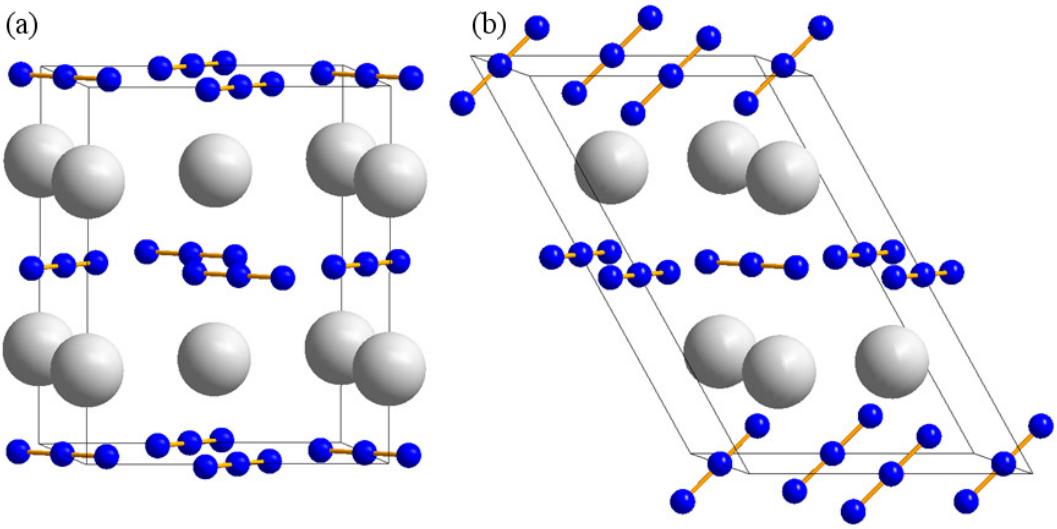

Figure 5.17 Comparison of (a) CsN_3-II and (b) CsN_3-III, highlighting the retention of the layered structure, meanwhile showing the rotation of half of the azide anions.

Compression of the unit cell appears to manifest itself primarily in the contraction of the unit cell *a*- and *b*-axes, while the *c*-axis is more resistant to compression, see Figure 5.18(c). It is likely, however, that the resistance of the *c*-axis to compression can be attributed to two competing effects; the pressure-induced contraction is partially compensated by expansion along the same direction due to the slight shearing of the layers (illustrated by the increase in the β-angle). It should also be noted that compression is not accompanied by any appreciable rotation of the azide groups with respect to the unit cell axes.

From these data it has also been possible to describe the smooth variation in unit cell volume with pressure by a 3rd-order Birch-Murnaghan equation of state (EoS) for this polymorph. In this case, V_0 has been fixed to be the unit cell volume determined by refinement of the pattern collected at 0.54 GPa (the first pressure at which pure form III is observed); all of the higher pressures have been normalised to this. The coefficients calculated in this way were: V_0 = 325.98 Å^3, B_0 = 19.7(10) GPa and B' = 5.8(11), which are consistent with values reported for caesium halides.[78] It should be noted, however, that the first pressure at which this form was observed was 0.32 GPa and it would therefore be worthwhile collecting more diffraction data over the II/III phase transition in order to determine accurately the unit cell volume (V_0) of CsN_3-III at this pressure. This would not be expected to change the absolute values of B_0 or B' dramatically and one can therefore be confident about comparisons drawn between this study and those on analogous systems.

P (GPa)	*a* (Å)	*b* (Å)	*c* (Å)	*β* (°)	*V* (Å^3)	wR_p
0.54	9.8858(8)	6.1327(7)	6.2119(10)	120.054(8)	325.98(4)	0.048
0.85	9.8325(9)	6.0968(7)	6.1949(11)	120.073(9)	321.37(5)	0.060
1.30	9.7630(10)	6.0520(7)	6.1690(11)	120.074(9)	315.43(5)	0.065
1.71	9.6986(8)	6.0084(5)	6.1449(9)	120.110(7)	309.76(3)	0.053
2.11	9.6449(10)	5.9736(7)	6.1249(11)	120.159(9)	305.12(4)	0.063
2.49	9.6005(11)	5.9457(7)	6.1076(11)	120.183(9)	301.36(4)	0.063
2.91	9.5470(8)	5.9143(5)	6.0891(9)	120.227(7)	297.07(3)	0.045
3.53	9.4861(10)	5.8756(7)	6.0686(11)	120.275(9)	292.11(4)	0.060

Table 5.4 Unit cell parameters obtained during the high-pressure neutron diffraction study of CsN_3-III.

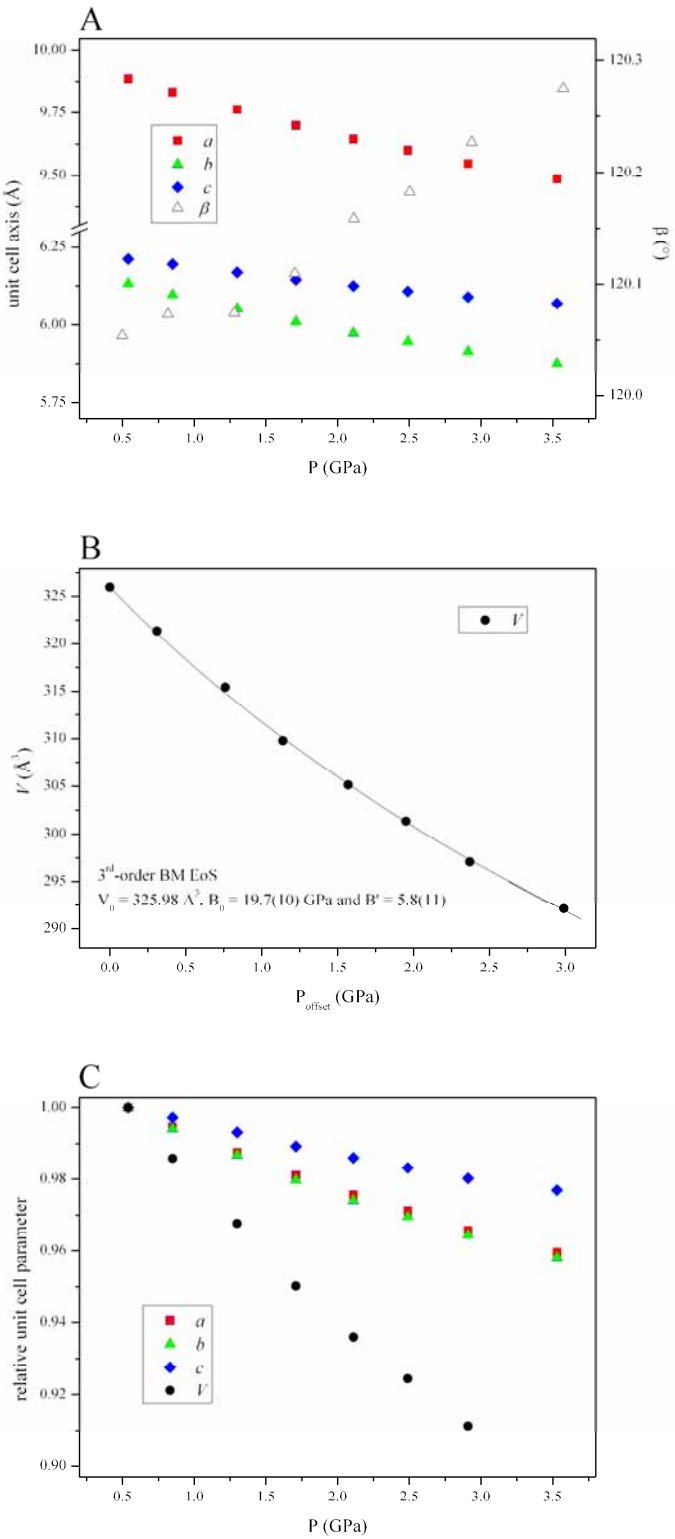

Figure 5.18 (a) compression of the unit cell parameters (a, b, c and β) of CsN_3-III over its stability range; (b) relative compression of the unit cell axes and unit cell volume (normalised to P = 0.54 GPa); and, (c) PV-plot for CsN_3-III and its representative 3rd-order Birch-Murnaghan EoS.

The pattern collected at the next pressure point (3.6 GPa[8]) showed a dramatic change, indicative of a phase transition. Further compression of this phase (CsN_3-IV) showed that its stability was limited to a pressure range of only ~1.0 GPa – a third high-pressure phase transition was observed to commence at 4.4 GPa. A clean pattern was collected for a pure form of CsN_3-V at 4.8 GPa. No further changes were observed up to the maximum pressure studied (6.0 GPa). Current efforts are focussed on obtaining unambiguous unit cells for these high-pressure phases and it is hoped that structure solution will be possible based on the neutron powder diffraction data presented herein and complementary high-pressure X-ray powder studies (*vide infra*).

Unfortunately the time constraints of this experiment meant that it was not possible to examine the decompression behaviour sufficiently to determine any hystereses. Nevertheless, examination of the diffraction pattern collected at atmospheric pressure confirmed that the tetragonal form II had been recovered and, in contrast to NaN_3 above, showed no evidence of internal strain.

High-Pressure X-ray Powder Diffraction Study

In order to complement the above neutron diffraction study, powder X-ray diffraction data were collected during the compression of caesium azide (to 3.9 GPa) at the Extreme Conditions Beamline (I15), Diamond Light Source. Diffraction patterns collected during this experiment, representative of forms II-IV, are shown in Figure 5.19. Comparison of the diffraction patterns obtained experimentally for CsN_3-III with those calculated using the structural model presented above highlighted a number of intensity mismatches, particularly in the peaks located at d = 2.11, 2.42, 2.97 and 4.22 Å in the pattern collected at 2.1 GPa (Figure 5.20). Visual inspection of the sample after data collection showed that considerable radiation damage had occurred – this dramatic effect is presented in Figure 5.21. The light colouration of the sample caused by sample centring (green lines) is thought to be due to the formation of F-centres upon irradiation – a well-documented phenomenon in alkali metal azides.[79, 80] This effect became more noticeable upon irradiation for longer exposure times (red spots correspond to 10 s; dark blue spot in Figure 5.21(b) after irradiation for 90 s) and thus is perhaps indicative of sample decomposition. This phenomenon has also previously been observed in, for example, TlN_3 (in which the unit cell volume was observed to increase after X-ray irradiation [81]) and in NaN_3 (in which 'trapped' N atoms were

[8] It should be noted that the pressures reported for the three high-pressure phases have been estimated based on the *d*-spacing of the Pb (200) and (111) peaks. In some cases these peaks were overlapped by sample peaks and the uncertainty in pressure is therefore larger than patterns for which Rietveld refinement was possible.

observed by ESR spectroscopy [82]). Furthermore it is analogous to the high-pressure photolysis (λ = 514 nm) of sodium azide reported by Peiris and Russell who propound this method for the generation of novel polynitrogen species.[4]

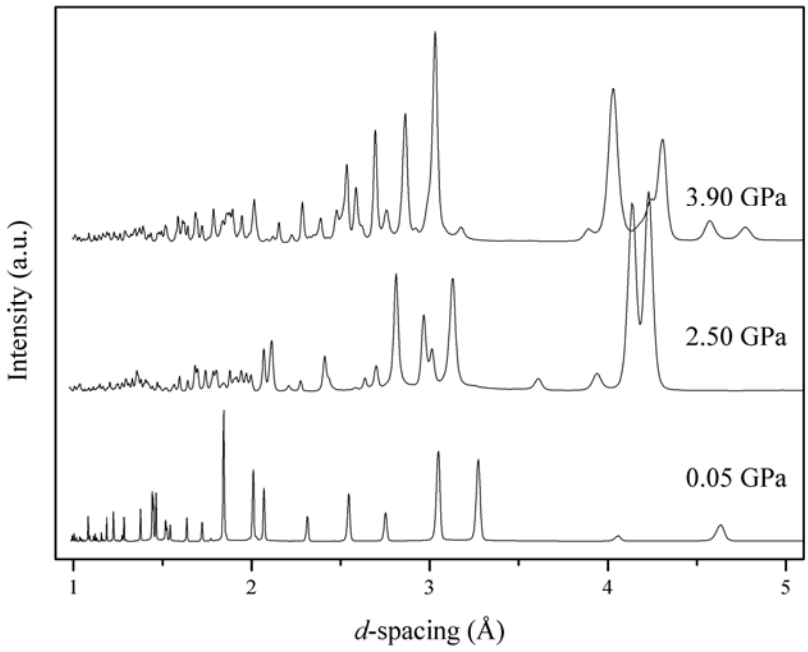

Figure 5.19 X-ray powder diffraction patterns collected for CsN_3-II (0.05 GPa), CsN_3-III (2.50 GPa) and CsN_3-IV (3.90 GPa) collected at the Extreme Conditions Beamline (I15), Diamond Light Source.

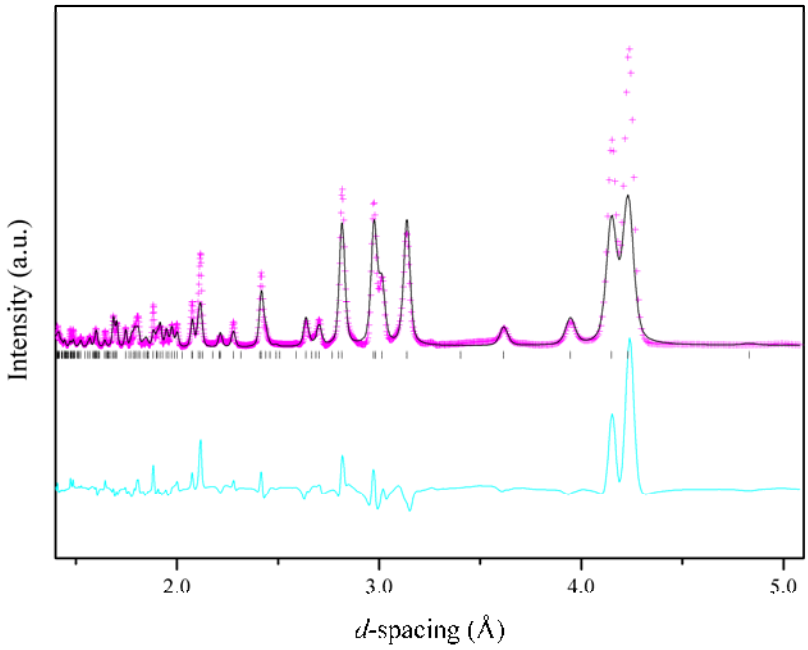

Figure 5.20 Refinement of the X-ray powder diffraction pattern collected for CsN_3 at 2.1 GPa using the CsN_3-III structural model (black tick marks). The observed intensities (I_{obs}) are represented as pink crosses and the calculated pattern (I_{calc}) is shown as a black line. The difference curve ($I_{obs} - I_{calc}$) is shown in cyan – this highlights numerous intensity mismatches in this pattern, particularly at d = 2.11, 2.42, 2.97 and 4.22 Å.

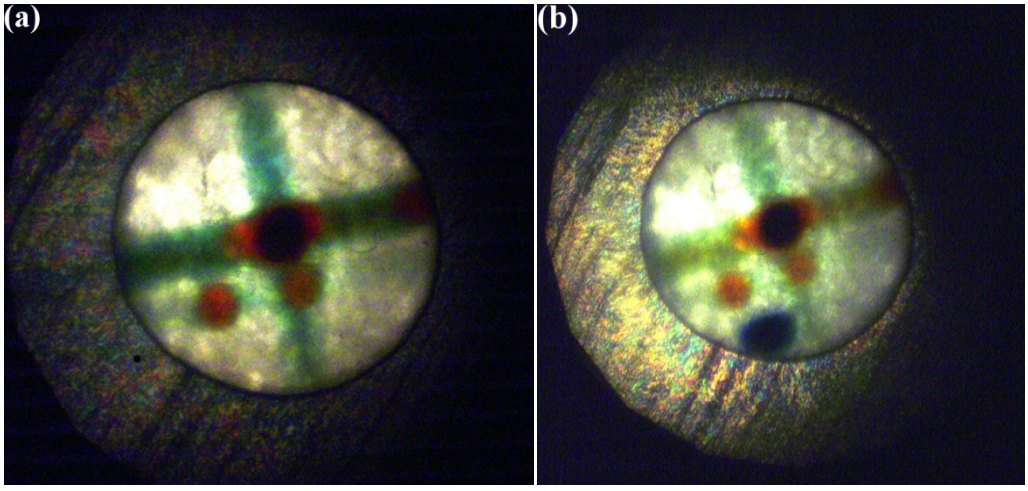

Figure 5.21 Optical microscope images of the radiation damage of CsN_3 at constant pressure (a) before and (b) after 90 second exposure. The green lines in each image are due to exposure of the sample to X-ray during alignment of the diamond-anvil cell; the red dots were produced during shorter data collections (10 s); the blue dot present in (b) is an effect of exposure of a fresh sample of CsN_3 to synchrotron radiation for 90 sec.

This dramatic evidence of sample deterioration in the synchrotron beam prompted the investigation of possible (crystalline) decomposition products which may be present in

sufficient quantities to contribute to the Bragg scattering. The majority of the intensity mismatches are coincident with diffraction peaks arising from caesium metal ($Im\bar{3}m$) although the relative intensities of these peaks do not correspond with the calculated pattern based on the cubic structure of Cs(s). This is perhaps not surprising as one would expect the small quantities of metal deposited in this way to be under extreme strain and to exhibit preferred orientation. Furthermore the deposition of caesium metal also implies the formation of a (or various) polynitrogen species, which may be expected to have an effect on the relative intensities of the diffraction peaks observed in this experiment. It would therefore be beneficial to repeat these studies and characterise the products of photolysis by a number of methods, particularly vibrational spectroscopy. Once identified and characterised at pressure, the recoverability of these products to ambient conditions should then become a priority in order to explore this avenue as a route to synthesising novel, 'greener' energetic materials.

Unfortunately the uncertainty over the effect of irradiation on CsN_3 has meant that it has not been possible to structurally characterise the second high-pressure polymorph, for which X-ray powder diffraction patterns were also collected. It would therefore also be worthwhile repeating this study using short exposure times in order to obtain high-resolution X-ray powder diffraction data on CsN_3-IV and CsN_3–V, while minimising sample decomposition.

Summary: CsN_3

The compression of caesium azide has been studied to a maximum pressure of 6.0 GPa by a combination of X-ray and neutron powder diffraction: evidence of three high-pressure polymorphs is presented. The structure of the first high-pressure form (CsN_3-III) has been determined by a combination of X-ray and neutron powder diffraction. In addition, evidence of two further high-pressure polymorphs is presented and current efforts are being directed at the structural characterisation of these forms. An unexpected result of the X-ray powder diffraction study was the observation of photolysis at pressure, resulting in Cs metal and, possibly, polynitrogen species. These studies should therefore be supplemented by a more rigorous study in order to asses the sample composition critically and to investigate the possibility of the recovery of the product materials to ambient pressure.

5.5.3 TlN_3

High-Pressure Neutron Diffraction Study

The initial aim of the structural investigation of thallium azide was to obtain high quality diffraction data on the high-pressure polymorph, TlN_3-III. A multiplot of the neutron powder

diffraction patterns collected during this experiment is shown in Figure 5.22. Since the phase transition from the tetragonal form II to the high-pressure form was reported to be *ca* 0.7 GPa, the initial increases in sample pressure were small (0.05 – 0.1 GPa increments). In this way it was possible to carry out Rietveld refinements on the powder diffraction patterns collected for TlN_3-II in this lower pressure regime (unit cell parameters may be found in Table 5.5). A 2nd order Birch-Murnaghan EoS has been fitted to the smooth compression of unit cell volume with V_0 (refined) 283.0(9) $Å^3$, B_0 = 21(3) GPa and B'(fixed) = 4. Unfortunately the relatively narrow stability range of TlN_3-II meant that any scatter in the data was magnified and thus it was not possible to determine a higher-order EoS and the e.s.d calculated for the bulk modulus is larger than desired. Despite this, the value of B_0 is consistent with other metal azides and the calculated V_0 compares favourably with the volume at ambient conditions (282.6(1) $Å^3$) determined experimentally by X-ray powder diffraction.

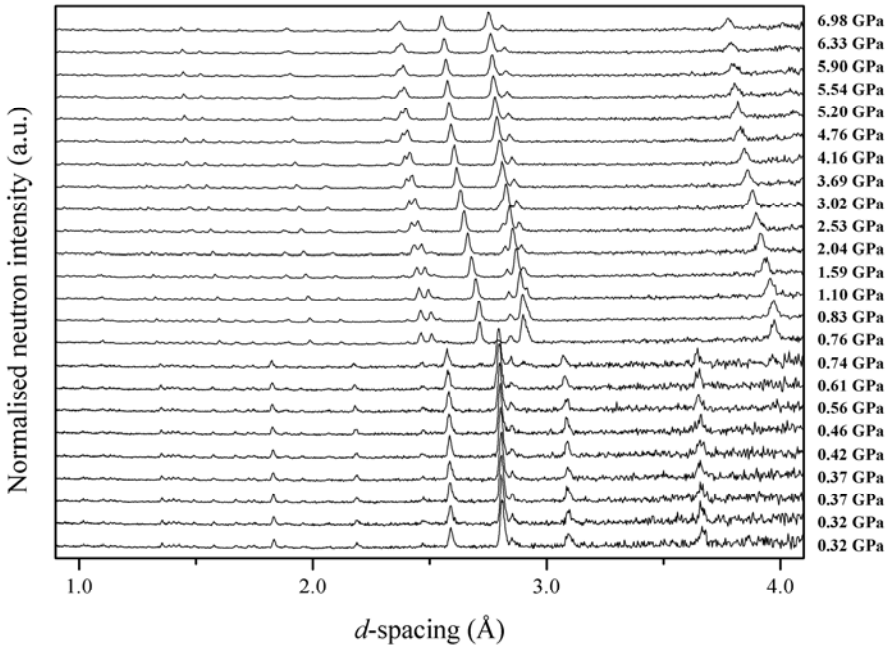

Figure 5.22 Multiplot of neutron powder diffraction patterns collected during the compression of TlN_3. The patterns collected below 0.76 GPa display a lower signal-to-noise ratio, since shorter collection times were utilised in these cases (*ca* 1 hr compared to 4 hrs for the later patterns).

Comparison of the structure determined at 0.74 GPa with that obtained from the initial pattern (0.32 GPa) shows that the compression of the unit cell is not accompanied by any rotation of the N_3^- anions and is surprisingly isotropic. Plots of the relative compression of

the unit cell axes (Figure 5.23) show that the compression within the layers of N_3^- and Cs^+ (*ab*-plane) is comparable to compression normal to the layer (*c*-axis).

P (GPa)	*a*, *b* (Å)	*c* (Å)	*V* (Å^3)	wR_p
0.32	6.1775(5)	7.3155(6)	279.17(4)	0.121
0.32	6.1762(6)	7.3141(8)	279.00(5)	0.151
0.37	6.1742(5)	7.3062(7)	278.52(4)	0.205
0.37	6.1707(5)	7.3022(7)	278.05(4)	0.125
0.42	6.1661(5)	7.3005(7)	277.57(4)	0.133
0.46	6.1604(5)	7.2957(7)	276.87(4)	0.124
0.56	6.1571(5)	7.2889(7)	276.33(4)	0.116
0.61	6.1472(6)	7.2847(8)	275.27(5)	0.146
0.74	6.1398(7)	7.2793(9)	274.41(5)	0.168

Table 5.5 Unit cell parameters determined during the compression of TlN_3-II, to a maximum pressure of 0.74 GPa.

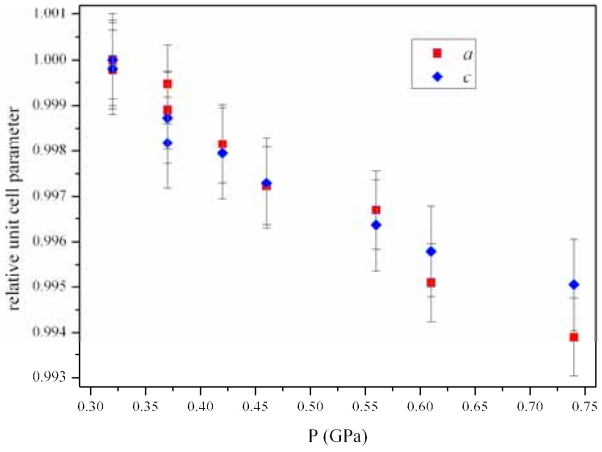

Figure 5.23 Relative compression of the unit cell axes in TlN_3-II to a maximum pressure of 0.74 GPa.

Another advantage of increasing the sample pressure in very small increments is the accurate determination of the II/III transition pressure (to within 0.2 GPa). The diffraction pattern collected at 0.76 GPa shows striking differences when compared to the pattern collected at 0.74 GPa; this is clear evidence of a phase transition. The quality of the diffraction pattern (after 2.5 hours) meant that it was possible to obtain an orthorhombic unit cell (*Immm*) for this high-pressure form. It was possible to carry out full-profile Rietveld refinement on this pattern and all subsequent patterns collected during the compression to a maximum pressure

of 6.98 GPa. It should be noted that the axes have been chosen to facilitate comparison with the ambient pressure tetragonal form.

Comparison of the structure of TlN_3-III determined at 0.76 GPa with the tetragonal structure immediately preceding the phase transition highlights the dramatic rearrangement that the azide anions undergo over this transition. As is illustrated in Figure 5.24, the phase transition involves an out-of-plane rotation of half of the azides (type I) to lie parallel to the orthorhombic *c*-axis, while the other azides (type II) are re-oriented parallel to the *a*-axis. As a result there are two independent azide units, an observation which is reflected in the splitting of vibrational modes noted by previous investigators.[57] These independent azides are arranged perpendicular to one another in chains that run parallel to the *c*-axis: the negative terminal N-atom of one is aligned with the positive central N-atom of its nearest neighbour, at a distance of 3.03 Å.

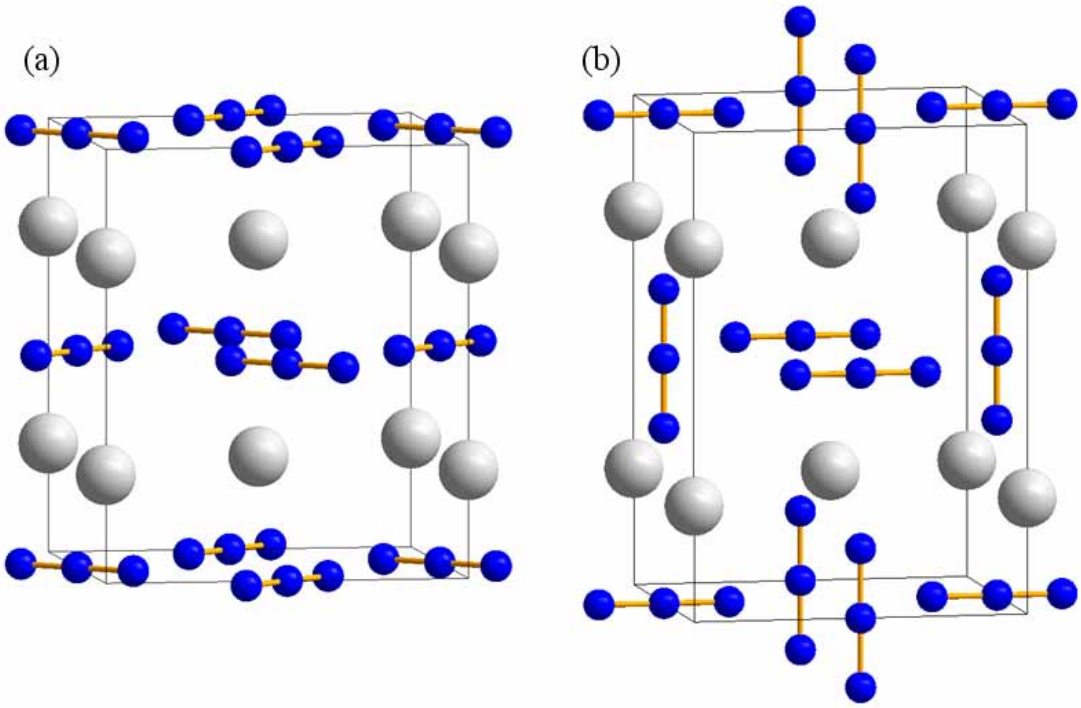

Figure 5.24 Comparison of the structures of (a) TlN_3-II and (b) TlN_3 –III clearly demonstrating the out-of-plane rotation of half of the azide anions over the high-pressure phase transition.

This arrangement of the azides results in each adopting a different co-ordination environment. In Type I each terminus lies in close proximity to four Tl cations (2.90 and 3.02 Å) in the layers immediately above and below the azide. Looking down the length of the N_3^- unit, these cations lie directly above one another resulting in a cuboidal configuration (see Figure 5.25 (a)). In contrast, Type II are co-planar with their four nearest Tl cations,

giving rise to the bifurcated N…Tl interactions shown in Figure 5.25(b). The co-ordination environment of the thallium cations can be thought of as a greatly distorted octahedron involving the termini of four Type I azides (2.90 and 3.02 Å) and two of Type II (2.88 Å). This is illustrated in Figure 5.26(a). Furthermore, it should be noted that the cations do not order themselves in perfectly linear chains; when viewed down the *b*-axis the alternating arrangement of Type I and Type II results in a wave-like distribution of Tl^+ cations (Figure 5.26(b)), which becomes more pronounced throughout compression (from 3.8° at 0.76 GPa to 6.3° at 6.98 GPa).

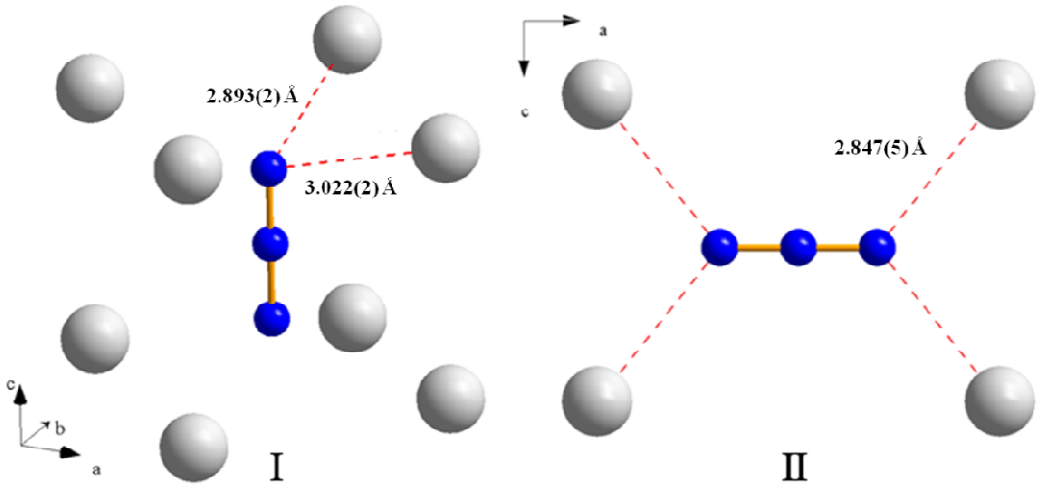

Figure 5.25 Co-ordination environments of the independent azides in TlN_3 (Type I and Type II) at 0.76 GPa.

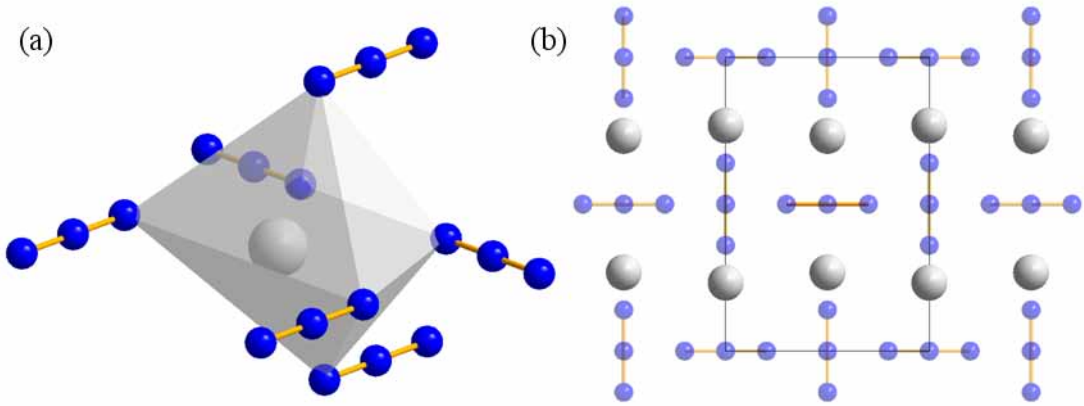

Figure 5.26 Co-ordination environment of the Tl cations in TlN_3 (a) the distorted O_h round one cation, and (b) the wave-like distribution of cations in unit cell viewed down the *a*-axis.

The unit cell parameters over the course of the experiment (from 0.32 to 6.98 GPa) have been tabulated in Table 5.6 and plotted in Figure 5.27. This shows that the lengthening of the tetragonal axis is outweighed by the shortening of the *a*- and *b*-axes, resulting in a 2.7%

reduction in unit cell volume over the phase transition. This sizeable contraction and the considerable degree of re-organisation within the structure explain the reconstructive nature of this phase transition noted during single-crystal studies.[18]

P (GPa)	a (Å)	b (Å)	c (Å)	V (Å^3)	wR_p
0.76	5.8274(6)	5.4141(3)	8.4670(7)	267.14(3)	0.057
0.83	5.8261(4)	5.4097(3)	8.4589(5)	266.61(3)	0.034
1.10	5.8145(5)	5.3840(3)	8.4224(7)	263.66(4)	0.050
1.59	5.7943(5)	5.3472(3)	8.3703(6)	259.34(3)	0.044
2.04	5.7743(5)	5.3137(3)	8.3227(7)	255.37(3)	0.045
2.53	5.7549(4)	5.2817(3)	8.2777(6)	251.61(3)	0.048
3.02	5.7353(4)	5.2520(3)	8.2354(6)	248.07(3)	0.047
3.69	5.7120(4)	5.2207(3)	8.1901(6)	244.23(3)	0.044
4.16	5.6933(4)	5.1981(3)	8.1595(6)	241.47(3)	0.049
4.76	5.6742(5)	5.1712(3)	8.1217(7)	238.31(3)	0.050
5.20	5.6607(5)	5.1548(3)	8.0995(7)	236.34(3)	0.054
5.54	5.6492(5)	5.1400(4)	8.0789(8)	234.59(4)	0.061
5.90	5.6402(5)	5.1268(4)	8.0628(9)	233.15(4)	0.073
6.33	5.6266(6)	5.1123(4)	8.0428(9)	231.35(4)	0.061
6.98	5.6098(6)	5.0923(4)	8.0137(9)	228.93(4)	0.070

Table 5.6 Unit cell parameters obtained by Rietveld refinement of neutron powder diffraction patterns collected for TlN_3-III.

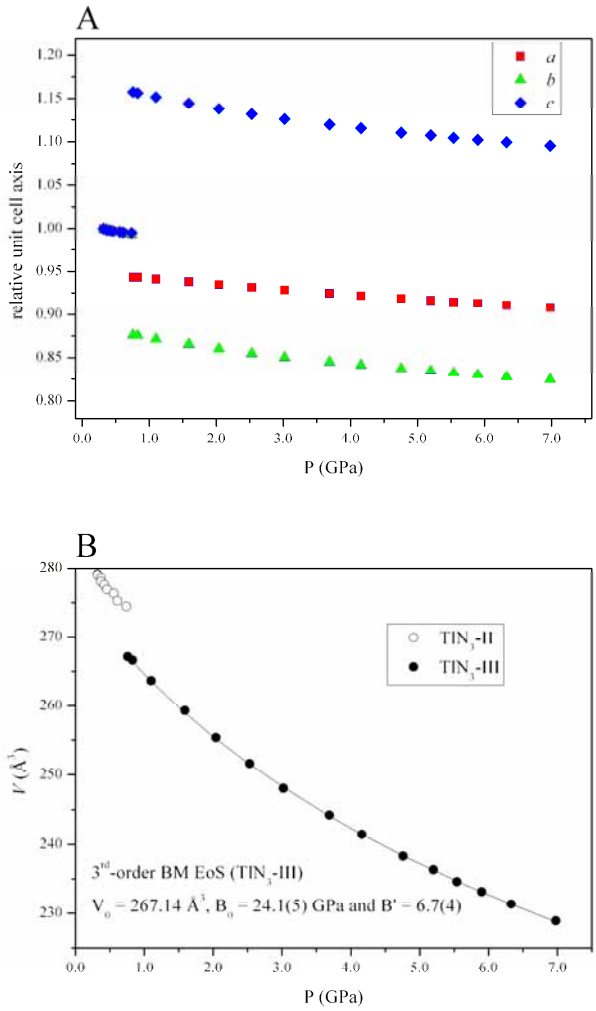

Figure 5.27 (a) relative compression of the unit cell axes of TlN_3 between 0.3 and 7.4 GPa, highlighting the lengthening of the tetragonal *c*-axis over the II/III transition; and, (b) the contraction of the unit cell volume over the same pressure regime, with clear evidence of the first-order transition.

The variation in the unit cell volume with pressure can be described by a 3rd-order Birch Murnaghan EoS with $V_0 = 267.14$ Å^3 (fixed), $B_0 = 24.1(5)$ GPa and B' = 6.7(4). It should be noted that for this high-pressure phase, the volume at the first pressure (0.76 GPa) where it was observed has been taken as V_0; all pressures were therefore normalised to this. The coefficients of the EoS have been verified by construction of an *Ff*-plot and are consistent with the compression characteristics observed for the other metal azides in this study. The larger value of the bulk modulus for this polymorph compared to TlN_3-II shows that this form is less compressible than the ambient pressure form, although it should be noted that the large error in the bulk modulus of TlN_3-II means that it is unadvisable to draw any further conclusions.

The relative shortening of the unit cell axes in TlN_3-III (shown in Figure 5.27) allows one to assess the compression mechanism critically. This figure clearly shows that the *a*-axis is most resistant to compression – while the shortening of the *a*-axis does result in shorter interactions between the cations and the azide termini within the same plane, this is accompanied by an increase in the angle formed between the Type II azide and its two thallium neighbours which would be expected to reduce the efficacy of any cohesive interactions (see Figure 5.28a). Contraction of the *c*-axis results in a significant shortening of the interaction between the termini of Type I azides and the central atom of Type II (~7% over the pressure range studied). Interestingly the parallel interactions between neighbouring cations are compressed by either ~2% or ~ 10% over the same pressure range (Figure 5.28b), resulting in the observed wave-like distribution becoming more pronounced at higher pressures. This differential contraction would therefore suggest that, at some finite pressure, TlN_3-III would undergo a symmetry-breaking phase transition. The direction aligned with the interplanar separation (*b*-axis) is, as expected, the most compressible axis.

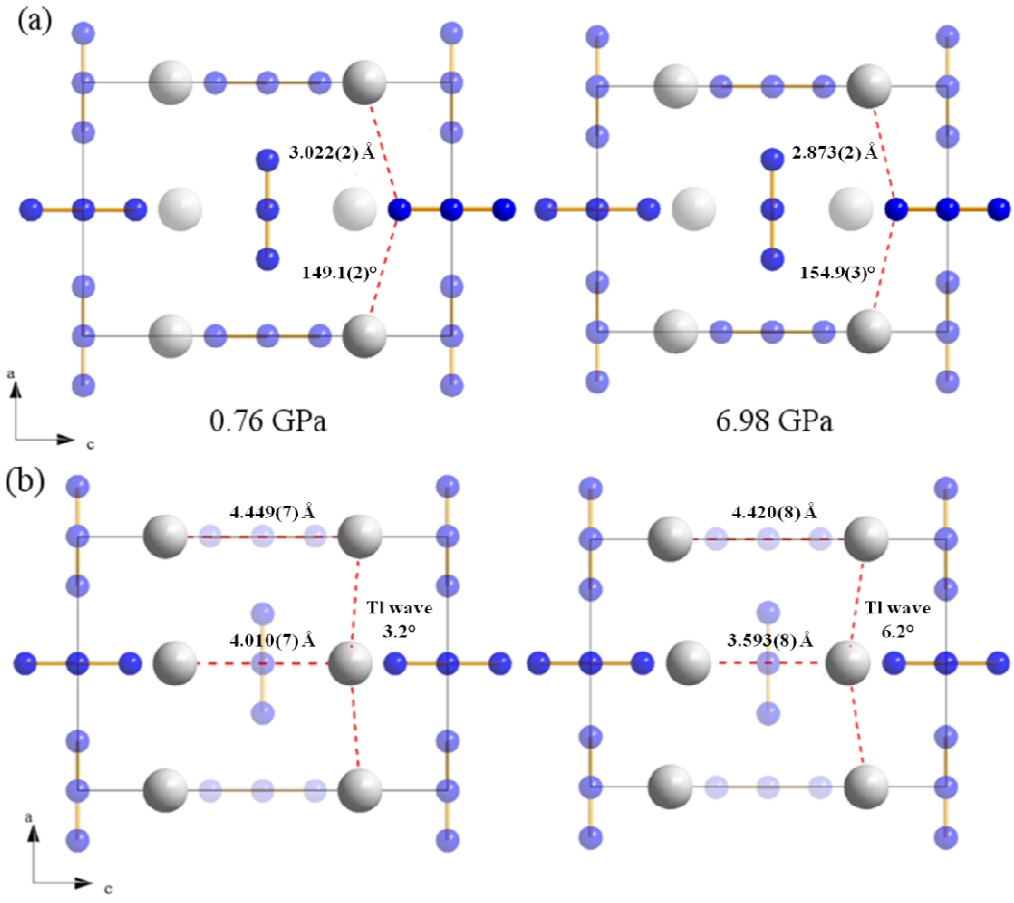

Figure 5.28 (a) Compression along the *a*-axis, highlighting the increased angle between Tl-N-Tl, (b) compression along the *c*-axis, which has been shown to result in the differential contraction of Tl…Tl and N…N interactions.

Finally it should be noted that a weak reflection (2.32 Å) is observed in the patterns collected above 3.69 GPa which could not be accurately described by the current structural model. This peak persists during compression, but the only other significant change in the diffraction pattern is a slight reduction in intensity of the peak at 2.60 Å; no other extra peaks are observed (Figure 5.29). For this reason it has not been possible to determine whether this is indicative of a new phase, perhaps as a result of a monoclinic distortion of the orthorhombic form III, or in fact is evidence of a decomposition product. Unfortunately mechanical failure of the gasket during decompression resulted in complete evacuation of the sample chamber. This meant that it was impossible to collect a neutron powder diffraction pattern at atmospheric pressure to examine the reversibility of the II/III phase transition and no material could be recovered for subsequent analysis to assess sample purity. It would therefore be worthwhile to investigate the high-pressure polymorphism of TlN_3 using high resolution X-ray diffraction, primarily to determine if a phase transition does occur above 3.69 GPa, but also to characterise the decompression behaviour fully.

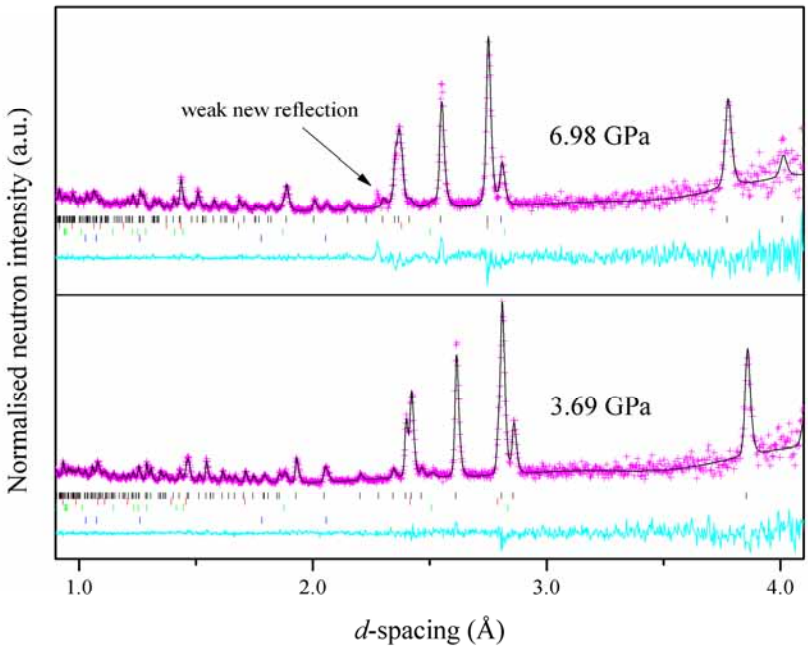

Figure 5.29 Rietveld refinement of the patterns collected at 6.98 GPa and 3.69 GPa to show the emergence of the weak peak *ca* 2.3 Å in the higher pressure pattern. In both cases the experimental data (I_{obs}) are represented as pink crosses, the calculated pattern (I_{calc}) is superimposed as a black line and the difference between these ($I_{obs} - I_{calc}$) is shown in cyan. Tick marks for each phase are also shown for clarity: TlN_3 (black), Pb (red), WC (green) and Ni (blue).

In addition to examining the high-pressure behaviour of thallium azide at ambient temperature, the low temperature phase (TlN_3-IV) was investigated at ambient pressure by X-ray powder diffraction. Due to concerns previously raised [55] over the effect of sample aging upon the phase behaviour of TlN_3, high-quality X-ray powder diffraction data were collected (2θ range of 2 – 140°) for a freshly-prepared sample at room temperature to confirm sample purity. The quality of the diffraction data (and the Rietveld refinement of this pattern using the tetragonal TlN_3-II structure) is highlighted in Figure 5.30, which clearly shows that no contamination from a decomposition product or other impurity occurred. The sample was subsequently cooled to 100 K, at which point diffraction data were collected over a period of 8 hours to ensure effective powder-averaging throughout the whole 2θ range and therefore to facilitate structure solution. X-ray powder patterns were then collected at 20 K intervals between 80 and 280 K (1 hr exposure), although smaller temperature increments were employed in the range of 230 – 245 K in order to determine accurately the TlN_3-II → IV transition temperature. A multiplot of the X-ray powder diffraction patterns collected during this experiment is shown in Figure 5.31.

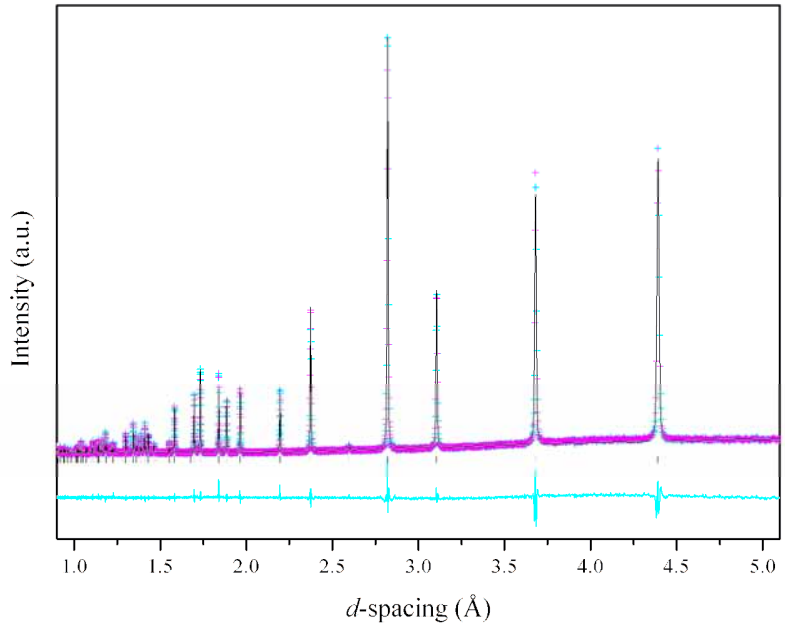

Figure 5.30 Rietveld refinement of the X-ray powder diffraction pattern collected for TlN_3-II (black tick marks) at room temperature, highlighting the quality of the data and the sample. The experimental data (I_{obs}) are shown as pink crosses, the calculated pattern (I_{calc}) as a black line and the difference curve ($I_{obs} - I_{calc}$) in cyan.

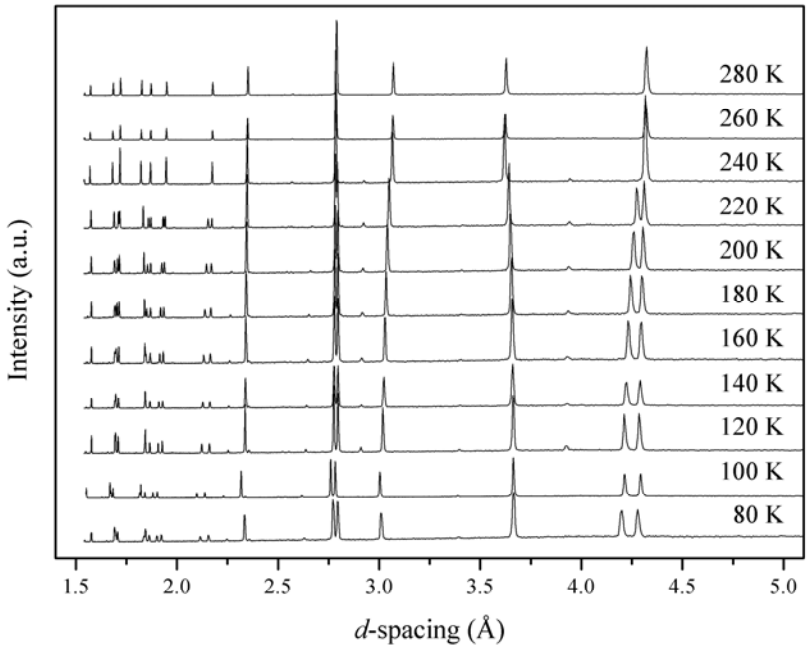

Figure 5.31 Mulitplot of the X-ray powder diffraction patterns collected during the variable temperature study of TlN_3 (intensities scaled for clarity). The TlN_3-II → IV transition between 240 and 220 K is evident in the splitting of peaks *ca* 2.15, 2.75 and 4.40 Å.

Close inspection of the diffraction patterns collected at 235 and 240 K, particularly in the region $d < 2.2$ Å, shows splitting of the diffraction peaks, characteristic of a phase transition between these temperatures, see Figure 5.32. This transition temperature is in accordance with that observed by Iqbal and Christoe during the spectroscopic measurements [55], but is significantly lower than the transition temperature (248 ± 5 K) reported by Mauer *et al.* in their X-ray powder diffraction study. It should be noted, however, that Mauer *et al*. based their determination of the transition temperature on a discontinuity in the slope of a plot of the unit cell parameters *versus* temperature and remarked that 'the change in the X-ray pattern is subtle, and it is difficult to establish the transition temperature accurately'.[54] The quality of the data reported herein, however, has allowed the accurate determination of the transition temperature to be between 235 and 240 K – the pattern collected at 240 K exhibits no peak broadening and the characteristic peaks are suitably modelled by singlets. A more detailed study in this temperature range using high-resolution powder diffraction is currently underway in order to determine the transition temperature more precisely.

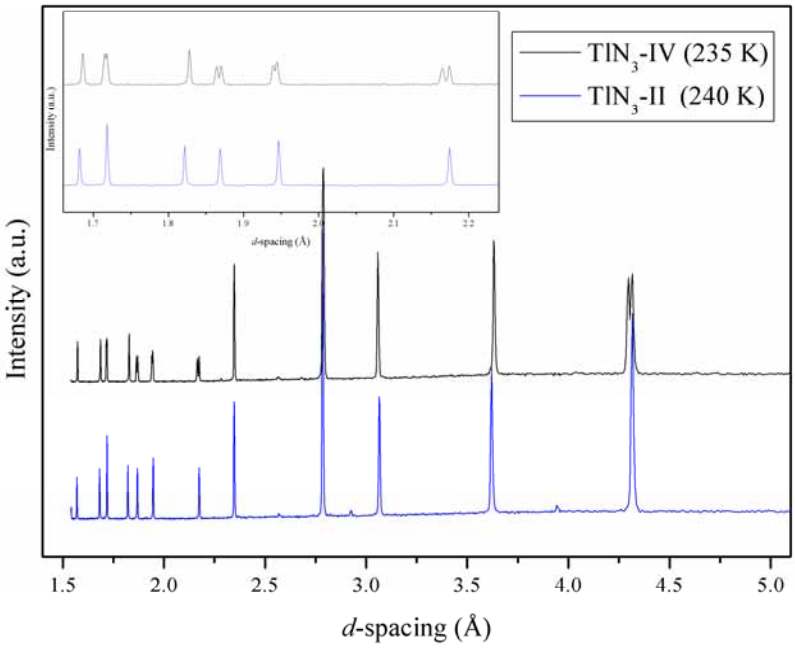

Figure 5.32 Comparison of the diffraction patterns collected for TlN_3 at 240 and 235 K. The tetragonal → orthorhombic transition is indicated by the splitting of numerous peaks, particularly those highlighted in the inset.

The splitting observed in the characteristic peaks (such as (004) and (400) at d ~ 2.2 Å) is indicative of a phase transition from the tetragonal structure of TlN_3-II to an orthorhombic structure, in accordance with conclusions drawn from previous diffraction studies.[54] In the present study, however, the quality of the 100 K data allowed space group determination (*Cmcm*) and subsequent structure solution. The structure of TlN_3-IV was solved by Dr S. Margadonna (School of Chemistry, University of Edinburgh), using the simulated annealing program Powder Solve within Materials Studio.[83] The positions of the heavy atoms were determined initially (using $P\bar{1}$ symmetry) before global optimisation, throughout which the azide anions were treated as rigid bodies. It was then possible to carry out full-profile Rietveld refinement of all diffraction patterns collected for this form, the quality of which is typified by that shown in Figure 5.33 for the pattern collected at 100 K. Throughout refinement the angles N1-N2-N1 and N3-N4-N3 were restrained to be 180(2)° by the insertion of a 'dummy' atom at positions equivalent to N1' and N3' (with zero occupancy) and defining each restraint in terms of N1-N2-N1' and N3-N4-N3'.[84]

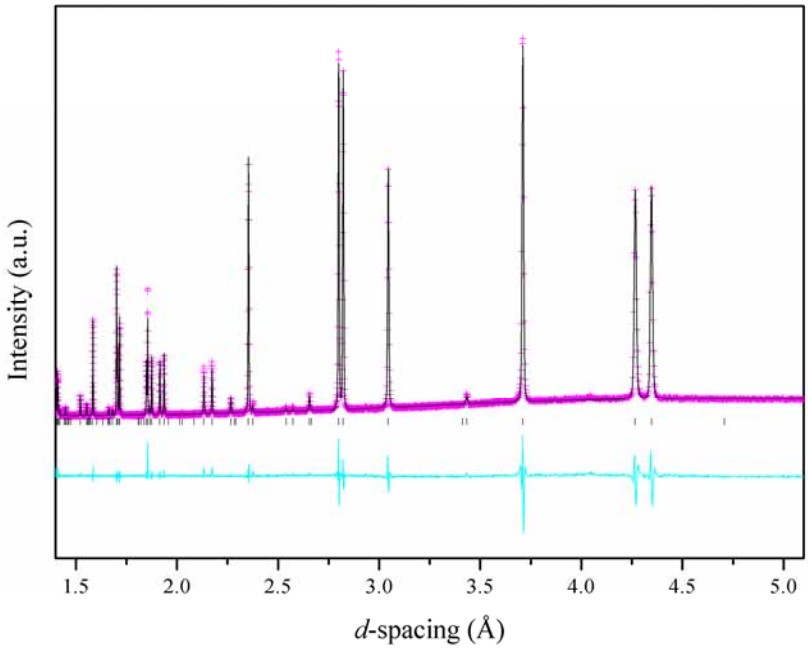

Figure 5.33 Rietveld refinement of the diffraction pattern collected at 100 K using the TlN3-IV structural model (black tick marks). The experimental data (I_{obs}) are shown as pink crosses, the calculated pattern (I_{calc}) as a black line and the difference between these models ($I_{obs} - I_{calc}$) is shown in cyan.

A summary of the unit cell parameters determined throughout this experiment can be found in Table 5.7 and in Figure 5.34(a), which clearly shows the phase transition between the tetragonal form II and the orthorhombic form IV. In order to provide a direct comparison between the different forms, also presented in Figure 5.34(a) are values calculated for $a_{ortho}/\sqrt{2}$ and $c_{ortho}/\sqrt{2}$, since the *a*- and *c*-axes in the orthorhombic cell correspond to the face diagonals of the original tetragonal cell. Furthermore, as the transition involves a doubling of the unit cell, it has been necessary to scale the volume of TlN_3-IV by 0.5 to facilitate comparison of the thermal expansion of each form, presented graphically in Figure 5.34(b). The volumetric thermal expansion of TlN_3-IV has been determined for the temperature range 80 – 235 K: α_v = [6.0(3) + 0.0519(20) T] x 10^{-5} K^{-1}; in comparison, α_v = [-0.9(5) + 0.0039(18) T] x 10^{-3} K^{-1} for TlN_3-II in the range 240 – 293 K.